

REACTIVE VARIABLE CHARGE POTENTIAL DEVELOPMENT AND ATOMISTIC
SIMULATIONS OF SURFACE AND HETEROGENEOUS INTERFACIAL
INTERACTIONS

By

YU-TING CHENG

A DISSERTATION PRESENTED TO THE GRADUATE SCHOOL
OF THE UNIVERSITY OF FLORIDA IN PARTIAL FULFILLMENT
OF THE REQUIREMENTS FOR THE DEGREE OF
DOCTOR OF PHILOSOPHY

UNIVERSITY OF FLORIDA

2013

© 2013 Yu-Ting Cheng

To my family with love

ACKNOWLEDGMENTS

First, I would like to show my gratitude to my advisor Prof. Susan B. Sinnott for her kind instruction and all efforts to guide me during my Ph.D. study. Her continuous supports, suggestions and helpful discussions have helped me pass through all difficulties during my research experiences. I would also like to thank Prof. Simon R. Phillpot for his invaluable advices on the studies in this dissertation and to extend my sincere appreciation to my committee members Prof. Paul H. Holloway, Prof. Scott S. Perry and Prof. Sergey Vasenkov for their supports and comments.

Great thanks to all former and present members in the Computational Materials Science Focus Group for their friendship and continuous supports. I also want to specially thank Drs. Tao Liang, Tzu-Ray Shan and Bryce Devine for their mentor and help on my researches, Te-Yu Kao, Ya-Chiao Chang, Pang-Wei Liu, Hsiu-Wen Tsai, Aiden Liu, Mong-Jen Chen, Hsin-Yin Tsai, Yi-Chung Wang, Ya-Wen Yeh, Chung-Hsin Fan, Chao-Hsuan Shen, Kun-Ta Tsai, Tsu-Wu Chiang, and Tzung-Han Lai for their constant support and encourage inside and outside the school.

Most importantly, my beloved family gives me unconditional love, patience and support. Without them, none of this would have been possible. Finally, I want to express my gratitude to my lovely wife, Chih-Yun (Angela) Huang, for her never-ending support. The dissertation is dedicated to her.

TABLE OF CONTENTS

	<u>page</u>
ACKNOWLEDGMENTS.....	4
LIST OF TABLES.....	8
LIST OF FIGURES.....	10
ABSTRACT	12
CHAPTER	
1 INTRODUCTION	14
1.1 General Introduction	14
1.2 Integration of Computational and Experimental Methods	15
1.3 Outline	18
2 COMPUTATIONAL METHODS	25
2.1 Computational Methods	25
2.2 Density Functional Theory	25
2.3 Classical Empirical Methods	27
2.3.1 Interatomic Potentials	27
2.3.2 Molecular Dynamics (MD) Simulations	28
2.3.3 Ensembles.....	29
2.3.4 Periodic Boundary Conditions and Cutoff Radius.....	30
2.4 Variable Charge Reactive Potentials: COMB Potentials	30
2.4.1 General Formalism of the Third-Generation COMB Potentials.....	30
2.4.2 Electrostatic Energies	31
2.4.3 Short-Range interactions.....	34
2.4.4 van der Waals Interactions	36
2.4.5 Correction Terms.....	37
2.4.6 Dynamic Charge Equilibration Method	37
2.5 Parameterization of COMB Potentials	39
2.5.1 Creating the Database.....	40
2.5.2 Parameterization of Pure Systems	41
2.5.3 Parameterization of Binary Systems.....	41
2.6 Transition State Search: Dimer Method	42
2.7 Summary	43
3 DEVELOPMENT OF COMB3 CU/ZNO POTENTIAL AND ITS APPLICATION ON CU CLUSTERS DEPOSITION ON ZNO SURFACE	50
3.1 Potential development and Properties of Cu/ZnO.....	52
3.1.1 Fitting Procedure	52
3.1.2 Predicted Properties of ZnO polymorphs.....	53

3.1.3	Predicted Properties of CuZn alloys	54
3.2	Interaction of Cu on ZnO(10 $\bar{1}0$)	54
3.2.1	Adsorption Energies of Cu Adatom on ZnO(10 $\bar{1}0$)	54
3.2.2	Migration barriers of Cu Adatom on ZnO(10 $\bar{1}0$)	55
3.3	Cu Clusters Deposition on ZnO(10 $\bar{1}0$)	56
3.3.1	Details of the MD Simulation of Cluster Deposition and Relaxation	56
3.3.2	Surface Morphology and Growth Mode	57
3.3.3	Effect of Incident Energy	59
3.3.4	Effect of Surface Temperature	60
3.4	Comparison of the Growth of Cu on Cu(111) and ZnO(10 $\bar{1}0$)	61
3.5	Summary	62
4	DEVELOPMENT OF COMB3 TI/TIO ₂ POTENTIAL AND ITS APPLICATONS ON CU CLUSTERS ON TIO ₂ (110) SURFACES	76
4.1	Potential Development and Properties of Ti and TiO ₂	77
4.1.1	Fitting Procedure	77
4.1.2	Predicted Ti Properties	78
4.1.3	Properties of Rutile TiO ₂ and Phase Stability	80
4.1.4	TiO ₂ Low Miller Index Surfaces	81
4.2	Heterogeneous Interfacial System: Cu _n /TiO ₂ (110).....	83
4.2.1	Cu Clusters on Stoichiometric TiO ₂ (110).....	83
4.2.2	Cu ₁₄₇ Clusters on Non-Stoichiometric TiO ₂ (110)	84
4.3	Summary	85
5	DEVELOPMENT OF COMB3 TI/TIN POTENTIAL AND ITS APPLICATONS ON TI/TIN INTERAFACES AND THE DEPOSTION OF ATOMIC OXYGEN ON TIN(001) SURFACE.....	95
5.1	Potential development and Properties of Ti, N ₂ , and TiN.....	96
5.1.1	Fitting Procedure	96
5.1.2	Fitted Properties of Ti metal and N ₂ molecule	97
5.1.3	Fitted and Predicted TiN Phase Stability and Properties	98
5.1.4	Predicted Defect Formation Energies and Surface Energies of rocksalt TiN	99
5.2	Predicted Dynamical Results	101
5.3	Applications of COMB3 TiN Potential	102
5.3.1	Adhesion of fcc-Ti/TiN(001) Interfaces	102
5.3.2	Atomic Oxygen deposition on TiN(001) surface	104
5.4	Summary	105
6	FIRST-PRINCIPLES STUDY OF EARLY STAGE OXIDATION OF FACETED AIN SURFACES	113
6.1	Computational Details.....	113
6.2	Adsorption of Atomic and Molecular Oxygen on the AIN surface.....	115

6.3 Summary	116
7 CONCLUSIONS	120
APPENDIX: POTENTIAL PARAMETERS FOR COMB POTENTIALS DEVELOPED IN THIS WORK.....	123
REFERENCE LIST.....	128
BIOGRAPHICAL SKETCH.....	141

LIST OF TABLES

<u>Table</u>	<u>page</u>
1-1 Characteristics of physical adsorption and chemisorption.	20
2-1 The common used interatomic potentials	45
2-2 List of fitting parameters for the pure systems.	46
2-3 List of fitting parameters for the charge-dependent energy terms.	46
2-4 List of fitting parameters for the binary systems.	46
3-1 Comparison of the properties of ZnO wurtzite phase predicted by the COMB2 and COMB3 potentials with values obtained from experiments and DFT calculations.	64
3-2 Properties of Cu-Zn alloys predicted by COMB3 compared to those from experiments and DFT calculations	64
3-3 The adsorption energy (eV) of a single Cu adatom at the three different adsorption sites on the ZnO(10 $\bar{1}$ 0) surface as predicted by COMB3 and DFT calculations.	65
3-4 Predicted migration barriers of a Cu adatom on the ZnO(10 $\bar{1}$ 0) surface found using the dimer method with COMB3 and compared with DFT results	65
4-1 Properties of Ti reproduced or predicted by the COMB3 potential developed in this work, and compared to experimental results, DFT calculations and the MEAM potential.	87
4-2 Properties of the rutile, anatase, and brookite phases calculated by the COMB potential. The properties are compared to experiments, DFT calculations and three other empirical potentials.	88
4-3 Cohesive energies of rutile titania and that relative to rutile titania for other polymorphs calculated from COMB potential in comparison with DFT calculations and other empirical potentials.	89
4-4 Low index surface energies of rutile TiO ₂ from the <i>ab initio</i> approaches and empirical potentials.	90
4-5 Charge variation (Q-Q _{bulk}) of surface atoms of TiO ₂ surfaces.	91
5-1 COMB predictions compared to published experimental results, DFT calculations, and MEAM potentials for the lattice constants a ₀ and c ₀ ,	

	enthalpy of formation, cohesive energy, bulk modulus, shear modulus and elastic constants of the rocksalt TiN and rutile Ti ₂ N.....	107
5-2	Comparison of formation energies of point defects in NaCl typed TiN crystal calculated from first-principles calculations and COMB potentials.....	108
5-3	Relaxed surface energy of TiN (100), (110) and (111) surface predicted by COMB potentials, in comparison with the predictions from published first-principles calculation and MEAM potentials.	108
6-1	Comparison of the computed bulk properties to the experimental data.....	117
6-2	Predicted adsorption energies (E_{ads}) of atomic oxygen on the flat and stepped AlN(10 $\bar{1}$ 0) surfaces.....	117
A-1	Atomic and electrostatic parameters of pure elements (O, Cu, N, Ti, and Zn) for COMB3 potentials.	124
A-2	Bond-typed parameters of pure element (O, Cu, N, Ti, and Zn) for COMB3 potentials.	125
A-3	Bond-typed parameters of Cu/ZnO system for COMB potential developed in this work.	126
A-4	Bond-typed parameters of TiN and TiO ₂ systems for COMB3 potentials developed in this work.	127

LIST OF FIGURES

<u>Figure</u>	<u>page</u>
1-1 Initial oxidation processes of bare metal surfaces.	21
1-2 Surface processes of metal thin films or clusters growth on metal oxide substrate.....	22
1-3 Hierarchy of multiscale modeling.....	23
1-4 Snapshot of a molecular dynamics simulations of water, carbon monoxide, and carbon dioxide molecules interacting with a copper catalyst supported by a zinc oxide substrate.....	24
2-1 Lennard-Jones (LJ) potential.....	47
2-2 Schematic representation of periodic boundary conditions in MD simulations ...	48
2-3 The two migration mechanisms of single Cu atom on Cu(100).	49
3-1 Top view of three different adsorption sites of Cu atoms on the ZnO(10 $\bar{1}$ 0) surface.....	66
3-2 The binding energy (eV) of Cu _n (n = 2 to 5) clusters on ZnO(10 $\bar{1}$ 0) predicted by DFT calculations and COMB potential.....	66
3-3 Relaxed structure of Cu ₅ clusters supported by the ZnO(10 $\bar{1}$ 0) surface.	67
3-4 Simulation model for deposition of Cu clusters on the ZnO(10 $\bar{1}$ 0) surface.....	68
3-5 MD simulation of the morphology of Cu clusters following the deposition of 1ML of Cu atoms.	69
3-6 Snapshots of just the Cu atoms at the indicated coverage (0.2–1ML) following deposition on ZnO(10 $\bar{1}$ 0).....	69
3-7 The deposition processes of Cu clusters landing on ZnO surface.....	70
3-8 Schematic of Ehrlich–Schwoebel barrier (ΔE_{ES}).....	70
3-9 Top-down snapshots from MD simulation of the surface morphology of 1ML of Cu deposited on ZnO(10 $\bar{1}$ 0) with different incident energies.....	71
3-10 Top-down snapshots from MD simulation of the morphology of 1ML Cu deposited on ZnO(10 $\bar{1}$ 0) maintained at the indicated temperatures.....	72

3-11	Snapshot from an MD simulation of the morphology of Cu clusters on ZnO (10 $\bar{1}0$) at the indicated coverage.....	73
3-12	Snapshot from an MD simulation of the morphology of Cu clusters on Cu(111) at the indicated coverage.....	74
3-13	Top-down snapshots from the MD simulations of 2ML Cu deposited on Cu(111) and ZnO(10 $\bar{1}0$)	75
4-1	Model of the rutile TiO ₂ surfaces.	92
4-2	Optimized geometries of Cu ₁₃ , Cu ₃₈ , Cu ₅₅ , and Cu ₁₄₇ clusters.	93
4-3	Charge distribution of relaxed Cu clusters on TiO ₂ (110)	93
4-4	Charge distribution of relaxed Cu ₅₅ clusters on the stoichiometric and defected TiO ₂ (110) surfaces.....	94
5-1	The unit cell of fitting structures for TiN and Ti ₂ N systems in this study	109
5-2	Schematic of layers sequence of the TiN(001), (110), (111) surfaces.....	109
5-3	The crystal structures of rocksalt TiN as a function of temperature	110
5-4	The interfacial structures of Ti(001)/TiN(001)	111
5-5	Snapshots of oxygen atoms deposited on the TiN(001) surface	112
5-6	Snapshots from the deposition of single oxygen molecule on the TiN(001) surface.....	112
6-1	Stable adsorption sites on the flat and stepped AlN(10 $\bar{1}0$) surfaces	118
6-2	The energy change of the adsorption and dissociation of O ₂ on the flat and stepped AlN(10 $\bar{1}0$) surface.....	119

Abstract of Dissertation Presented to the Graduate School
of the University of Florida in Partial Fulfillment of the
Requirements for the Degree of Doctor of Philosophy

REACTIVE VARIABLE CHARGE POTENTIAL DEVELOPMENT AND ATOMISTIC
SIMULATIONS OF SURFACE AND HETEROGENEOUS INTERFACIAL
INTERACTIONS

By

Yu-Ting Cheng

December 2013

Chair: Susan B. Sinnott
Major: Materials Science and Engineering

Advancements in computational resources have enabled the application of computational methods in a manner that complements experimental measurements and ultimately capture the process-structure-property relationships of material systems. Among various computational methodologies, the classical empirical methods (also known as interatomic potentials) has been developed and used in molecular dynamics (MD) simulations. Such simulations are able to model systems at atomic and nanometer scale and dynamical processes that include the effects of temperatures and pressure, which is beyond the reach of quantum-based approaches. Because the interatomic potential is the main gradient in MD simulations for calculating energies and forces, it is therefore important that the interatomic potential is accurate and transferable in order to correctly describe the chemical and physics properties of materials under a variety of conditions. In addition, to ensure the widest possible application, the interatomic potential should be capable of simulating systems with different types of chemical bonding present.

Recently, the charge-optimized many-body (COMB) potentials were developed to tackle this challenge and parameterized to include a wide range of elements and compounds, including heterogeneous systems. In this dissertation, the main objective is to apply and parameterize the third-generation COMB potential for several specific heterogeneous systems and use them to investigate the underlying physics of interfacial and surface phenomena that are critical for the success of many applications. Potentials were developed for metallic Zn and Ti, and for CuZn, CuTi, ZnO, TiO₂, and TiN. Through MD simulations, COMB potentials have been successfully applied to characterize the growth modes of Cu on Cu(111) and ZnO(10 $\bar{1}$ 0) and clearly elucidate the ways in which Cu growth transitions from layer-by-layer to three-dimensional as Cu coverage increases. For the Cu/TiO₂ system, an enhanced bonding between Cu clusters and the oxidized TiO₂(110) surface was predicted. The adsorption mechanism was predicted to be the formation of a metal-oxygen bond between Cu and O. In addition, the characterization of the adsorption of O and O₂ on the TiN(001) surface showed that the COMB potentials for Ti/TiN/TiO₂ and N/NO systems were well suited to the oxidation study.

As a result of the work carried out and described in this dissertation, COMB potentials can be considered to be potent tools from an engineering perspective to provide useful guidance for the interpretation of experimental data and from a fundamental science perspective to facilitate materials development.

CHAPTER 1 INTRODUCTION

1.1 General Introduction

Processes at surface are critical for the success of many applications.¹⁻⁵ For example, surface oxidation, in particular at high temperatures, is inevitable for many systems where the application takes place under ambient conditions. The process of surface oxidation may result in destructive outcomes such as the degradation of thermal barrier coatings^{6,7} or beneficial outcomes such as heterogeneous catalysts.^{8,9}

With recent advances in material characterization techniques, such as in-situ transmission electron microscopy (TEM), Auger electron spectroscopy (AES), and X-ray photoelectron spectroscopy (XPS), experimental methods are able to provide atomic resolution images of surfaces and accompanying information regarding the details of their structure, electronic structure, and composition. As a result, several mechanisms of the initial oxidation process on bare metal surfaces have been determined,¹⁰⁻¹² as shown in Figure 1-1.

In principle, when oxygen molecules impinge on material surfaces, two adsorption processes may take place depending on type of interaction that are prevalent.¹³ One is physisorption, where the interactions are dominated by van der Waals forces. Because of the weak interaction, the molecule has a high mobility on surfaces and this adsorption is reversible, which leads to high desorption rates. In contrast, chemisorption involves the transfer and sharing of electrons, which leads to chemical bond formation. Therefore, chemisorption results in stronger molecule-surface interactions than physisorption. In addition, chemisorption is sensitive to details of the surface structure and its symmetry. The detailed characteristics of physisorption and

chemisorption are listed in Table 1-1. Subsequently, the next process is metal-oxide formation, for which two possible mechanisms have been proposed. First, the dissociative oxygen atoms penetrate into the subsurface and form an oxide within the substrate. Second, the substrate surface atoms exchange with adsorbed oxygen atoms and form an oxide film at the surface.

Many of the above-described processes at surface are also important in heterogeneous catalysis using metal/metal oxide systems. Reactions where such catalysts are important include the synthesis of methanol via hydrogenation of CO and CO₂,¹⁴ water-gas shift reaction for removal of CO,^{15, 16} and the production of hydrogen by steam reforming of methanol.¹⁷ Despite the technological importance of these reactions, in many instances the nature of the active sites and their relative stability is still not well established. Factors such as surface geometry, the interface between the metal and oxide, and the size and distribution of metal clusters strongly control the reactivity of the catalyst and the selectivity of products. Because these factors are closely associated with the surface processes such as adsorption, diffusion, and growth, as shown in Figure 1-2, a better understanding of these processes is important from an engineering perspective to govern the behaviors of a wide range of applications and from a fundamental science perspective to provide principles for future design.

1.2 Integration of Computational and Experimental Methods

The last two decades have witnessed a dramatic rise in computational resources that has facilitated tremendous progress in computational science. In particular, this progress has enabled the application of computational simulations to complement the experimental observations for capturing the process-structure-property relationship of an interested material. Various simulation methodologies have been developed to

elucidate materials behaviors over a wide length and time scale, as shown in Figure 1-3. For example, density functional theory (DFT), which is a quantum mechanical modeling method, may be used to predict complex interfacial phenomena such as wetting, adsorption, diffusion, and segregation for atoms, molecules and condensed phases. Because of its explicit treatment of electronic structure, it is further able to provide high-fidelity predictions, but unfortunately the computational cost increases rapidly with system size. Therefore, these calculations are limited to a relatively small number of atoms (<500). To overcome this limitation, classical empirical methods (also known as interatomic potentials) that model materials at the atomic and nanometer scale without explicitly treating electrons have been developed and employed in molecular dynamics (MD) and Monte Carlo (MC) simulations. Such simulations have been employed to examine device-sized systems and dynamical process that include the effects of temperatures and pressure, which is beyond the reach of quantum-based approaches.

The main strength of classical empirical potentials is their low computational cost relative to electronic structure calculations. Recently, computation of a system with over a trillion (10^{12}) atoms becomes a reality in MD simulations.¹⁸ In MD simulations, the motions of the particles in a system are predicted by solving Newton's equation of motion. Therefore, it is important that the interatomic potential, which is used to calculate energies and forces, is accurate and transferable in order to correctly describe the chemical and physics properties of materials under a variety of conditions. Over the last few decades, empirical potentials have been successfully developed for the specific type of chemical bonding within a given system. For example, Lennard-Jones (LJ)

potentials^{19, 20} are typically used to characterize van der Waals (vdW) interactions; embedded atom method (EAM) potentials^{21, 22} are typically used to describe metallic bonding; and Buckingham potentials^{23, 24} are typically used to model ionically bonded systems. Although these potentials and many others^{25, 26} describe the specific interactions for which they are parameterized very well, they are typically applicable to materials with only one type of bonding which prevents their widespread application to a system with different types of bonding.

One example is heterogeneous catalysis, as illustrated in Figure 1-4, which shows that catalytic driven chemical reactions involve several different interactions across interfaces such as reactant-metal and metal-metal oxide that may contribute to overall catalytic activity and selectivity. Therefore, a potential should not only capture multiple-bonding events and types but also correctly describe their relative strength. Recently, the charge-optimized many-body (COMB)²⁷⁻³⁰ potentials and reactive force field (ReaxFF)²⁷⁻³⁰ potentials have been developed to tackle this challenge and parameterized to include a wide range of elements and compounds, including heterogeneous systems.

The first-generation COMB (COMB1) potential was developed in 2007 by Yu *et al.*³¹ based on Tersoff potential²⁷ and the electronegativity equilibration (QEq) method proposed by Rappe and Goddard^{32, 33}. Later, to improve the description of interfacial structures and small molecules, the second-generation COMB (COMB2) potential in two different versions, COMB2A³⁴ and COMB2B²⁸, were developed. Recently, the third-generation COMB (COMB3)²⁹ potential was developed using terms from COMB2 potential³⁰ for electrostatic effects, the second-generation reactive empirical bond order

(REBO2)³⁵ potential for short-range interactions, and the coordination function that was developed for the REBO potential for MoS₂³⁶ systems. In particular, because of the replacement of the original Tersoff expression, which lacks the four-body dihedral term that is needed to capture the delocalized bonding in hydrocarbon systems, and with the short-range interaction terms used in REBO2, the COMB3 potential can be extended to C/H/O/N systems.³⁰

In this dissertation, the main objective is to apply and parameterize the COMB3 potential for various heterogeneous systems and investigate the underlying physics of the interfaces and surface phenomena. The interfaces phenomena will focus on the metal clusters growth on the metal oxide via deposition and the surface phenomenon will focus on the oxidation of metal nitride surfaces.

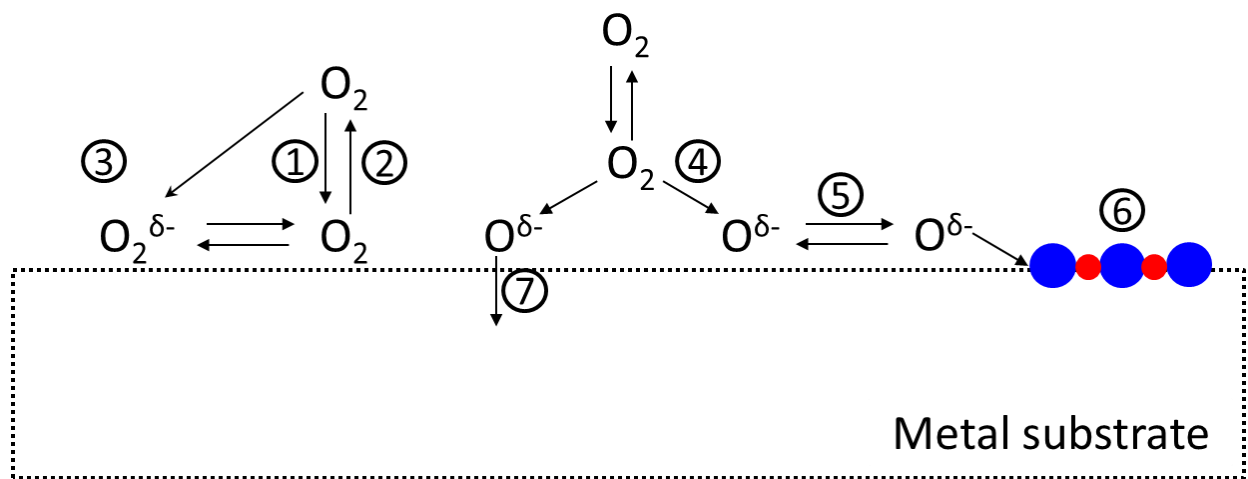
1.3 Outline

For a systematic study of this dissertation, the following chapters are organized as follows. Chapter 2 reviews the computational methods used throughout our investigated systems. Specifically, the formalisms and parameterization procedures for the COMB3 potential are thoroughly described. Chapter 3 presents the COMB3 potential development for the Cu/Zn and Cu/ZnO systems. This potential function is applied in MD simulations to model the deposition and subsequent evolution of Cu clusters on ZnO (10 $\bar{1}$ 0) in order to elucidate aspects of the growth mode of Cu on ZnO (10 $\bar{1}$ 0) that are currently the subject of controversy in the literature. Chapter 4 provides the COMB3 potential function for titanium (Ti) and titania (TiO₂). The Ti/TiO₂ potential successfully describes the properties of *hcp* Ti metal and rutile TiO₂. In addition, the phase orders of TiO₂ polymorphs and surface energies of various rutile surfaces are

well predicted compared to DFT calculations. The TiO_2 potential is further combined with the Cu/Cu₂O and Cu/Ti COMB3 potentials to examine the energetics of different-sized Cu clusters on rutile $\text{TiO}_2(110)$ surface. Chapter 5 provides the COMB3 potential function for TiN systems. The potential is further used to study the structural and adhesive properties of Ti/TiN interfaces and characterize the adsorption behavior of oxygen atoms and molecules on the TiN(001) surface. Chapter 6 discusses behaviors of adsorption and subsequent dissociation of O₂ on the AlN stepped surface investigated by DFT calculations. The results are further compared to behaviors of the flat surface. Lastly, the general conclusions of this collection of works and future applications of the COMB3 potential are given in Chapter 7.

Table 1-1. Characteristics of physical adsorption and chemisorption.¹³

Physical adsorption	Chemisorption
<ul style="list-style-type: none"> ▪ Weak van der Waals interactions ▪ The heat of adsorption are low (20 – 40kJ/mol) ▪ No electron transfer ▪ No dissociation of adsorbed species ▪ Nonspecific (insensitive to surface symmetry) ▪ Rapid, non-activated, and reversible ▪ Only significant at relatively low temperatures 	<ul style="list-style-type: none"> ▪ Strong chemical bonding ▪ The heat of adsorption are low (40 – 400kJ/mol) ▪ Electron transfer leading to bond formation ▪ May involve dissociation ▪ High surface symmetry specific (ex: steps) ▪ Slow, activated, and irreversible ▪ Over a wide range of temperatures



- ① Oxygen impingement (from gas phase)
- ② Molecular physisorption or desorption
- ③ Non-dissociative chemisorption ④ Dissociative chemisorption
- ⑤ Surface diffusion
- ⑥ Oxide formation ⑦ Oxygen dissolution

Figure 1-1. Initial oxidation processes of bare metal surfaces.

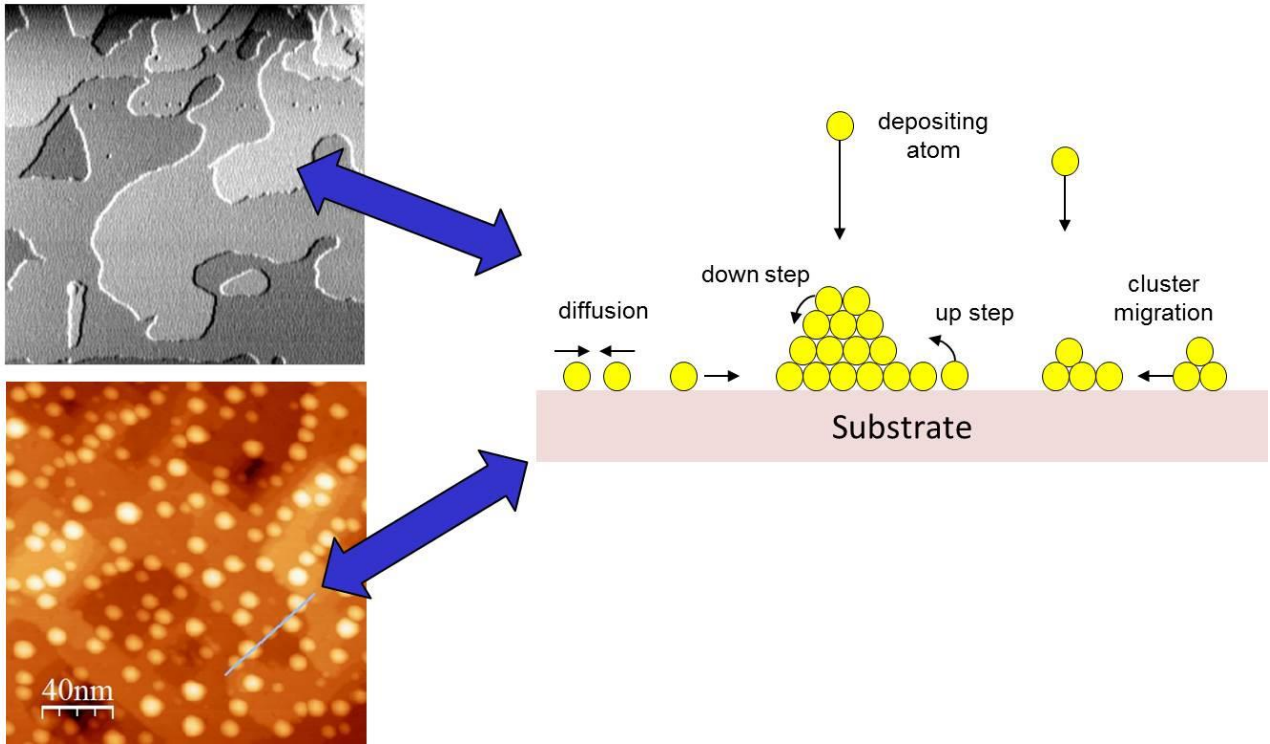


Figure 1-2. Surface processes of metal thin films or clusters growth on metal oxide substrate.^{37, 38}

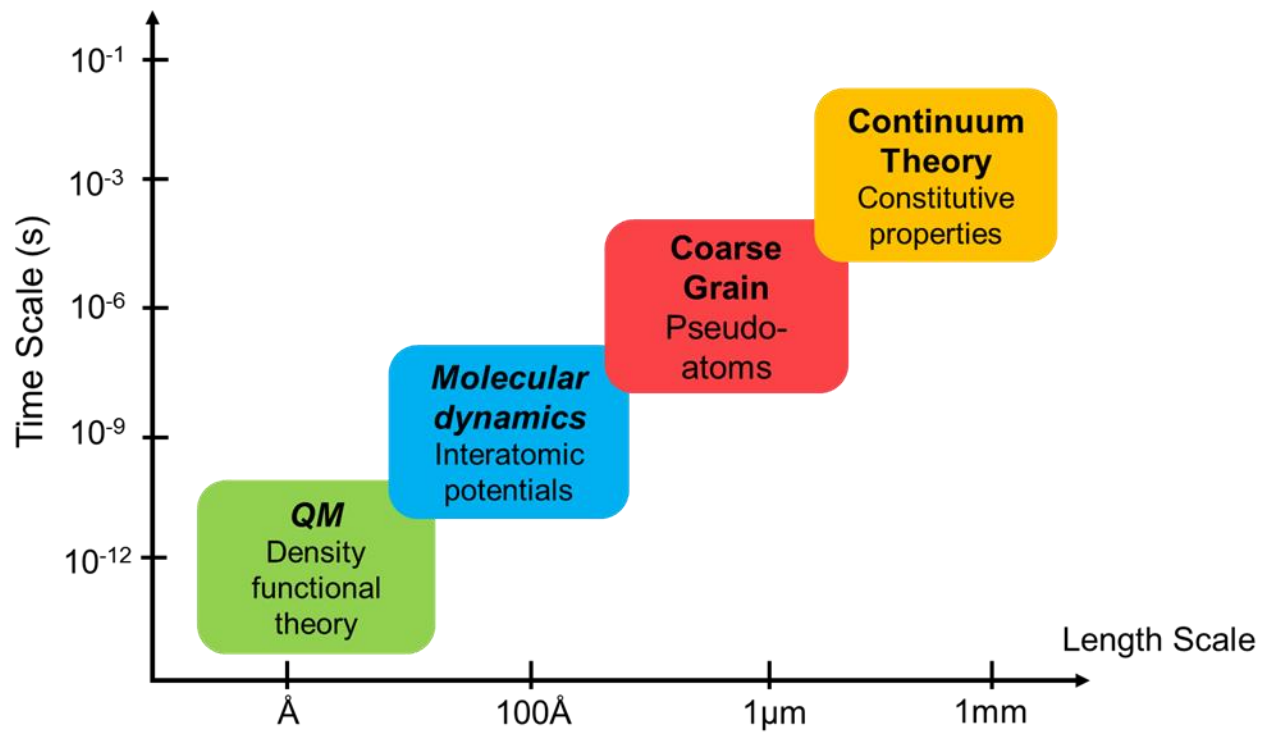


Figure 1-3. Hierarchy of multiscale modeling.

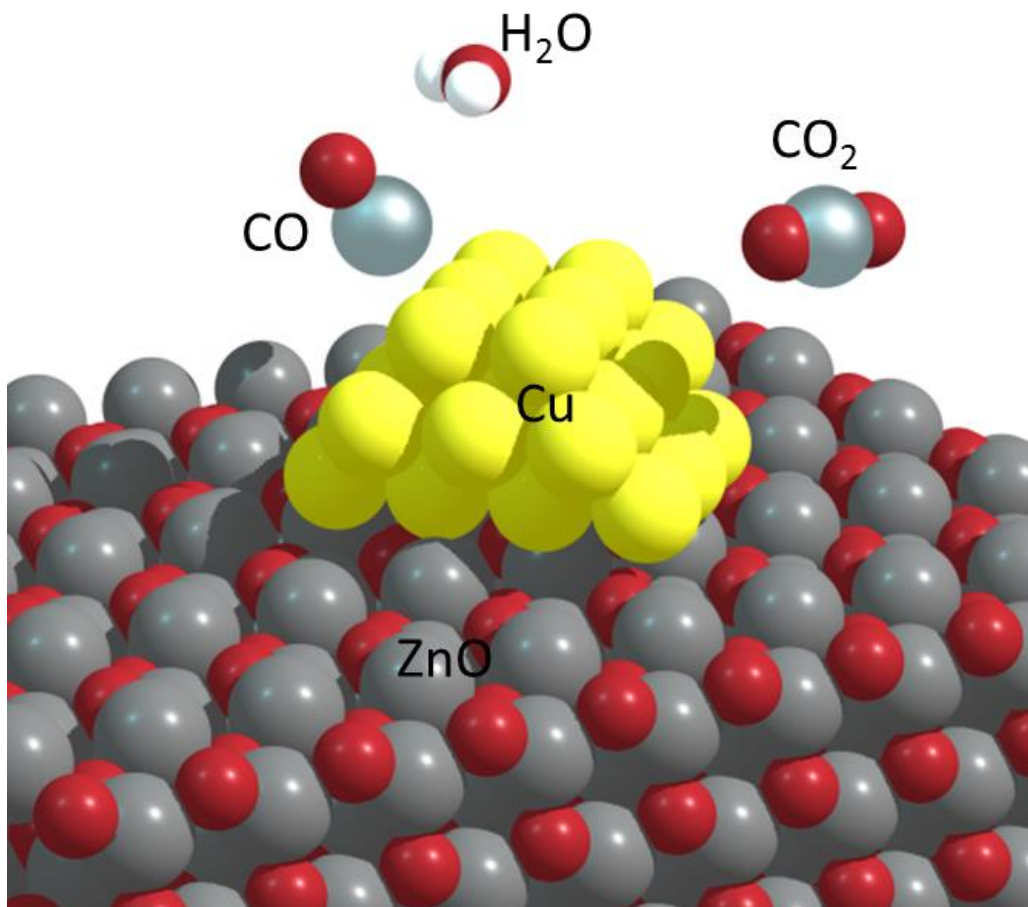


Figure 1-4. Snapshot of a molecular dynamics simulations of water, carbon monoxide, and carbon dioxide molecules interacting with a copper catalyst supported by a zinc oxide substrate. The element of Zn(grey), O(red), Cu(yellow), C(light blue) and H(white) is distinguished by color.

CHAPTER 2 COMPUTATIONAL METHODS

2.1 Computational Methods

Different types of computational methods exist that provide information regarding material properties from the electronic scale (e.g., density of states) to the structural scale (e.g., stress concentration). Therefore, understanding the advantages and limitations of different computational approaches is important for their proper application. Here, the fundamentals of density functional theory (DFT), which considers interactions between atoms and electrons explicitly, and classical atomic-scale methods, which consider interactions between atoms with interatomic potential functions, are discussed. These two approaches are also the main tools used in the computational work that forms the basis of this dissertation

2.2 Density Functional Theory

In density functional theory, the many-body electronic wavefunction Ψ of quantum mechanics is replaced with the electronic density $\rho(r)$ as the central quantity. The development of DFT is based on two theorems that were proposed by Hohenberg and Kohn in 1964.³⁹ The first theorem stated that, “*The external potential $v_{ext}(r)$, and hence the total energy, is a unique functional of the electron density $n(r)$* ”, which can be expressed as a one-to-one relationship between the external potential and the ground state electron density. The term “functional” refers to a function of a function, which means that the energy of a material has a functional dependence on single electron density, $\rho(r)$, and then $\rho(r)$ is a function of the positions of the electrons, r .

The second theorem stated that, “*The ground state energy can be obtained variationally: the total energy is the exactly ground density*”. In other words, the exact

ground state density of the system is that which minimizes the total energy. Therefore if we know the total energy functional in terms of the density, the ground state energy can be found by numerically minimizing this functional. However, neither theorem defined the functional.

Based on the Hohenberg and Kohn theorems, the electron density can be used to determine the ground state. However, we still need to determine the electron-electron interaction term of the Schrödinger equation. In 1965, Kohn and Sham⁴⁰ used the derivation of a set of equations that only involve single, non-interacting electrons. Therefore, the Schrödinger equation can be written in terms of the Kohn-Sham equations as:

$$\left[-\frac{\hbar^2}{2m_e} \nabla^2 + V(r) + V_H(r) + V_{XC}(r) \right] \Psi_i(r) = \varepsilon_i \Psi_i(r), \quad (2-1)$$

$$V_H(r) = e^2 \int \frac{n(r')}{|r-r'|} d^3r' \quad ; \quad V_{XC}(r) = \frac{\delta E_{XC}[n(r)]}{\delta n(r)}. \quad (2-$$

2)

The individual terms on the right side in Equation 2-1 are, in order, the kinetic energy of electron, the electron-nuclei potential, the electron-electron potential (also called the Hartree potential), and the exchange-correlation potential. $\Psi_i(r)$ is the wavefunction of state i that only depends on three spatial variables, and ε_i is the Kohn-Sham eigenvalue. In Equation 2-1, the exact functional for the exchange-correlation energy is the only unknown term. Therefore, reasonable approximations such as the local density approximation (LDA) and generalized gradient approximation (GGA), are required to solve this equation. These approximations have been shown to work well for most

material systems, with the notable exception of strongly correlated systems.⁴¹⁻⁴³ For more complete details regarding developments and applications of DFT, the reader is referred to Ref.⁴⁴

2.3 Classical Empirical Methods

2.3.1 Interatomic Potentials

In contrast to DFT, interatomic potentials are less computationally expensive because they only consider interactions between atoms without explicitly treating electrons. Through mathematical models, the energy of different types of bonding can be represented as functions of interatomic distance, electronic density, bond angles, charge, types of neighbors, and/or other factors. The most well-known is the Lennard-Jones (LJ) potential,^{19, 20} which was initially proposed for liquid argon and takes the form of Equation 2-2:

$$U(r_{ij}) = 4\varepsilon \left[\left(\frac{\sigma}{r_{ij}} \right)^{12} - \left(\frac{\sigma}{r_{ij}} \right)^6 \right], \quad (2-3)$$

where the r_{ij} (Å) is the interatomic distance between two atoms and the parameters of ε and σ are associated with the materials property. In addition, the r^{-12} term represents the short-range repulsion interaction from overlapping electron orbitals with equal spin (Pauli repulsion). In contrast, the r^{-6} term represents long-range van der Waals attraction.

A schematic curve of the LJ potentials energy (U) as a function of interatomic distance (r_{ij}) is shown in Figure 2-1 (a). The parameter, ε (eV), governs the strength of the interaction, where the minimum potential energy ε_{min} corresponds to an interatomic distance, σ (Å). In addition, the shape of the potential energy curve controls many of the

physical properties of materials, such as the bulk modulus and thermal expansion. A schematic curve of the force as function of interatomic distance is illustrated in Figure 2-1 (b), which are determined from the gradient of the interatomic potential energy and thus takes the form of Equation 2-3:

$$F(r_{ij}) = \left(\frac{48\varepsilon}{\sigma^2}\right)(r_{ij}) \left[\left(\frac{\sigma}{r_{ij}}\right)^{14} - \frac{1}{2} \left(\frac{\sigma}{r_{ij}}\right)^8 \right]. \quad (2-4)$$

From Figure 2-1 (b), it is clear that σ is the equilibrium interatomic distance, where the net forces are zero. Therefore, as indicated in Figure 2-1 (c), when the interatomic distance is larger or smaller than the equilibrium distance, an attraction or repulsion force acts and pushes both atoms until they reach an equilibrium distance.

Because of its computational simplicity, the LJ potential is extensively used. In modern materials modeling, it is best applied to describe the properties of gases or long-range interactions. Over the last few decades, empirical potentials using different mathematical expressions and various parameters for the potential function have been successfully developed for specific types of chemical bonding within a given system, as listed in Table 2-1. These potentials are then used to determine interatomic forces in, for example, molecular dynamics (MD) simulations.

2.3.2 Molecular Dynamics (MD) Simulations

MD simulation is used to investigate the dynamical properties of a system at the atomic scale. In this approach, the motion of each atom is described by solving Newton's second law:

$$F = m\bar{a} = m \frac{d^2 \bar{r}}{dt^2}, \quad (2-5)$$

$$F_i = -\frac{\partial U}{\partial r_i}, \quad (2-6)$$

where F is the force exerted on the atom, which can be determined from the gradient of the interatomic potential energy U . In addition, \vec{a} is the acceleration of the atom and \vec{r} is its instantaneous position. Therefore, both DFT and interatomic potentials may be used to determine interatomic forces within MD simulations, although the latter is more computationally efficient and therefore more commonly used. In addition, many numerical algorithms have been developed for integrating the equation of motion, such as the Verlet, leap-frog, and predictor-corrector.⁴⁵ In this dissertation, the Verlet algorithm is used.

2.3.3 Ensembles

MD is a statistical mechanics method, and it provides a way to obtain a set of configurations (atomic positions and momenta) distributed according to some statistical distribution function (an ensemble). Therefore, in an MD simulation, various thermodynamic ensembles are employed. Three common ensembles are: (1) *Microcanonical Ensemble* (NVE): used for an isolated system with N atoms, which keeps a constant volume (V) and a conserved total energy (E). (2) *Canonical Ensemble* (NVT): used for a system with N atoms in a temperature bath. The volume (V) and the temperature (T) of the system are kept constant. (3) *Isobaric Isothermal Ensemble* (NPT): used for an isolated system with N atoms in a temperature and pressure bath. The pressure (P) and the temperature (T) of the system are kept constant.

2.3.4 Periodic Boundary Conditions and Cutoff Radius

At current levels of computing power, MD simulations are routinely carried out on system sizes on the order of several nanometers. However, they are useful in showing atomic-scale details related to experimentally observed macroscopic systems. To mimic materials in the bulk or at surfaces, periodic boundary conditions (PBCs) are typically applied. In particular, three-dimensional PBCs are used to mimic a portion of a bulk system with no surfaces present. In contrast, simulations of planar surfaces make use of two dimensional PBCs within the plane of the surface; the third direction typically includes a vacuum region. In general, large systems can be more readily modeled with smaller atomic-scale systems through the use of PBCs.

Figure 2-2 illustrates PBCs in two dimensions. The system cell is repeated to mimic an infinite lattice and thus does not have edge effects. During the simulation when a particle moves in the system cell, the corresponding particle in each neighboring periodic cell moves in the same manner. If a particle leaves the system cell, say through the left boundary, one of its periodic images enters through the opposite side, the right boundary.

2.4 Variable Charge Reactive Potentials: COMB Potentials

2.4.1 General Formalism of the Third-Generation COMB Potentials

This section presents the general formalism of COMB potentials and describes how they are used to obtain a proper description of energy and charge for a multicomponent system. As show in Equation 2-7, the total potential energy ($U^{tot}[\{q\},\{r\}]$) of a system as described by the COMB potential is composed of electrostatic energy ($U^{es}[\{q\},\{r\}]$), short-range interactions ($U^{short}[\{q\},\{r\}]$), van der

Waals interactions ($U^{vdW}[\{r\}]$), and correction terms ($U^{corr}[\{r\}]$), where q and r represent the charge and coordinate array of the system, respectively.

$$U^{tot}[\{q\},\{r\}] = U^{es}[\{q\},\{r\}] + U^{short}[\{q\},\{r\}] + U^{vdW}[\{r\}] + U^{corr}[\{r\}] \quad (2-7)$$

2.4.2 Electrostatic Energies

The electrostatic energies ($U^{es}[\{q\},\{r\}]$) include the self-energy ($U^{self}[\{q\},\{r\}]$), the charge-charge interactions ($U^{qq}[\{q\},\{r\}]$), the charge-nuclear interactions ($U^{qZ}[\{q\},\{r\}]$), and the energies associated with atomic polarizability ($U^{polar}[\{q\},\{r\}]$), which are defined in Equation 2-8. The repulsion between nuclei is not explicitly formulated since their overall effects are assumed to be included in the short-range interactions

$$U^{es}[\{q\},\{r\}] = U^{self}[\{q\},\{r\}] + U^{qq}[\{q\},\{r\}] + U^{qZ}[\{q\},\{r\}] + U^{polar}[\{q\},\{r\}] \quad (2-8)$$

The self-energy ($U^{self}[\{q\},\{r\}]$) described the energy required to form a charge on an atom. This can be expressed by the summation of the ionization or electron affinity energy of an isolated atom ($V^{ionize}(q_i)$) and a correction function ($V^{field}(r_{ij}, q_i)$), termed the field effect⁴⁶, that reflects the change of electronegativity and atomic hardness of the atom with its environment, as specific in Equations 2-9, 2-10, and 2-11:

$$U^{self}[\{q\},\{r\}] = E_i^0(0) + \chi_i q_i + \left(J_i + \sum_{j \neq i}^N V_{ij}^{field}(r_{ij}, q_i) \right) q_i^2 + K_i q_i^3 + L_i q_i^4 \quad (2-9)$$

$$V_i^{ionize}(q_i) = E_i^0(0) + \chi_i q_i + J_i q_i^2 + K_i q_i^3 + L_i q_i^4 \quad (2-10)$$

$$V_{ij}^{field}(r_{ij}, q_i) = \frac{1}{2\pi\epsilon_0} \sum_{j \neq i}^{NN} \left(\frac{P_{ij}^Z q_j}{r_{ij}^3} + \frac{P_{ij}^J q_j^2}{r_{ij}^5} \right) \quad (2-11)$$

In Equation 2-10, as outlined by Toufar et al.,⁴⁷ the parameters χ is identified with the electronegativity, and J is associated with chemical hardness or self-Coulombic interaction,⁴⁷ which are inherent to each element. Therefore, χ_i , J_i , K_i , L_i are treated as atomic parameters and fitted to the ionization energies and electron affinities for each of the elements. In contrast, the parameters P_{ij}^χ and P_{ij}^J in Equation 2-11 are associated with specific bonds to describe the environmental dependence of field effects.

The long-range electrostatic interaction between two ions is normally described by Coulomb's Law, which is defined in Equation 2-12,

$$U_{ij}^{Coul}(q_i, q_j) = \frac{1}{4\pi\epsilon_0} \frac{q_i q_j}{r_{ij}} \quad (2-12)$$

However, as the distance between two ions approaches to zero, the Coulomb expression in Equation (2-6) results in infinite values, which was also called "Coulomb catastrophe". To avoid this Coulomb catastrophe that was introduced by a point charge model, COMB potentials adopt the Streitz-Mintmire³⁴ charge density function.

Specifically, the charge density of an atom is taken to be function of its charge, spatial location (r) and atomic position (r_i):

$$\rho_i(r_i, q_i) = Z_i \delta(|r - r_i|) + (q_i - Z_i) f_i(|r - r_i|) \quad (2-13)$$

$$f_i(|r - r_i|) = \xi_i^3 \pi^{-1} \exp(-2\xi_i |r - r_i|) \quad (2-14)$$

Z_i is an effective point core charge treated as a fitted parameters, δ is the Dirac delta function, $f(r)$ is a function that capture the radial decay of the electron density of the S-type orbital,⁴⁸ and ξ is an orbital exponent that controls the length scale associated with this decay. Further, the charge-charge interactions ($U^{qq}[\{q\}, \{r\}]$) can be calculated as

indicated in Equation 2-15 by the integration over electron densities between pairs of atoms through the Coulomb integral, J_{ij}^{qq} defined in Equation 2-16.

$$U^{qq}[\{q\},\{r\}] = \sum_i \sum_{j \neq i} q_i J_{ij}^{qq} q_j \quad (2-15)$$

$$J_{ij}^{qq} = [\rho_i | \rho_j] = \int d^3 r_1 \int d^3 r_2 \frac{\rho_i(r_1) \rho_j(r_2)}{r_{12}} \quad (2-16)$$

Where r_1 and r_2 indicate the centers of $\rho_i(r)$ and $\rho_j(r)$, and r_{12} is the distance between density distribution. Similarly, the charge-nuclear interaction $U^{qZ}[\{q\},\{r\}]$ are expressed in Equation (2-17) through the charge-nuclear coupling operator, J_{ij}^{qZ} , which is shielded nuclear attraction integral and defined in Equations 2-18 and 2-19.

$$U^{qZ}[\{q\},\{r\}] = \sum_i \sum_{j \neq i} (q_i J_{ij}^{qZ} q_j + q_j J_{ji}^{qZ} q_i) \quad (2-17)$$

$$J_{ij}^{qZ} = [j | \rho_i] - [\rho_j | \rho_i] \quad (2-18)$$

$$[j | \rho_i] = \int d^3 r \frac{\rho_i(r)}{|r - r_i|} \quad (2-19)$$

The Coulombic interaction in Equation (2-9) and (2-11) are solved via a direct Wolf summation method⁴⁹ which is more computationally efficient than the Ewald summation⁵⁰ for computing electrostatic interactions.

The polarizability, P , presents the relative tendency of an equilibrium charge distribution to be distorted in response to an external field, which is defined as the ration of the induced dipole moment, $\overline{\mu}$, of an atom to the electric field, \overline{E} . The inclusion of the polarization effects has been proven to be useful in classical simulations to stabilize the complex oxide structures such as α -alumina⁵¹ and to model the interactions with

small polarizable molecules such as water and oxygen molecules. Using the fluctuation dipole model by Sterne et al.,⁵² as specific in Equation 2-20, the polarization vector can be directly calculated from the electrostatic field generated by the atomic charges, \bar{E}_i^q , and the neighboring induced dipoles.

$$\bar{\mu}_i = P_i \bar{E}(\bar{r}) = P_i \left(\bar{E}_i^q + \sum_{j=1, j \neq i}^N T_{ij} \bar{\mu}_j \right) \quad (2-20)$$

$$\bar{E}_i^q = \frac{1}{4\pi\epsilon_0} \sum_{j \neq i}^N q_j \frac{\partial J_{ij}^{qq}}{\partial r} \frac{\bar{r}_{ij}}{|\bar{r}_{ij}|} \quad (2-21)$$

P_i is the polarizability tensor and T_{ij} is the induced dipole field tensor. Because the atomic polarizability is assumed to be isotropic, P_i thus reduces to a scalar value that is only associated with the elemental nature of the atom. The induced dipole field tensor (T_{ij}) is employed as a damped function that diminishes as atoms overlap.

$$T_{ij} = \frac{1}{4\pi\epsilon_0 |\bar{r}_{ij}|^3} \left(1 - 3 \frac{\bar{r}_{ij} \cdot \bar{r}_{ij}}{|\bar{r}_{ij}|^2} \right) \left[1 - e^{-2\xi_i r} (1 + 2\xi_i r_{ij} + 2\xi_j^2 r_{ij}^2) \right] \quad (2-22)$$

Lastly, as shown in Equation 2-23, the energies contributed from atomic polarizability are the dipole self-energy, the dipole-charge interaction, and the dipole-dipole interaction, respectively.

$$U^{polar} [\{q\}, \{r\}] = \sum_i \frac{\bar{\mu}_i^2}{2P_i} + \sum_i \bar{\mu}_i \cdot \bar{E}_i^q + \sum_i \sum_{j \neq i} \bar{\mu}_i T_{ij} \bar{\mu}_j \quad (2-23)$$

2.4.3 Short-Range interactions

The bond-order type short-range interactions, U^{short} , where the short-range repulsion energy, $V^R(r_{ij}, q_i, q_j)$, and attraction energy, $V^A(r_{ij}, q_i, q_j)$, are based on the

Tersoff⁵³ and Yasukawa⁵⁴ potentials, as briefly described in Equation 2-24. For the origin Tersoff potential, the short-range interaction is dependent on the interatomic distance (r). However, the short-range interaction in COMB potentials is not only exponentially decay with interatomic distance (r) but vary with charge (q). In Equations 2-25 and 2-26, the charge-dependent correction functions, $D_i(q_i)$, are added to the exponential term of the repulsion and attraction energies to reflect the change in atomic radius with charge. The change in the bond order with charge is reflected in the charge dependent function, $B_{ij}^*(q_i, q_j)$. In addition, the cut-off function, as described in Equation 2-27, adopts the cosine-decay formalism to smoothly terminate the short-range interactions, where R_{ij}^{\max} and R_{ij}^{\min} are the upper and lower cutoff distance.

$$U^{short}[\{q\}, \{r\}] = \frac{1}{2} \sum_i \sum_{j \neq i} \left\{ f_c(r_{ij}) \left[V^R(r_{ij}, q_i, q_j) - b_{ij} V^A(r_{ij}, q_i, q_j) \right] \right\} \quad (2-24)$$

$$V^R(r_{ij}, q_i, q_j) = A_{ij} \times \exp \left\{ -\lambda_{ij} r_{ij} + \frac{1}{2} \left[\lambda_{ii} D_i(q_i) + \lambda_{jj} D_j(q_j) \right] \right\} \quad (2-25)$$

$$V^A(r_{ij}, q_i, q_j) = B_{ij} B_{ij}^*(q_i, q_j) \times \exp \left\{ -\alpha_{ij} r_{ij} + \frac{1}{2} \left[\alpha_{ii} D_i(q_i) + \alpha_{jj} D_j(q_j) \right] \right\} \quad (2-26)$$

$$f_c(r_{ij}) = \begin{cases} 1 & r_{ij} \leq R_{ij}^{\min} \\ \frac{1}{2} \left(1 + \cos \left(\frac{r_{ij} - R_{ij}^{\min}}{R_{ij}^{\max} - R_{ij}^{\min}} \pi \right) \right) & R_{ij}^{\min} < r_{ij} \leq R_{ij}^{\max} \\ 0 & r_{ij} > R_{ij}^{\max} \end{cases} \quad (2-27)$$

The bond-order term (b_{ij}) uses a similar formalism that is used in the REBO potential⁵⁵ and includes the contributions from the bond angle (b^{angle}), coordination (b^{coord}), additional torsion ($b^{torsion}$), and conjugation ($b^{conjugat}$) effects from hydrocarbon

systems, which are used to capture many-body effects. Here, due to the complex bond environment of hydrocarbon system, the bond-order term only show the contribution from bond angle and coordination without torsion and conjugation effects, as shown in Equation 2-28. The detailed parameters and fitting procedure of the COMB potential for hydrocarbon system is described in ref.^{36, 56}

$$b_{ij} = \left[1 + \left(\sum_{j \neq i}^N \sum_{k \neq i, j}^N \zeta(r_{ij}, r_{ik}) g_{ij}(\cos(\theta_{ijk})) + P_{ij} \right)^{\eta_i} \right]^{\frac{-1}{2\eta_i}} \quad (2-28)$$

The asymmetric term $\zeta(r_{ij}, r_{ik})$ is used to weaken the longer bond. The angular function, $g_{ij}(\theta_{ijk})$, and the coordination function, P_{ij} , are described from Equations 2-29 to 2-31.

$$\zeta(r_{ij}, r_{ik}) = f_c(r_{ik}) \exp \left[\beta_{ij}^{m_i} (r_{ij} - r_{ik})^{m_i} \right] \quad (2-29)$$

$$g(\cos(\theta_{ijk})) = b_0 + \sum_{n=1}^6 b_n \cos^n(\theta_{ijk}) \quad (2-30)$$

$$P_{ij} = c_0 Z_i + c_1 e^{c_2 Z_i} + c_3 \quad (2-31)$$

In Equations 2-29 to 2-31, m_i , b_0 to b_6 and c_0 to c_3 are fitted parameters, and Z_i is the number of nearest neighbors of atom i .

2.4.4 van der Waals Interactions

The long-range van der Waals (vdW) interactions, ($U^{vdW}[\{r\}]$), are captured by the classical Lennard-Jones formula in COMB potential, and take the form of Equation 2-32:

$$U^{vdW}[\{r\}] = \sum_i^{NN} \sum_{j \neq i}^{NN} V^{vdW}(r_{ij}) = \sum_i^{NN} \sum_{j \neq i}^{NN} 4\epsilon_{ij}^{vdW} \left(\left(\frac{\sigma_{ij}^{vdW}}{r_{ij}} \right)^{12} - \left(\frac{\sigma_{ij}^{vdW}}{r_{ij}} \right)^6 \right) \quad (2-32)$$

In this expression, ϵ_{ij}^{vdW} and σ_{ij}^{vdW} reflect the strength and equilibrium distance of the vdW interactions, respectively. The vdW interactions are truncated and shifted to zero at the Coulombic cut-off radii. To avoid extremely high repulsion between short-range bonded atoms, a cubic spline function is added to smoothly terminate the vdW interactions at the upper end of short-range cut-off radii. For any binary vdW bonds, the ϵ_{ij}^{vdW} and σ_{ij}^{vdW} are decided by considering the geometric and arithmetic means of values of element-type vdW bonds, respectively.

2.4.5 Correction Terms

The correction terms, ($U^{corr}[\{r\}]$), are primarily used to modify the energy contribution from specific bond angles. In the set of correction terms, as described in Equation 2-33, they consist of Legendre polynomials (*LPs*) up to sixth order and a bond-bending (*BB*) term.

$$U^{corr}[\{r\}] = \sum_i^N \sum_{j \neq i}^N \sum_{k \neq i, j} \left\{ \sum_{n=1}^6 K_{ijk}^{LP_n} [\cos(\theta_{ijk})] + K_{ijk}^{BB} [\cos(\theta_{ijk}) - \cos(K_{ijk}^\theta)]^2 \right\} \quad (2-33)$$

The *LPs*, whose detailed forms can be found in ref.³⁰, are a set of symmetric energy penalties on the bond angle. In contrast, the bond bending term provides an asymmetric energy penalty on a specific bond angle, K_{ijk}^θ . For more detailed on the application of correction terms in COMB potentials, they can be found in refs⁵⁷. All the parameters in Equation (2-27) are three-dimensional, where the first subscript character (*i*) represents the element-type of the central atom.

2.4.6 Dynamic Charge Equilibration Method

The key development of COMB potential applicable to multiple types of bonding is a method for equilibration of charge. Although fixed-charged potentials work well for

bulk materials systems, they cannot describe systems that require charge equilibration, such as a heterogeneous interface between dissimilar materials. In COMB potential, the atomic charges are treated as dynamical variables evolving with time and are equilibrated based on the electronegativity-equilibration (EE) principle. This principle, which was proposed by Sanderson, states that in a closed system of interacting ions at chemical equilibrium, the electron density is distributed so that electrochemical potential is equal at all atomic sites. Based on the definition that the chemical potential (μ_i) for each site (atom) is equivalent to the partial derivative of the total energy (U^{tot}) with respect to electron density ($\rho(r)$): $\partial U^{tot} / \partial \rho(r)$, it is also equivalent to the negative of the electronegativity (χ_i) at each site. Therefore, the partial charge on each atom can be determined as that which corresponds to the equilibrium electronegativity.

To efficiently and explicitly determine the partial charge and position of each atom dependent upon time, an extended Lagrangian method developed by Rick et al. is employed in COMB potential. The Lagrangian for the system is:

$$L = \sum_{i=1}^N \frac{1}{2} m_i \dot{r}_i^2 + \sum_{i=1}^N \frac{1}{2} M_Q \dot{q}_i^2 - U^{tot}[\{q\}, \{r\}] - \lambda_L \sum_{i=1}^N q_i \quad (2-34)$$

In Equation 2-34, m_i , r_i , and q_i correspond to the mass, position, and charge of atom i , respectively. The first term on the right side is the kinetic energy associated with the physical movement of the ions. The second term is the kinetic energy of the charges with a fictitious charge mass (M_Q). The potential energy is defined in third term. The final term is the constraint, where λ_L is an undetermined multiplier that enforces the constraint to keep the charge in the system conserved.

From the Lagrangian, we can derive equations of motion for the atomic positions and charges as:

$$M_q \ddot{r}_i = \frac{-\partial U^{tot}}{\partial r_i} \quad (2-35)$$

$$M_q \ddot{q}_i = \frac{-\partial U^{tot}}{\partial q_i} - \lambda_L = -\chi_i - \lambda_L \quad (2-36)$$

Since the total charge is conserved in a system, it follows that:

$$\sum_i \ddot{q}_i = 0 \quad (2-37)$$

Therefore, solving the above two equations shows λ_L is equal to the mean electronegativity for the system, as shown in Equation 2-38.

$$\lambda_L = -\frac{1}{N} \sum_i \chi_i = -\bar{\chi} \quad (2-38)$$

This leads to Equation 2-36 can be rewired as Equation 2-39:

$$M_q \ddot{q}_i = \bar{\chi} - \chi_i \quad (2-39)$$

The partial charge on each atom is determined by iteratively solving the equations of motion with damping factor for each set of nuclear positions until the electronegativity (χ_i) on each atom is sufficiently close to the mean electronegativity ($\bar{\chi}$) of the system.

2.5 Parameterization of COMB Potentials

Although the COMB potential has a complex formalism for the potential energy, each component is indispensable to model multiple types of bonding within a given system. Based on the origin of the potential energy, the general procedure for parameterizing the COMB potential is performed as follows^{30, 58}: (1) creating the

database from published experimental data and/or electronic structure calculations; (2) parameterizing the pure systems (starting with the parameters of short-range interactions and then that of electrostatic energies); (3) parameterizing the binary systems (starting with the parameters of short-range interactions).

2.5.1 Creating the Database

The parameterization of COMB potential proceeds by optimizing its parameters against the fitting database. In order to allow it to be suitably transferrable between various systems, a fitting database that includes a wide ranges of pure and binary compounds of various phases needs to be considered in the parameterization process. Normally, the fitting database for pure system consists of bond length (or lattice constant), elastic constants, cohesive energy and for binary systems consist of atomic charge and heat of formation. The fitting database should also comprise data from systems with a variety of coordination numbers to provide a good description of the bond-order dependence, which therefore consists of different defected and surface structures. In addition, for different focus of studies, the database such as transition state energy for atomic diffusion can be added into parameterization process.

The properties of these systems are obtained from published experimental data and/or the electronic structure calculations. For crystalline structure, the electronic structure calculations are performed with plane-wave DFT calculation using the software of Vienna *ab initio* Simulation Program (VASP)⁵⁹⁻⁶² with appropriate pseudopotential and exchange-correlation function (US-LDA or PAW-PBE). For molecular systems, the electronic structure calculations are performed using the Gaussian09⁶³ computational chemistry software package.

2.5.2 Parameterization of Pure Systems

Because the electrostatic energy terms for an uncharged pure system (such as bulk structures) is zero, the energy contribution of COMB potential for such a system is only from the short-range interactions (Equation 2-18) and the formalism is reduced to the Tersoff type of potential. In this case, this is straightforward for the parameterization of COMB potential, which only fitting parameters in the pairwise term and bond-order term, as shown in Table 2-1. The van der Waals interaction will be considered in hydrocarbon systems.

After fitting the parameters in the short-range interactions, the second step is to determine the charge-associated parameters of an atom. The involved parameters for this step are listed in Table 2-2. The fitting process for this step is achieved through the following three sub-steps: (1) fitting χ_i, J_i, K_i, L_i to the electron affinity and first, second, and third order of ionization energies of an isolate atom; (2) fitting the atomic polarizability, P_i , from the atomic polarization in a bonded dimer system; (3) fitting the rest of the parameters to the reaction energies of inserting or detaching an electron from the dimer system

2.5.3 Parameterization of Binary Systems

Lastly, the COMB potential is fit to the binary system with multiple phases. Similar to the parameterization process for pure system, the potential starts with fitting the pairwise terms to the phase orders and charged of variety of binary systems, which is followed by fitting the parameters in many-body terms for the properties of the phase of interest. The involved parameters for the binary systems are listed in Table 2-3.

2.6 Transition State Search: Dimer Method

Long-time simulations of system evolution require approaches other than traditional MD, such as a kinetic Monte Carlo (KMC) scheme. In a typical KMC simulation, the energetics of all transitions that might occur in the system must be known. By contrast, methods such as the string approach⁶⁴ and nudged elastic band (NEB)⁶⁵ method are used to identify transition states. However, the requirement of knowing the initial and final state limits the application of these approaches to simple systems. In the present work, to further evaluate the capability of the COMB potential and to characterize the transition states of Cu motion on the ZnO surface, the dimer method developed by Henkelman and Jónsson⁶⁶ is utilized. In the dimer method algorithm, effective forces are used to move along the lowest curvature direction in order to find the saddle point. Because the dimer method uses only the first derivatives of the potential and the initial state, it is computationally efficient.

The diffusion of Cu adatom on the Cu(100) surface has been investigated extensively in experiments^{67, 68} and simulations.⁶⁹⁻⁷² Therefore, this system is used as a first test of our implementation of the dimer method with the COMB potential. In MD simulations with the embedded atom method (EAM) potential, Liu et al.⁷⁰ predicted the migration barriers for the hopping and exchange mechanisms of Cu on Cu(100) to be 0.38 eV and 0.72 eV, respectively. Hanson et al.⁶⁹ also examined these mechanisms with DFT calculations and found that the hopping mechanism had an activation energy of 0.69 eV, compared to 0.97 eV for the exchange mechanism. In the present work, the Cu(100) surface consists of 864 atoms, 72 atoms per layer in 12 layers. A single Cu adatom is placed in a 4-fold hollow site which is the site with the highest adsorption energy. Approximately 20 Å of vacuum is used to prevent interaction between the top

layer and a periodic image of the bottom layer. In addition, only the Cu adatom and first-layer atoms are allowed to move freely. Figure 2-3 shows the two transition mechanisms for hopping and exchange as predicated by the COMB potential. The predicted migration barriers are 0.42 eV and 0.53 eV, respectively, which are in qualitative agreement with experimental findings, prior EAM simulations and DFT calculations. This test illustrate that the COMB potential is able to predict the correct transition mechanisms of Cu on the Cu (100) surface.

2.7 Summary

Generally, the COMB potential has thirty element-typed (or called one-dimensional) parameters for each element, thirty-two bond-typed (two-dimensional) parameters for each bond, and additional bond-angle-typed (three-dimensional) parameters, which is optional, for correcting the energy contribution from specific bond angles. This design is important to allow parameters to be flexible and transferable in a multicomponent system. Therefore, for the COMB potential, there is no re-parameterization needed of previous parameters when the potential is expanded to include more components or when new binary systems are examined. Therefore, relatively speaking, the parameterization of COMB potentials is more challenging than traditional interatomic potentials because of its considerable fitting database and parameters. We have therefore developed an in-house code called Potential Optimization Software for Materials (POSMAT) ⁵⁸ to speed up the parameterization process by utilizing a shared memory parallelization scheme. In addition, the COMB potential is currently implemented in the Large-scale Atomic/Molecular Massive Parallel Simulator (LAMMPS) ⁷³ packages distributed by Sandia National Laboratories. This availability allows the COMB potentials being capable of simulating system larger than

10^6 atoms at nanosecond timescale. A comparison of the performance of the COMB potential and other many-body potentials within LAMMPS can be found in Ref.⁷⁴

Table 2-1. The common used interatomic potentials.⁷⁵

Potentials	Formalisms	Application
<i>Lennard-Jones</i> ²⁰ (1924)	$V_{ij} = 4\varepsilon \left[\left(\frac{\sigma}{r} \right)^{12} - \left(\frac{\sigma}{r} \right)^6 \right]$ <p>The constants of σ and ε are dependent on the physical property of materials.</p>	Mostly suitable for rare gases
<i>Buckingham</i> ²³ (1938)	$V_{ij} = A \left\{ \exp(-Br_{ij}) \right\} - \frac{C}{r_{ij}^6}$ <p>The constants of A and r_0 are dependent on the physical property of materials.</p>	Mostly suitable for covalent bonding
<i>Embedded-Atom Method (EAM)</i> ²² (1984)	$E_{tot} = \sum_i G_i(\rho_{h,i}) + \frac{1}{2} \sum_{i,j} V_{ij}(r_{ij})$ <p>$\rho_{h,i}$ is the total electron density at the atom i due to the rest of the atom in the system. r_0 are constants dependent on the materials.</p>	Mostly suitable for metals
<i>Tersoff</i> ³² (1988)	$V_{ij} = V_r(r_{ij}) - B_{ij}V_a(r_{ij})$ <p>V_r and V_a are the potentials due to repulsive and attractive forces between atoms i and j; B_{ij} is a bond-order parameter which takes the many-body effects into account.</p>	Mostly suitable for covalently bonded materials
<i>Reactive empirical bond-order (REBO) potential</i> ⁵⁶ (1990)	$E_b = \frac{1}{2} \sum_{i \neq j} f_c(r_{ij}) \left[V^R(r_{ij}) - b_{ij} V^A(r_{ij}) \right]$ $= \frac{1}{2} \sum_{i \neq j} f_c(r_{ij}) \left[\left(1 + \frac{Q}{r} \right) A e^{-\alpha \cdot r_{ij}} - b_{ij} B_{ij} e^{-\beta \cdot r_{ij}} \right]$	Mostly suitable for covalently bonded materials and hydrocarbon

Table 2-2. List of fitting parameters for the pure systems.

Parameters	Descriptions	Equations
$A_{ii}, B_{ii}, \lambda_{ii}, \alpha_{ii}$	pairwise term	2-19, 2-20
η_i, m_i	in bond order term	2-28, 2-29
β_{ii}	asymmetric term	2-29
b^{ang-0} to b^{ang-6} for ii bond	bond angle term	2-30
c_0 to c_3 for ii bond	coordination term	2-31
$\varepsilon_{ii}^{vdW}, \sigma_{ii}^{vdW}$	vdW interaction	2-32
K_{iii}^{LP} to K_{iii}^{LP} , K_{ii}^{BB} and K_{iii}^{θ}	correction functions	2-33

Table 2-3. List of fitting parameters for the charge-dependent energy terms.

Parameters	Descriptions	Equation
χ_i, J_i, K_i, L_i	ionization energy	2-10
P_{ii}^{χ}, P_{ii}^J	field effects	2-11
Z_i, ξ_i	Coulomb interaction	2-13, 2-14
P_i	atomic polarizability	2-20
$D_{Ui}, D_{Li}, Q_{Ui}, Q_{Li}$	charge-dependence on short range	2-25, 2-26

Table 2-4. List of fitting parameters for the binary systems.

Parameters	Descriptions	Equation
$P_{ij}^{\chi}, P_{ij}^J, P_{ji}^{\chi}, P_{ji}^J$	field effects	2-11
$A_{ij}, B_{ij}, \lambda_{ij}, \alpha_{ij}$	pairwise short-range	2-19, 2-20
β_{ij}, β_{ji}	symmetric term	2-20
b^{ang-0} to b^{ang-6} for ij and ji bonds	bond angle term	2-30
c_0 to c_3 for ij and ji bonds	coordination term	2-31
K_{ijk}^{LP} to K_{ijk}^{LP} , K_{ijk}^{BB} and K_{ijk}^{θ}	correction functions	2-33

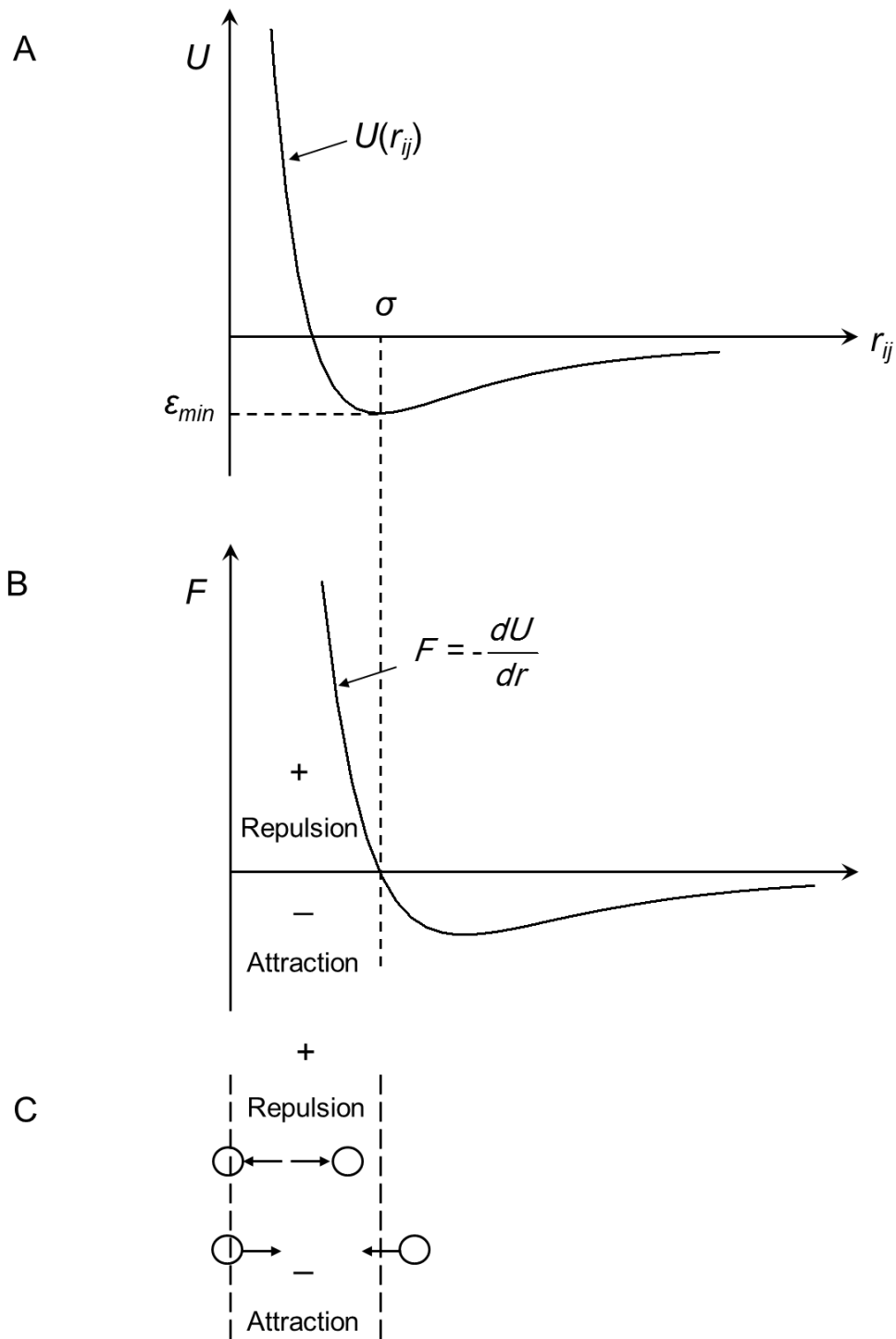


Figure 2-1. Lennard-Jones (LJ) potential. A) Energy function, B) force function, C) illustration of repulsion and attraction forces when an atomic distance is below or over the equilibrium distance.

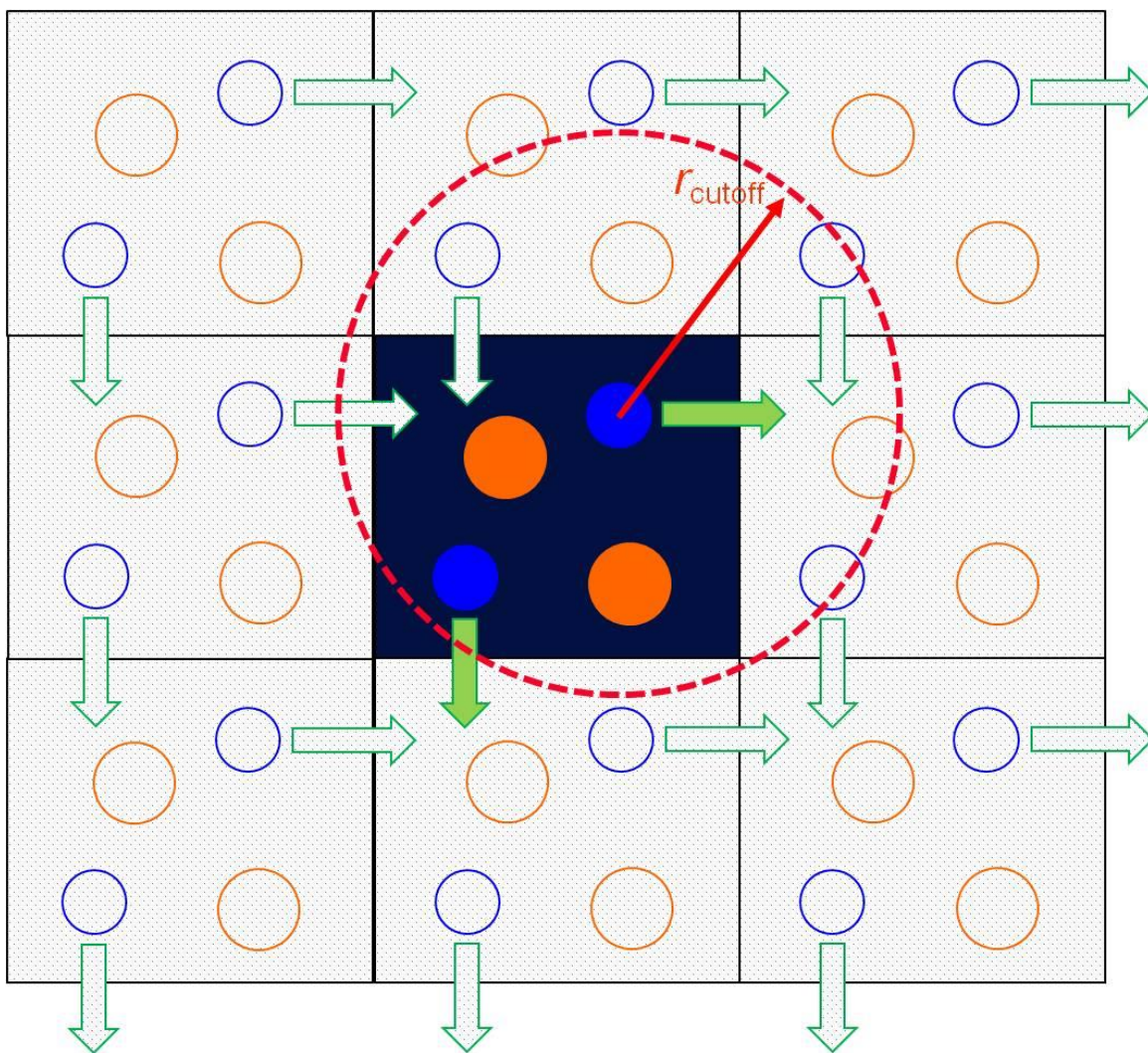
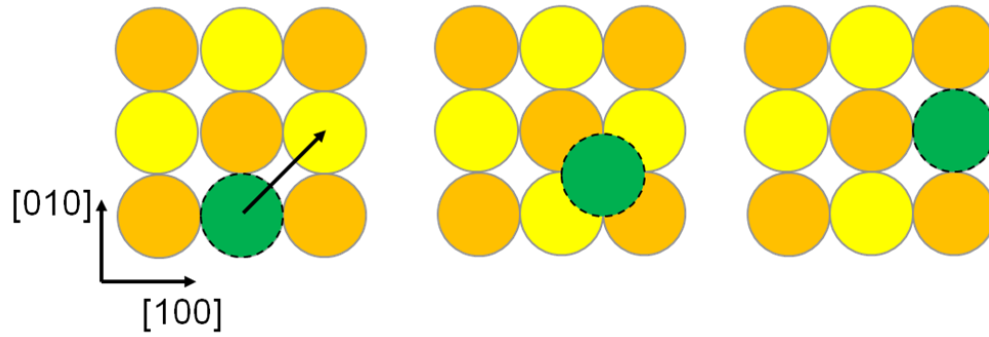


Figure 2-2. Schematic representation of periodic boundary conditions in MD simulations. The square with dark background represents the simulation cell, and the others are the images.

A



B

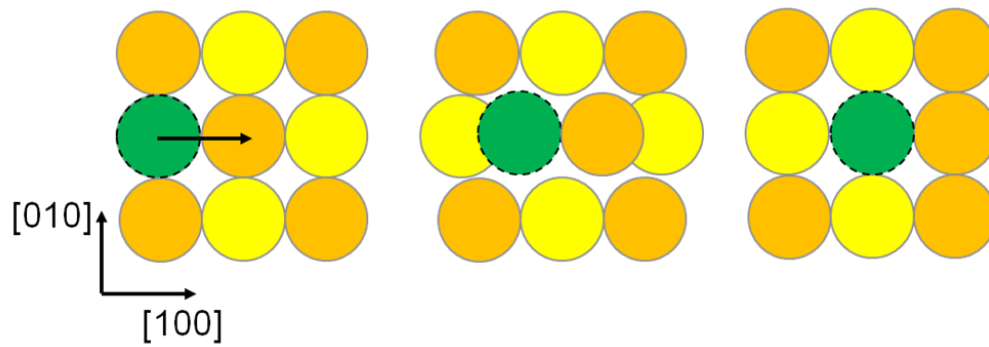


Figure 2-3. The two migration mechanisms of single Cu atom on Cu(100). A) Hop, B) exchange. The top schematic views, shown from left to right, are the initial state, saddle points, and final state, respectively. The yellow spheres are sublayer atoms, the orange spheres are surface atoms, and the green sphere is an adatom.

CHAPTER 3

DEVELOPMENT OF COMB3 CU/ZNO POTENTIAL AND ITS APPLICATION ON CU CLUSTERS DEPOSITION ON ZNO SURFACE

Methanol (CH_3OH) is a potential candidate for the next generation of renewable green fuels because its energy density is sufficiently close to that of gasoline. In addition, methanol exists in liquid form at ambient pressures and temperatures, which makes it easier to store and transport than hydrogen. Methanol synthesis from the hydrogenation of CO_2 is performed commercially using $\text{Cu/ZnO/Al}_2\text{O}_3$ catalyst. Despite numerous experimental and theoretical studies, there are still questions about the nature of the active site of the Cu/ZnO catalysts. Cu metal clusters,⁷⁶ Cu^+ ,⁷⁷⁻⁸⁰ the Cu/ZnO interface,⁸¹⁻⁸³ and Cu-Zn ⁸⁴ alloys have all been proposed as the active site. In addition, different sites might be active for CO_2 hydrogenation versus CO .^{82, 83, 85} While Cu/ZnO has been used in syngas hydrogenation, there is recent interest in using such catalysts in electrochemical reduction of CO_2 to produce methanol. This interest is motivated by studies that show that Cu oxide can electrochemically reduce CO_2 to methanol.⁸⁵ Le and co-workers have correlated methanol formation on the Cu oxide electrodes to the presence of Cu^+ sites.^{8, 86, 87} However, Cu oxide electrodes are inherently unstable in the reducing condition and methanol production tapers off with time as the oxide is reduced to metal. Recent results suggest that Cu on ZnO could lead to higher methanol formation rates but the nature of the active site and the stability of such catalysts still need to be explored.⁸

Since the morphologies of Cu cluster on ZnO surfaces can undergo dynamic changes, it is challenging to experimentally specify the state of the active sites under reaction conditions. Thus, to elucidate the formation of methanol on Cu/ZnO catalysts, the first step is to characterize the behavior of Cu atoms on ZnO surfaces. There have

been several surface science studies to characterize Cu growth and stability on polar⁸⁸ and nonpolar ZnO surfaces.^{37, 89-93} The polar ZnO surfaces are known to undergo complex reconstructions⁹⁴ and are therefore more difficult to examine using density functional theory (DFT). Consequently, the majority of the DFT work⁹⁵ has been focused on understanding Cu behavior on the ZnO(10 $\bar{1}$ 0) and ZnO(11 $\bar{2}$ 0) surfaces. Hu et al.^{96, 97} investigated Cu deposition and subsequent growth on the ZnO(10 $\bar{1}$ 0) and ZnO(11 $\bar{2}$ 0) surfaces using DFT. Their results indicate that Cu atoms strongly interact with ZnO becoming slightly positively charged between those suggested by Klier⁹⁷ (Cu⁺) and by Fleisch⁹⁸ (Cu⁰). It was suggested that the charged Cu atoms and the Cu-Zn sites might be the active sites of the system.

While first principles methods, such as DFT, provide high fidelity because of their explicit treatment of electronic structure, they are limited in the size and time scales that can be addressed directly. Because of the potential importance of large-scale changes of the Cu/ZnO interface (sintering of Cu metal, alloying with the oxide surface, oxidation of Cu metal, and adsorbate-induced surface reconstruction) on the catalytic activity, a computationally more efficient method is needed. One potential option is the development of potentials (reactive force fields) that are able to capture charge transfer within a system (such as at the Cu and ZnO at the interface) but still allow for much more rapid computation than DFT methods. Recently, the reactive force field (ReaxFF) method⁸⁶ has been applied to model related complex reactive systems including ZnO/water⁹⁹ and Cu/Cu₂O/water.^{100, 101} However, as yet these potentials have not been directly applied to the Cu/ZnO system.

Here, a third-generation charge-optimized many-body (COMB) potential for ZnO is developed and used to model the ZnO(10 $\bar{1}0$) surface interacting with either a single Cu adatom or a beam of deposited and equilibrated Cu clusters in classical molecular dynamics (MD) simulations. The use of a reactive potential with dynamic charge,¹⁰² such as COMB, in the simulations under temperature and pressure conditions that are similar to those in the experiments is necessary to fully describe the potential nanometer-scale changes at the interface, including sintering of the Cu clusters, alloying with the oxide surface, and oxidation of the Cu during the growth process. The COMB predictions for ZnO properties and of adsorption and migration energies of Cu atoms on the ZnO(10 $\bar{1}0$) surface are compared to published experimental data and to the results of density functional theory (DFT) calculations. In addition, the MD simulation results are compared with STM results to explain some puzzling experimental observations. The simulations further explore the way in which the growth mode and final morphology of the Cu clusters are influenced by changes in the Cu incident deposition energy and surface temperature. Cu growth on ZnO is also compared to Cu growth on Cu to determine how the nature of the surface influences the predictions.

3.1 Potential development and Properties of Cu/ZnO

3.1.1 Fitting Procedure

To ensure the phase stability of ZnO polymorphs, in addition to the wurtzite phase, another three phases of ZnO were explored: zincblende ($CN_{Zn,O}$: 4), rocksalt ($CN_{Zn,O}$: 6), and caesium chloride ($CN_{Zn,O}$: 8) were considered. Since the bond lengths (Zn-O: 1.99 Å vs. 2.00 Å) and bond angles (Zn-O-Zn: 108.55° and 110.38° vs. 109.47°) of wurtzite and zincblende are similar, there is only a small difference in cohesive

energy between two phases. The DFT-PBE calculations predict that the energy of the zincblende phase is only 0.014 eV per ZnO unit higher than that of wurtzite phase, which is similar to the energy difference calculated using the local density approximation (LDA) and generalized gradient approximation (GGA) (about 0.015 and 0.013 eV, respectively). The parameters for ZnO COMB potential were obtained through fitting to the data set including the energy dependence on volume of four ZnO polymorphs, elastic constants, and surface energies from experiments and DFT calculations

3.1.2 Predicted Properties of ZnO polymorphs

Table 3-1 compares the properties of lattice constants, elastic constants, and cohesive energy for various ZnO polymorphs predicted by the COMB2 and COMB3 potentials with values from experiments, DFT calculations and other empirical potentials. It is clearly shown that the newly developed COMB3 potential exhibits good predictions as COMB2 potential on the cohesive energy and the elastic constants of the wurtzite phase. Most importantly, the incorrect surface energy predictions of the COMB2 potential have been improved in the new COMB3 potential, where the polar surfaces of wurtzite ZnO have higher cleavage energies than nonpolar surfaces. Nevertheless, because the stabilization effect for the ideal termination of the polar surfaces of ZnO involves charge compensation of the surface layers, the cleavage energy for the polar surfaces is not quantitatively captured in the current COMB potential. Therefore, in future work incorporating data related to the polar surfaces, such as cleavage energies or reconstructed surfaces, may improve the COMB potential description of the polar surfaces.

3.1.3 Predicted Properties of CuZn alloys

The Cu–Zn interactions in COMB3 are explicitly parameterized for three specific Cu–Zn alloys,^{103, 104} which are the α -brass Cu₃Zn (fcc), β -brass CuZn (bcc), and γ -brass Cu₅Zn₈(*c*/52) phases, respectively. Table 3-2 lists the COMB3 predictions and makes a comparison to DFT and published experimental data. The heat of formation for the γ phase is properly calculated to be the lowest and the phase order prediction is correct. Although the bulk modulus of the γ phase is predicted to be larger than that measured experimentally, the correct phase order is of more importance because of the focus on potential alloying during cluster deposition and metal thin film growth rather than mechanical properties of this alloy.

3.2 Interaction of Cu on ZnO(10 $\bar{1}$ 0)

3.2.1 Adsorption Energies of Cu Adatom on ZnO(10 $\bar{1}$ 0)

Several computational studies¹⁰⁵ of Cu interacting with the ZnO(10 $\bar{1}$ 0) surface have been carried out. For example, Beltràn *et al.*^{96, 97, 106, 107} examined Cu adsorption directly on top of O and Zn surface atoms using Hartree-Fock theory and predicted that adsorption on O was slightly more favored than adsorption on Zn. Subsequently, Hu *et al.*⁹⁶ and Hellström *et al.*⁹⁷ performed more extensive DFT calculations that allowed for geometry optimization and predicted three possible adsorption sites for Cu on ZnO (10 $\bar{1}$ 0), as illustrated in Figure 3-1. Their calculations further predicted that site 2 in Figure 3-1 was considerably more stable than sites 1 and 3. These three adsorption sites are investigated here with the COMB3 potential.

Table 3 lists the adsorption energies and charges of single Cu atoms at these sites; a more positive value corresponds to a more stable configuration. The COMB3

potential predicts that the most favorable adsorption site is site 2 and the least favorable is site 1, which is consistent with the published DFT results ¹⁰⁷ at low Cu coverage. In addition, the atomic charges on the absorbed Cu is predicted to be higher at site 2 than at the other two sites, which correlates with the strong interaction between Cu and two O atoms.

3.2.2 Migration barriers of Cu Adatom on ZnO(10 $\bar{1}0$)

To characterize the migration of a single Cu atom on the ZnO(10 $\bar{1}0$) surface, the dimer method ¹⁰⁷ was employed to characterize its transition path. Table 4 lists the barriers for Cu atom migration from site 2 to sites 1 and 3. Although the barriers predicted by COMB3 are higher than those predicted by DFT ¹⁰⁸, the two sets of barriers are in qualitative agreement with one another. Specifically, both predict that Cu atom migration along the [12 $\bar{1}0$] direction is more energetically favorable than along the [0001] direction.

The relative stability of different sized copper clusters on the ZnO(10 $\bar{1}0$) surface can be characterized by the binding energy. The binding energy (E_b) per atom may be calculated using the following standard expression,

$$E_b = \frac{1}{n} [E(Cu_n) + E(ZnO) - E(Cu_n / ZnO)] \quad (3-1)$$

where n is the number of Cu atoms, $E(Cu_n/ZnO)$ is the total energy of Cu_n adsorbed on the surface, and $E(Cu_n)$ and $E(ZnO)$ are energies of Cu_n clusters and the optimized bare ZnO surface, respectively. The more positive value of E_b corresponds to a more stable species. Figure 3-2 illustrates the binding energy for Cu_n ($n=2-5$) clusters predicted by DFT calculations and COMB potential, which shows a fairly good correlation between

the values from DFT and COMB based on the estimation of linear trendline (R-squared value is 0.983). This result also indicates that, not surprisingly, Cu prefers to exist as a cluster than remain as an individual atom on this ZnO surface. Figure 3-3 shows the charge configuration of flat and planar Cu₅ clusters on ZnO(10 $\bar{1}0$), which indicates that the charge dependence of Cu clusters in different configurations.

From the above analyses it is clear that the COMB potential correctly describes the adsorption and migration of Cu atoms on ZnO(10 $\bar{1}0$). Therefore, in the next section, this potential is used to elucidate Cu thin-film growth via deposition for homogeneous and heterogeneous interfacial systems.

3.3 Cu Clusters Deposition on ZnO(10 $\bar{1}0$)

3.3.1 Details of the MD Simulation of Cluster Deposition and Relaxation

Classical MD simulations are used to model Cu₆ deposition on the ZnO(10 $\bar{1}0$) surface, where the forces on the atoms are determined via the COMB3 potential. Figure 3-4 shows the deposition system which is composed of deposited Cu clusters and a ZnO surface slab. The dimensions of the ZnO surface slab are 72 Å × 74 Å × 70 Å and it consists of 36960 atoms; the [10 $\bar{1}0$] direction is perpendicular to the plane of the surface. Periodic boundary conditions are imposed in the [12 $\bar{1}0$] and [0001] directions to simulate an infinite surface. There are three types of atoms in the slab: fixed, thermostat, and active atoms. The fixed atoms comprise the bottom four layers (~ 10 Å), and are held fixed in their bulk lattice sites to prevent the surface slab from translating as a result of the cluster deposition process. The middle fourteen layers (~ 30 Å) of ZnO are thermostat atoms, and have a Langevin¹⁰⁷ thermostat applied to them to dissipate the excess energy from the deposited clusters and maintain a constant surface

temperature of 300 K. The active region comprises the top eight layers of the slab and evolves under unconstrained equations of motion.

The motion of the thermostat and active atoms are determined by Newton's equations of motion, which are solved by using a Verlet algorithm¹⁰⁹ with a time step of 0.20 fs. The incident beam consists of Cu₆ with a stable octahedral structure that are deposited at a rate of 15.1 atoms/ps, which is on the same order as the experimental value of 10.3 atoms/ps.¹¹⁰ The kinetic energy of the clusters is 1.25 eV per atom, and the fluence is 4.5 J/cm². All of the MD simulations are performed using the LAMMPS¹¹¹ software.

3.3.2 Surface Morphology and Growth Mode

Figure 3-5(a) illustrates the morphology of the ZnO surface following the deposition of the equivalent of one monolayer (ML) of Cu, which corresponds to 600 Cu atoms. The surface Cu atoms are colored by their height above the ZnO surface to distinguish the monolayer-high 2D and multilayer-high 3D Cu clusters from one another, as illustrated in Figure 3-5(b). The MD simulations clearly predict that both 2D and 3D Cu clusters are formed following deposition.

To clarify the mechanisms associated with thin-film growth, Figure 3-6 illustrates the way in which the surface morphology of the Cu varies with coverage from 0.2 to 1 ML. Initially, at 0.2 ML, the deposited Cu atoms mostly maintain their cluster form on the surface while sometimes breaking into smaller clusters or even individual atoms following their initial impact on deposition. Because the incident energy is able to provide the energy that adatoms require to overcome migration barriers on ZnO[10 $\bar{1}$ 0],

adjacent Cu adatoms are able to migrate along the $[12\bar{1}0]$ direction and further coalesce into larger 2D Cu clusters.

When the Cu coverage reaches ~ 0.4 ML, a substantial fraction of the surface is covered by 2D Cu clusters. However, the formation of a second layer of Cu is also predicted, as indicated by the circle in Figure 3-6; this is the start of 3D structure formation. At this stage, the simulations predict that the deposited Cu clusters increase the area of the 2D clusters when they land on either the edge of existing 2D clusters and diffuse down to the lower terrace, or on the clean ZnO surface, as indicated in Figure 3-7(A). In contrast, when the deposited Cu land around the center of existing 2D clusters, they stick. This leads to the formation of the second-layer Cu atoms, as shown in Figure 3-7(B). These two behaviors may be further explained by the competition between diffusion energy and the Ehrlich–Schwoebel (*ES*) barrier.^{74, 76} The *ES* barrier, which is illustrated in Figure 3-8, is an additional barrier (ΔE_{ES}) that is added to the diffusion barrier (E_{diff}) as a result of bond stretching at the step when an adatom crosses the step edge to the lower terrace. It is therefore easier for Cu atoms at the step edge to reach the lower terrace while, because of the longer path to the edge, Cu atoms in the middle of the terrace may not have sufficient energy to overcome both ΔE_{ES} and E_{diff} , and so are reflected from the step edge to form a second layer.

As the Cu coverage increases above 0.6 ML, the spreading 2D clusters are found to exhibit a Cu (111)-like orientation, as indicated by the triangle in Figure 3-6. As the Cu coverage increases, the 2D clusters grow increasingly thicker and more three-dimensional without filling in the gaps between the 2D clusters, such that the

percentage of uncovered ZnO surface remains essentially unchanged. This implies that at this coverage, the 3D growth mode is dominant for Cu.

The growth of different metals on oxide surfaces has been studied and summarized in several review articles.^{112, 113} Growth modes similar to those described here were first observed by Ernst *et al.*^{4, 5, 114} for Cu particles that were vapor deposited on oxygen-terminated ZnO(0001) at 130 K. This study also found that the vapor deposited metal grew in the form of 2D clusters up to a certain critical coverage, beyond which 3D clusters formed. This type of growth mode was subsequently observed in other Cu/ZnO systems.¹¹⁵ However, because the temperatures of the ZnO surface are below 300 K in the current work, the growth mode and surface morphology are likely kinetically limited. Therefore, in the following sections, the kinetic effects are examined separately with respect to incident energy and the temperature of the ZnO surface.

3.3.3 Effect of Incident Energy

The incident energy of the Cu clusters is one of the parameters varied for the deposition process. A previous experimental study^{4, 92, 115-117} of Cu thin films grown on Cu(111) by direct ion deposition exhibited a strong morphological dependence on the incident energy. In an effort to probe this effect for Cu growth on ZnO, three different incident energies, 0.30, 1.25, and 2.81 eV/atom, are considered for Cu₆ up to a coverage of 1 ML while the surface temperature is maintained at 300 K. The resulting Cu thin films are illustrated in Figure 3-9.

At energies of 0.30 eV/atom, the Cu₆ octahedron clusters are predicted to spread out on the surface to form planar clusters or break into individual atoms without maintaining their original geometry. Because the incident energy is sufficient to overcome the migration barrier, adjacent Cu atoms or small clusters are able to merge

into larger clusters. This spreading and coalescence is predicted to be more prevalent at energies of 1.25 eV/atom, which leads to a larger percentage of the ZnO surface covered by 2D Cu clusters. As the incident energy is increased further to 2.81 eV/atom, the incident Cu clusters are predicted to penetrate into the surface and to partially mix with the surface Zn atoms as they rebound, thus forming Cu-Zn mixtures at or near the surface.

In an attempt to quantitatively analyze these modifications to the surface morphology, the surface roughness of the deposited film is investigated by the approach of root-mean-square (RMS) method. The definition of RMS can be expressed as,

$$R_q = \sqrt{\frac{\sum_i^n (Z_i - \bar{Z})^2}{n}} \quad (3-2)$$

where Z_i represents the height of the deposited atoms on the surface, \bar{Z} denotes the mean height of all the deposited atoms, and n is the total number of deposited atoms. The surface roughness based on RMS is 1.48, 1.33, and 1.42 for 0.30, 1.25 and 2.81 eV/atom, respectively. This finding indicates that the surface morphology becomes smoother as the incident energy increases up to a certain point. However, at energies beyond this point, the surface atoms will be sputtered and the surface roughness will increase.

3.3.4 Effect of Surface Temperature

In addition to the incident energy, the surface temperature is another deposition condition that can be varied. We considered the deposition of 1ML of Cu with an incident energy of 1.25 eV/atom on surfaces maintained at temperatures of 300, 600 and 800 K. As shown in Figure 3-10, although these predicted surface morphologies

finally exhibit 3D Cu cluster formation, small and random 3D clusters are found when the surface temperature is maintained at 800 K. Based on our simulation results, the area of 2D Cu clusters in terms of the number of Cu atom in the first layer increases with increasing surface temperature. It is estimated that the area of 2D Cu clusters increases around 12 % when the surface temperature is 800 K relative to when it is 300 K. Additionally, the structures of the 2D Cu clusters are more compact and exhibit the well-defined, Cu (111) structure at 800 K relative to their structures at 300 K. This relative dependence of surface temperature and Cu cluster morphology can be attributed to the fact that the thermal annealing effect provides additional energy for the migration of the Cu adatoms. However, because the thermal energy (0.08 eV at 800 K) is relatively small compared to the migration barrier (0.7 eV), the effect of surface temperature on the resulting surface morphology is not as significant as the effect of incident energy.

3.4 Comparison of the Growth of Cu on Cu(111) and ZnO(10 $\bar{1}$ 0)

It is expected that the surface structure of the substrate will influence the behavior of the deposited Cu clusters. To fully explore this effect on Cu thin film growth, the parameters used for 2ML Cu deposition on the ZnO(10 $\bar{1}$ 0) surface are applied to Cu deposition on the Cu(111) flat surface. Figure 3-11 and 3-12 illustrates the evolutions of surface morphologies on both surfaces.

Based on our previous study,³⁸ COMB predicts that the two lowest migration barriers for hopping and exchange mechanisms of a Cu adatom on Cu(100) are 0.42 and 0.53 eV, respectively. Because Cu (111) is a close-packed surface, the migration barrier for a Cu adatom on the (111) surface is lower than on the (100) surface. Thus,

as expected, our simulation results predict that deposited Cu atoms are able to easily migrate on the Cu(111) surface through hopping and exchange mechanisms which leads to the formation of laminar thin films with low surface roughness, as shown in Figure 3-13 (A). The result is in excellent agreement with experimental findings.¹⁰⁶ In contrast, as shown in Figure 3-13(B), deposited Cu clusters are predicted to form larger 3D clusters accompanied by spreading 2D clusters on ZnO(10 $\bar{1}$ 0) that exhibit a hexagonal shape with the Cu(111) orientation. The growth of Cu on ZnO can also be predicted using COMB by calculating the free energies of Cu and ZnO surfaces and the interfacial energy of Cu/ZnO, which are difficult to measure experimentally. In particular, three-dimensional film growth is expected when $\gamma_{\text{Cu}} + \gamma_{\text{ZnO}} < \gamma_{\text{Cu/ZnO}}$, and the two-dimensional film growth is expected when $\gamma_{\text{Cu}} + \gamma_{\text{ZnO}} > \gamma_{\text{Cu/ZnO}}$, where γ_{Cu} , γ_{ZnO} are the free surface energies of Cu and ZnO, respectively, and $\gamma_{\text{Cu/ZnO}}$ is the interfacial energy of Cu/ZnO.

In addition, based on the charge analysis predicted by COMB, Cu atoms are predicted to have a positive partial charge ($q_{\text{avg}} = +0.28e$) when they were deposited on ZnO but a near-neutral charge ($q_{\text{avg}} = +0.07e$) when deposited on the Cu surface. This finding indicates that the properties of the initial deposited Cu atoms are highly dependent on the nature of the surface.

3.5 Summary

The classical MD simulation results reported here make use of a new, third-generation COMB potential for ZnO. They predict that two-dimensional (2D) clusters of Cu form on ZnO(10 $\bar{1}$ 0) following the initial deposition of Cu₆ with incident energies of 1.25 eV/atom until the coverage of Cu is above 0.4 ML. With increasing coverage, the

2D Cu clusters spread to cover more of the clean ZnO surface. However three-dimensional (3D) cluster formation is also predicted. In particular, beyond a certain coverage, the transformation of 2D clusters into 3D clusters occurs more quickly than the spreading of 2D clusters to fill in the gaps between them. This implies that 3D growth is dominant at higher Cu coverage. The results thus elucidate the ways in which Cu growth transitions from layer-by-layer to three-dimensional as the coverage increases. The simulations also consider the kinetic effects on Cu clusters and thin-films growth in terms of incident energy and ZnO surface temperature. The simulations predict that incident energy is a critical factor for controlling the final structure of the thin film, while Cu-Zn surface mixing may result at high incident energies. On the other hand, although increasing the surface temperature does not show a significant influence on surface morphology as the effect of incident energy did, small and random 3D clusters with compact 2D clusters are found when the surface temperature is maintained at 800 K. Finally, we compare Cu growth on different supports of Cu (111) and ZnO(10 $\bar{1}$ 0). The simulations clearly indicate that deposited Cu clusters form laminar thin films on Cu (111) and clusters on ZnO(10 $\bar{1}$ 0). In addition, the charge on the Cu atoms is highly dependent on the nature of supporting surfaces. Specifically, Cu atoms have partial positive charges when they are deposited on ZnO but near neutral charges when deposited on the Cu surface. These results are expected to guide the interpretation of experimental data and optimization of supported metal systems for future catalyst design.

Table 3-1. Comparison of the properties of ZnO wurtzite phase predicted by the COMB2 and COMB3 potentials with values obtained from experiments and DFT calculations.

Properties	Exp.	DFT	COMB2	COMB3
a_0 (Å)	3.242	3.292	3.249	3.267
c_0 (Å)	5.187	5.293	5.213	5.189
c/a	1.600	1.608	1.604	1.582
E_c (eV/ZnO)	-7.520	-7.692	-7.440	-7.524
B (GPa)	136	134	147	138
C_{11} (GPa)	207	230	252	206
C_{12} (GPa)	121	82	129	114
C_{13} (GPa)	106	64	98	97
C_{33} (GPa)	210	247	267	217
C_{44} (GPa)	43	75	37	44
C_{66} (GPa)	–	74	57	47
$\gamma_{\text{Cleave}}(10\bar{1}0)$ (J/m ²)		2.30	2.12	2.21
$\gamma_{\text{Cleave}}(11\bar{2}0)$ (J/m ²)		2.50	2.31	2.33
$\gamma_{\text{Cleave}}(0001)/(000\bar{1})$ (J/m ²)		4.30	2.02	2.61
$\Delta E(\text{ZnS-Wurtzite})(\text{eV/ZnO})$		0.013	0.008	0.021
$\Delta E(\text{NaCl-Wurtzite})(\text{eV/ZnO})$		0.237	0.217	0.903
$\Delta E(\text{CsCl-Wurtzite})(\text{eV/ZnO})$		1.358	0.958	1.225

Table 3-2. Properties of Cu-Zn alloys predicted by COMB3 compared to those from experiments and DFT calculations. The reference states for the enthalpies of formation and metallic fcc Cu and hcp Zn, which are -3.725 and -1.272 eV/atom, respectively.

Phases	Properties	Exp.	DFT ⁺	COMB3
γ -Cu ₅ Zn ₈	a_0 (Å)	8.86 ¹⁰⁵	8.88	8.88
	ΔH_f (kJ/mol)		-126	-138
	B (GPa)	123 ¹⁰⁵		156
β -CuZn	a_0 (Å)		3.34	3.36
	ΔH_f (kJ/mol)		-21	-48
α -Cu ₃ Zn	a_0 (Å)		2.97	3.01
	ΔH_f (kJ/mol)		-16	-36

⁺ Our DFT calculations

Table 3-3. The adsorption energy (eV) of a single Cu adatom at the three different adsorption sites on the ZnO(10 $\bar{1}0$) surface illustrated in Figure 2 as predicted by COMB3 and DFT.¹⁰⁷

E_{ads} (eV)	Site 1	Site 2	Site 3
DFT	1.52 (0.32 e)	1.96 (0.55 e)	1.65 (0.40 e)
COMB3	1.30 (0.55 e)	1.76 (0.63 e)	1.47 (0.61 e)

Table 3-4. Predicted migration barriers of a Cu adatom on the ZnO(10 $\bar{1}0$) surface found using the dimer method with COMB3 and compared with DFT results.¹⁰⁷

Sites(initial \rightarrow final)	2 \rightarrow 3	2 \rightarrow 1
$E_{barrier}$ (eV)		
DFT	0.40	0.30
COMB3	0.76	0.68

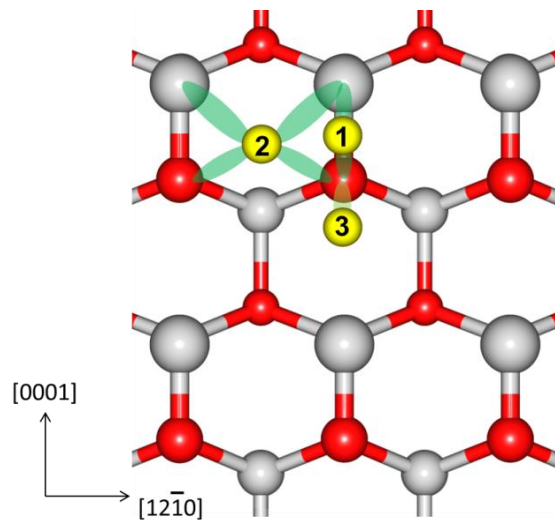


Figure 3-1. Top view of three different adsorption sites of Cu atoms on the ZnO($10\bar{1}0$) surface. The Zn (grey) and O (red) are distinguished by color and the atoms in the first (large) and the second (small) layers are distinguished by size. The numbered yellow spheres represent the possible adsorption sites for the Cu adatoms.

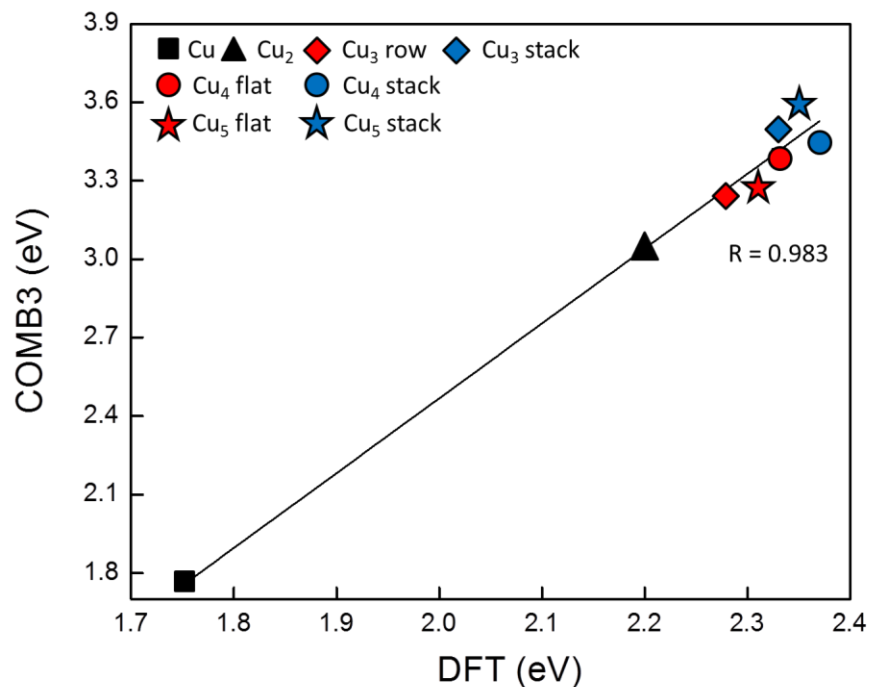
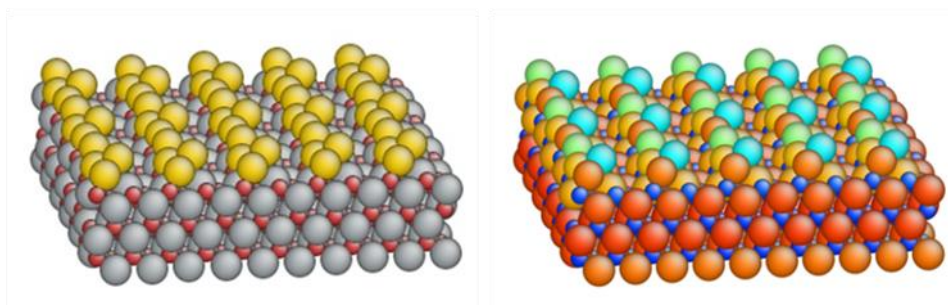
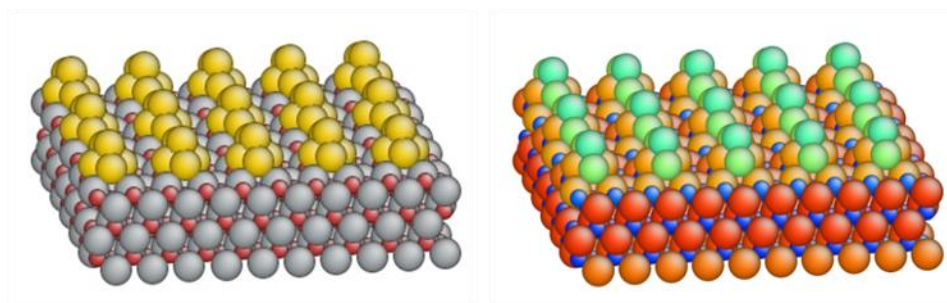


Figure 3-2. The binding energy (eV) of Cu_n ($n = 2$ to 5) clusters on ZnO($10\bar{1}0$) predicted by DFT calculations and COMB potential. The trendline and R-squared value (0.983) are given in the figure.

A



B



-1.0 -0.5 0 0.5 1.0



(e)

Figure 3-3. Relaxed structure of Cu_5 clusters supported by the $\text{ZnO}(10\bar{1}0)$ surface. A) Flat. B) Stack. (At left) Yellow atoms are Cu, red atoms are O, and grey atoms are Zn). (At right) Atoms are color coded by the charges with the color indicating the charge values.

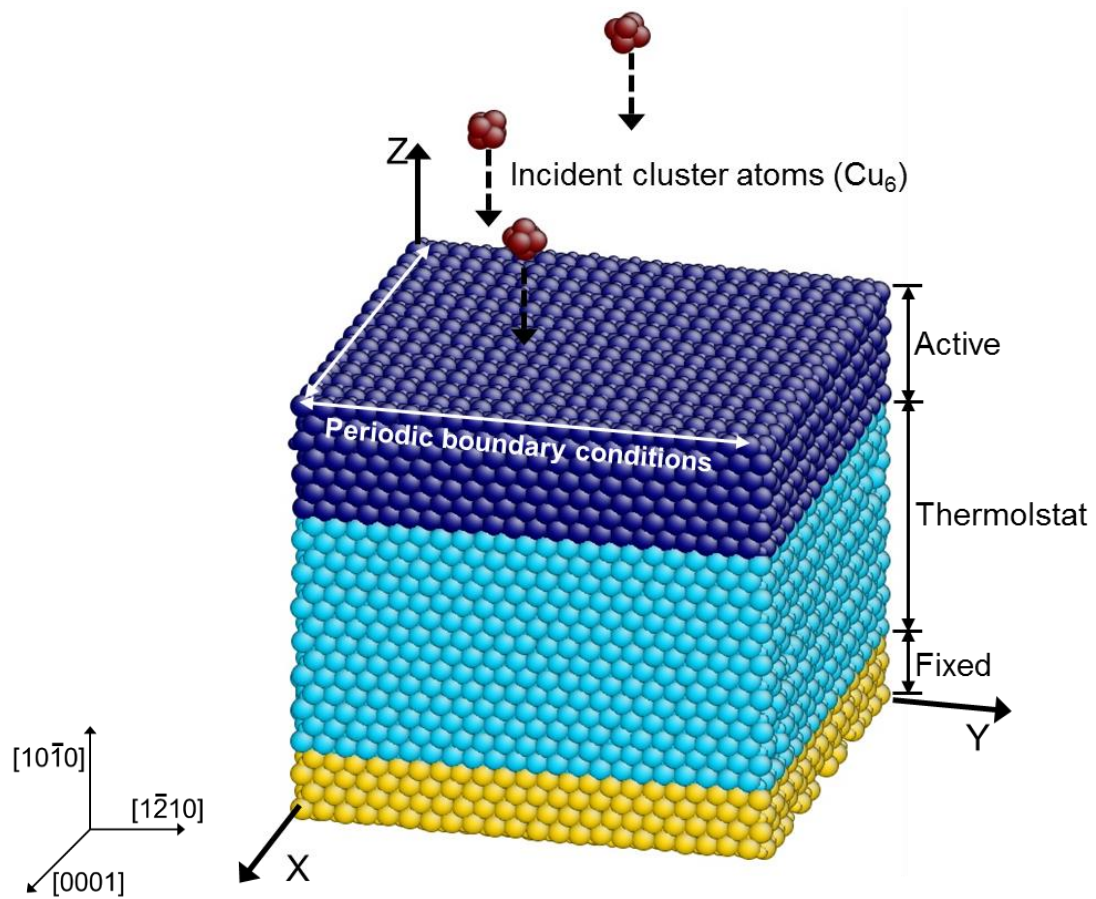


Figure 3-4. Simulation model for deposition of Cu clusters on the ZnO(10 $\bar{1}0$) surface.

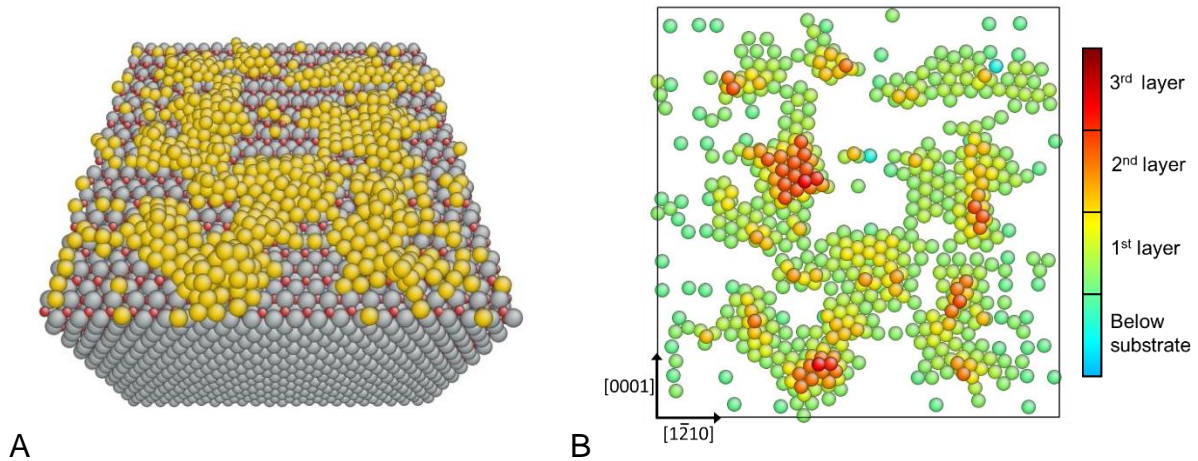


Figure 3-5. MD simulation of the morphology of Cu clusters following the deposition of 1ML of Cu atoms. A) The Cu, O, and Zn atoms are represented by yellow, red, and grey spheres, respectively. B) Top-down snapshot of just the Cu atoms, which are color coded by height according to the scale shown.

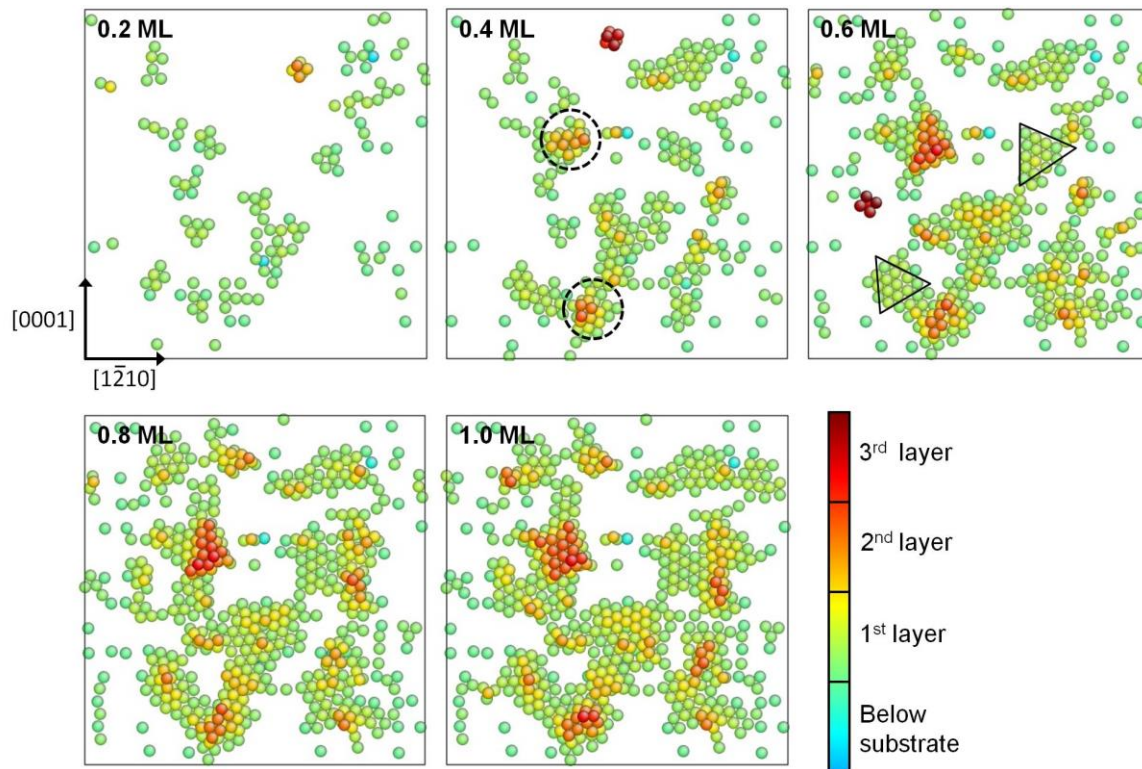
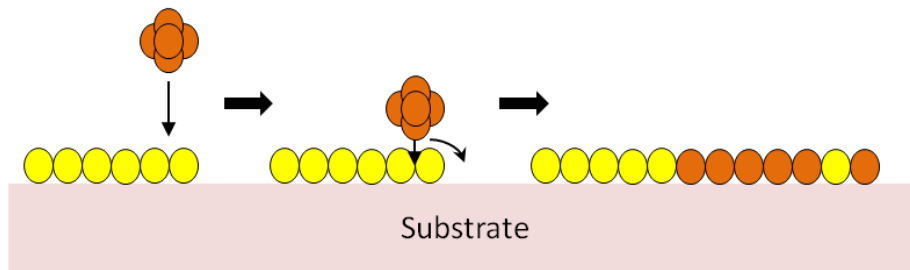


Figure 3-6. Snapshots of just the Cu atoms at the indicated coverage (0.2–1ML) following deposition on ZnO(10 $\bar{1}$ 0). The Cu atoms are color coded by height according to the scale shown.

A



B

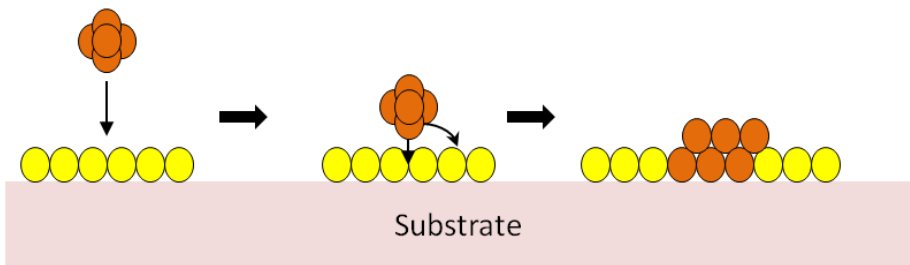


Figure 3-7. The deposition processes of Cu clusters landing on ZnO surface. A) The deposited Cu cluster lands on the edge of an existing 2D cluster and Cu atoms step down to the lower terrace. B) The deposited Cu cluster lands around the center of an existing 2D cluster and starts to form the second layer.

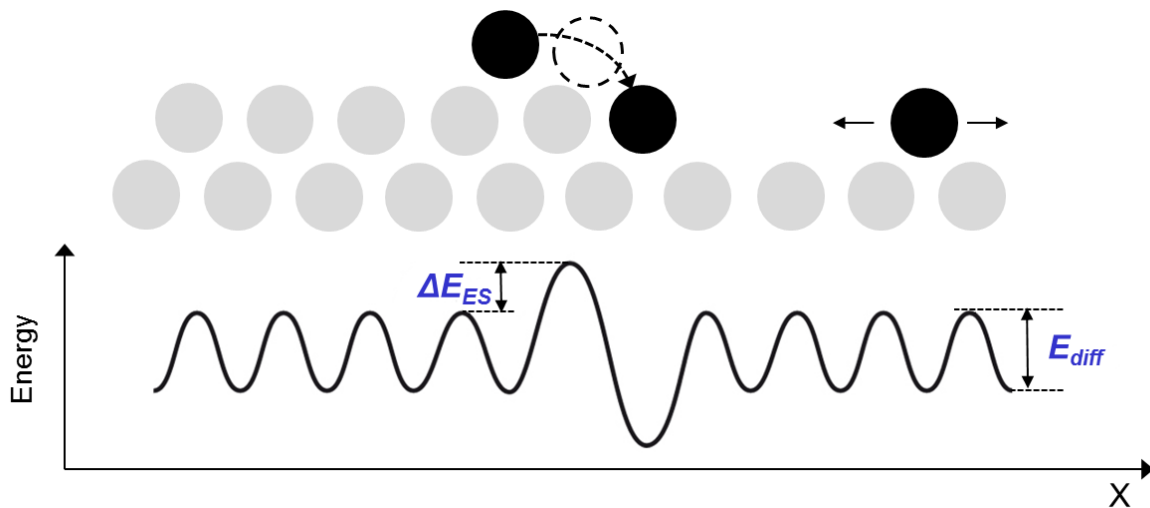


Figure 3-8. Schematic of Ehrlich–Schwoebel barrier (ΔE_{ES}) for an adatom on the step edge to descend to the lower terrace in addition to the diffusion barrier (E_{diff}).

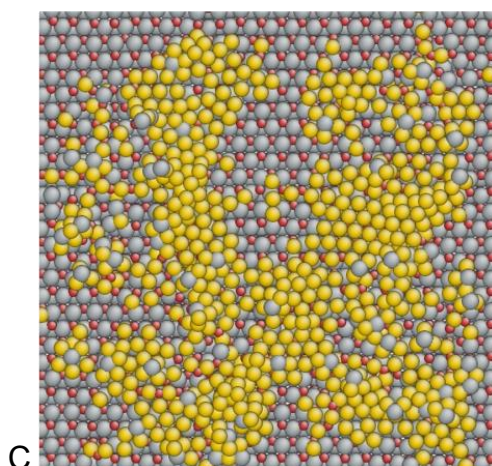
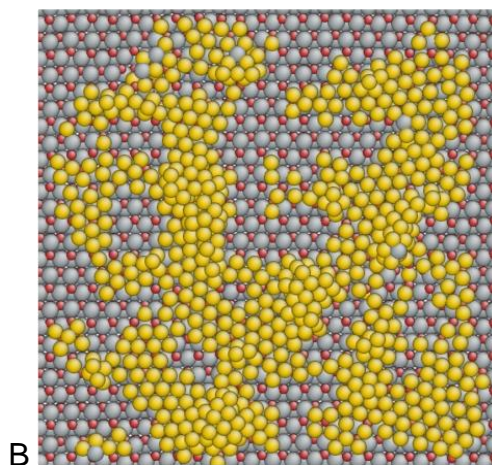
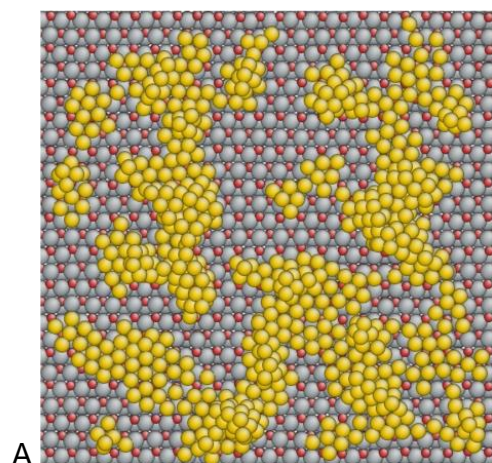


Figure 3-9. Top-down snapshots from MD simulation of the surface morphology of 1ML of Cu deposited on ZnO($10\bar{1}0$) with different incident energies. A) 0.30, B) 1.25, and C) 2.80 eV/atom.

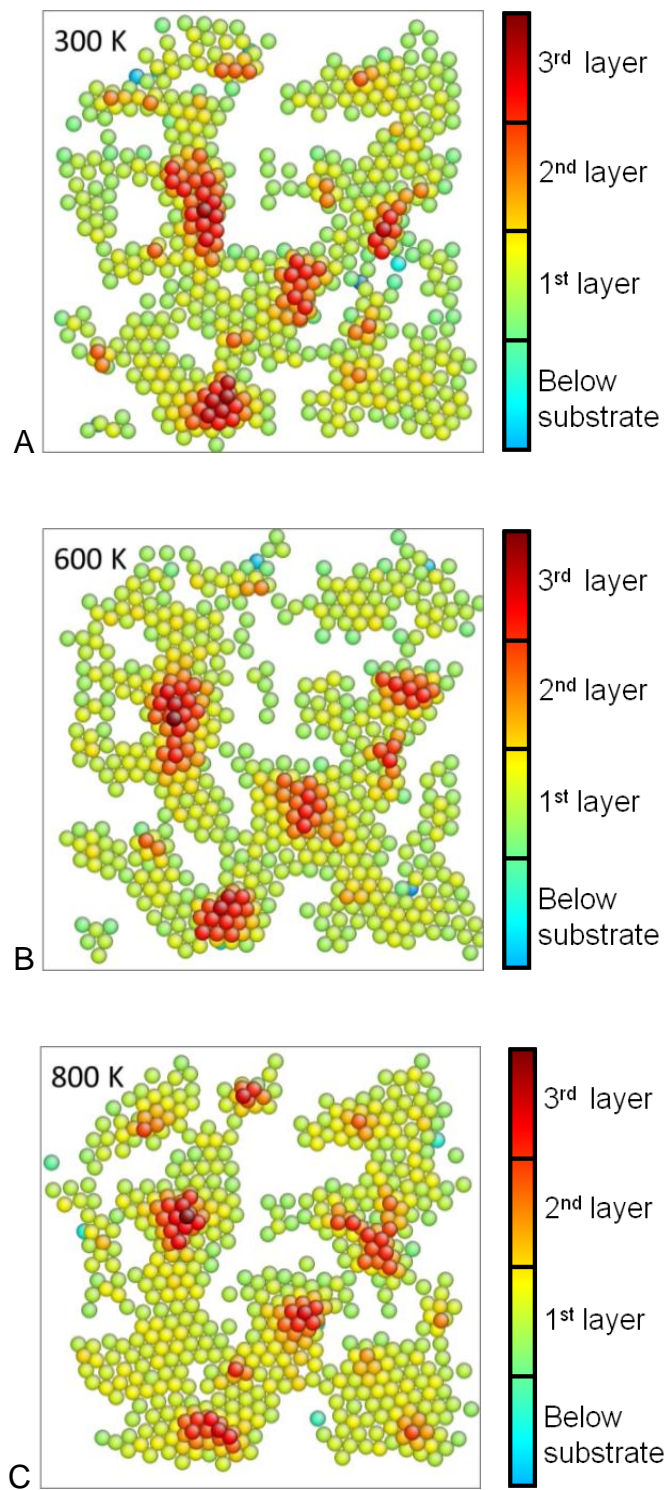


Figure 3-10. Top-down snapshots from MD simulation of the morphology of 1ML Cu deposited on ZnO($10\bar{1}0$) maintained at the indicated temperatures. A) 300 K, B) 600 K, C) 800 K. The Cu atoms are color coded by height according to the scale shown.

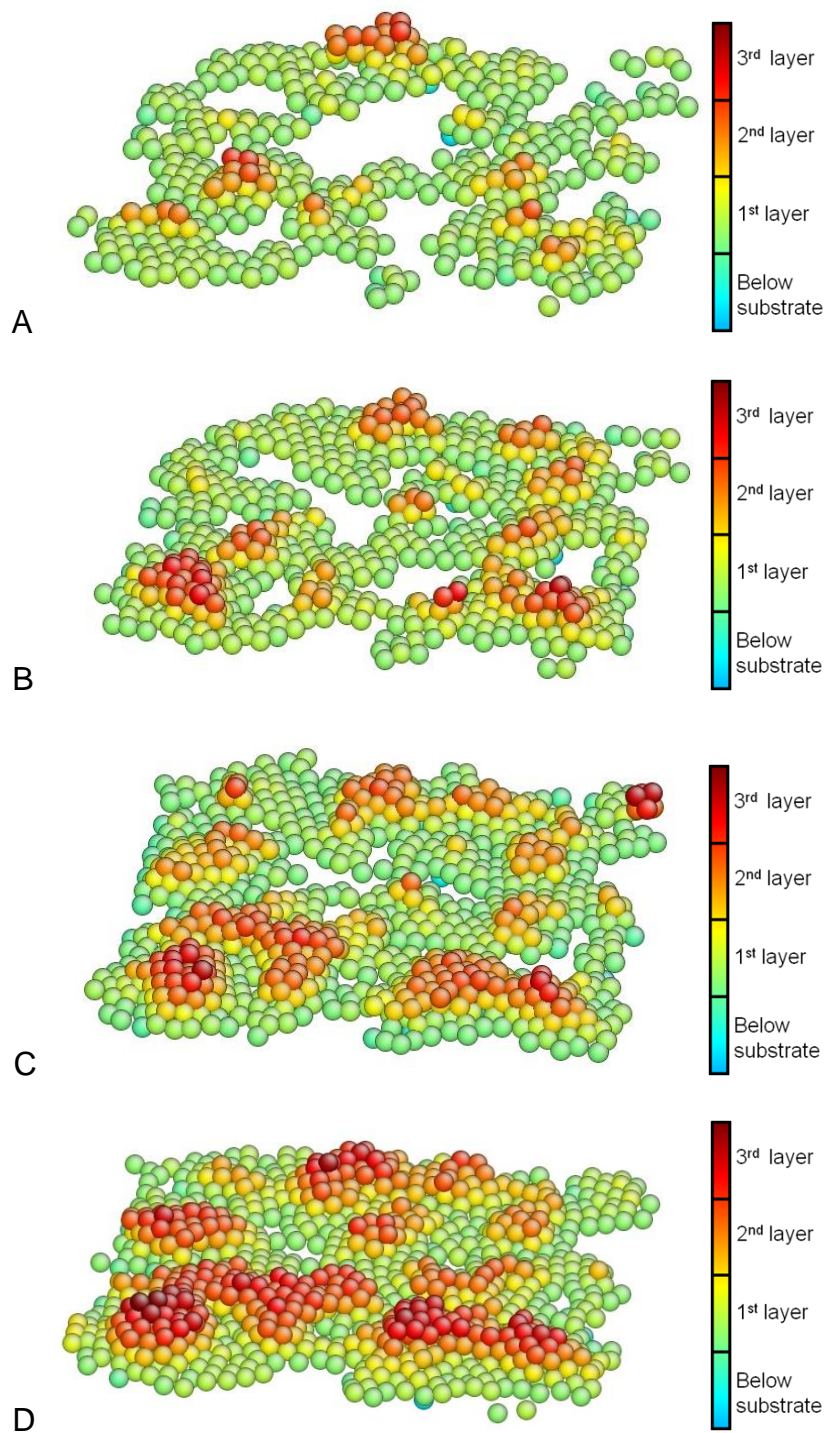


Figure 3-11. Snapshot from an MD simulation of the morphology of Cu clusters on ZnO(10 $\bar{1}0$) at the indicated coverage. A) 0.5 ML, B) 1.0 ML, C) 1.5 ML, D) 2.0 ML. The Cu atoms are color coded by height according to the scale shown.

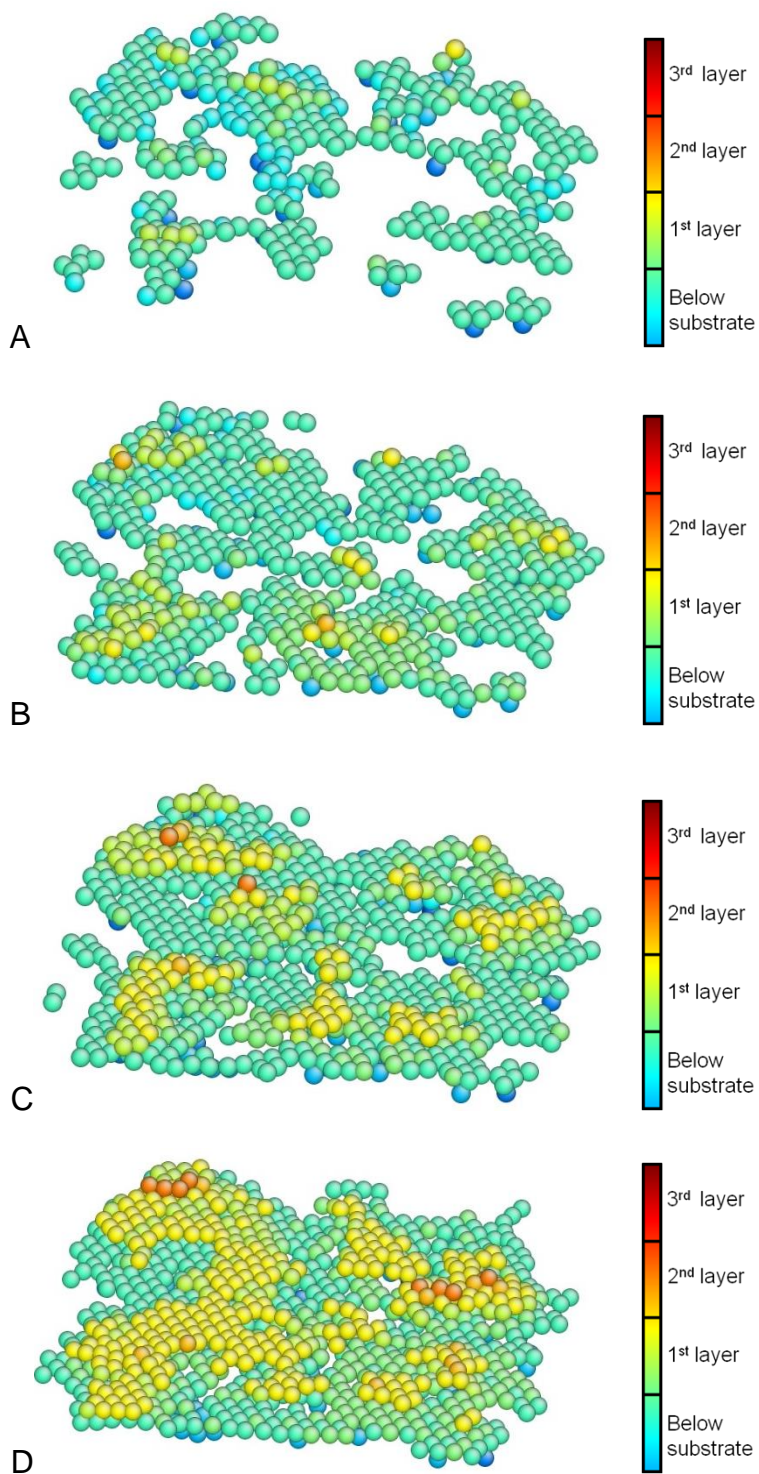
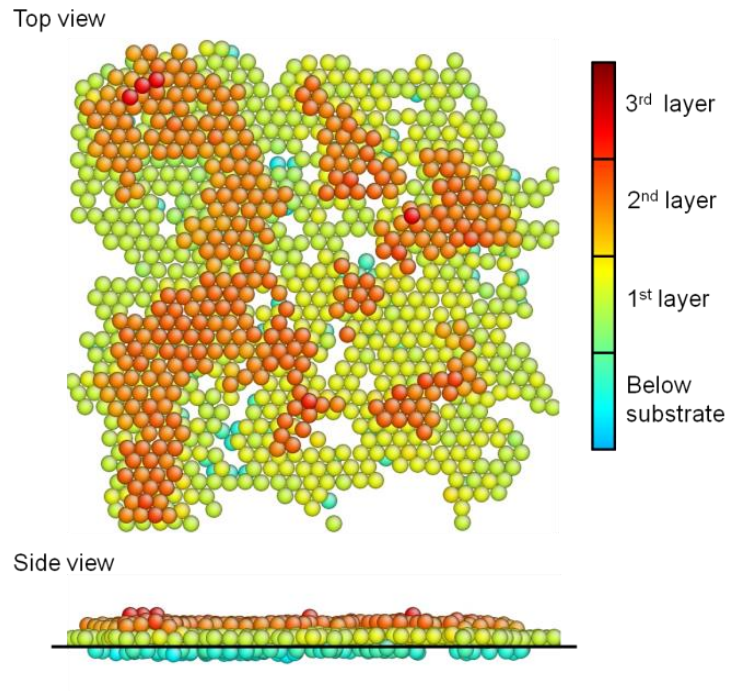


Figure 3-12. Snapshot from an MD simulation of the morphology of Cu clusters on Cu(111) at the indicated coverage. A) 0.5 ML, B) 1.0 ML, C) 1.5 ML, D) 2.0 ML. The Cu atoms are color coded by height according to the scale shown.

A



B

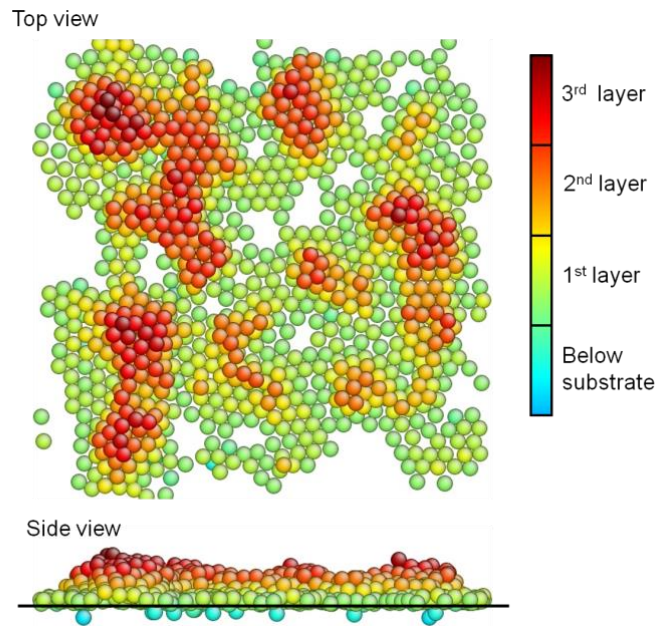


Figure 3-13. Top-down snapshots from the MD simulations of 2ML Cu deposited on Cu(111) and ZnO(10 $\bar{1}0$). A) Cu(111), B) ZnO(10 $\bar{1}0$). The Cu atoms are color coded by height according to the scale shown.

CHAPTER 4 DEVELOPMENT OF COMB3 TI/TIO₂ POTENTIAL AND ITS APPLICATIONS ON CU CLUSTERS ON TIO₂(110) SURFACES

Titania (TiO₂) has attracted much attention due to its diverse applications in pigments, gas sensors, solar cells, photo catalysts and heterogeneous catalysts.¹¹⁸ It is well known to crystallize into three natural polymorphs: rutile, anatase and brookite. In addition to these naturally occurring phases, several high pressure phases of titania have been found experimentally or suggested by theoretical calculations,¹¹⁹ including columbite (α -PbO₂), cotunnite (PbCl₂), baddeleyite (ZrO₂), fluorite (CaF₂), pyrite (FeS₂), hollandite (MnO₂), and ramsdellite (MnO₂).

Several empirical, fixed charge rigid ion potentials have been developed for atomistic and molecular dynamics simulations of TiO₂ systems^{120, 121} The formal charge model by Collins *et al.*¹²⁰ and the partial charge model by Matsui *et al.*¹²² describe the relative phase stabilities of titania polymorphs and low Miller index rutile surfaces quite well.¹¹⁹ Following the theories of Sanderson,¹²³ Parr *et al.*¹²⁴ and Mortier *et al.*¹²⁵ for charge equilibration (QEq), Rappé and Goddard introduced the screening the Coulomb interactions that turned the Hessian positive definite for most systems at regular densities.¹²⁶ Some of empirical potentials adopting this QEq scheme have also been developed for TiO₂, including the Morse stretch (MS-Q)¹¹⁹ potential, the second-moment Buckingham (SMB-Q)¹²⁷ potential and the second-moment tight-binding (SMTB-Q)¹²⁸ potential. Most recently, a ReaxFF Ti/TiO₂ potential has been developed for describing chemical reactions in Ti/O/Cl/H systems.^{129, 130}

In this work, the third-generation COMB potential is parameterized for titanium metal and titania and used in classical molecular dynamics (MD) simulations in combination with a previously parameterized potential for Cu to investigate the

properties of copper clusters on $\text{TiO}_2(110)$. The rest of the section is organized as follows. In section 4-1, we introduce the COMB potential functions for the Ti and TiO_2 systems, including the fitting procedure, properties of the bulk polymorphs, and relative stability of Ti and TiO_2 rutile surfaces. In section 4-2, we demonstrate the transferability of the COMB potential by applying it to the Cu/ TiO_2 system. In particular, the adsorption behavior of Cu clusters of different sizes on perfect, reduced and oxidized $\text{TiO}_2(110)$ surfaces are investigated in classical MD simulations. The findings are compared to the results of density functional theory (DFT) calculations and published experimental results. Lastly, in section 4-3 we summarize the major conclusions of this work.

4.1 Potential Development and Properties of Ti and TiO_2

4.1.1 Fitting Procedure

We apply an algorithm that fits structural and energetic information for multiple phases for the system of interest. The procedure determines the potential parameter set using a least-squares method to minimize a penalty function, $f(p)$, for each trial parameter set p . The penalty function is determined for all included phases by calculating the variation of lattice parameters, elastic constants, and phase stability with corresponding weighting factors. Here, the hexagonal closed packed (*hcp*) and rutile structures are the main focus phase for the Ti and TiO_2 systems, respectively. Therefore, the largest weighting factors are assigned to the properties of these two phases.

Wherever possible we use first-principles data from the literature, and when this is not available we perform our own DFT calculations to complete the data set for fitting and comparison. Our first-principles calculations are carried out with the Vienna *ab initio* Program (VASP)⁵⁹⁻⁶² program using the generalized-gradient approximation (GGA)¹³¹

and the Perdew–Burke–Ernzerhof (PBE)⁴³ exchange–correlation functional. The calculations utilize plane-wave basis sets with a 500 eV energy cutoff, a 4x4x4 Monkhorst-Pack k-point mesh,¹³² and projector augmented-wave (PAW) pseudopotentials^{133, 134} for Ti ([Ne] core with 3s²3p⁶4s²3d² electrons) and O ([He] core with 2s²2p⁴ electrons). The convergence criteria are set at 1.0×10^{-5} eV and 1.0×10^{-3} eV·Å⁻¹ for energies and forces, respectively.

The procedure used for parameter fitting follows that outlined by Liang *et al.*¹³⁵ In particular, element-type parameters are fit for pure elements (Ti and O) and bond-type parameters are fit for TiO₂ systems. The fitting structures for metallic Ti include the *hcp*, face-centered cubic (*fcc*), body-centered cubic (*bcc*), simple cubic, and diamond phases. The element-type parameters of oxygen, which are kept the same throughout the third-generation of COMB to ensure full compatibility and transferability of the different potentials, are fit to dimer and trimer oxygen molecules.

For TiO₂ binary systems, we include 10 different AB₂ phases in the fitting training set, following the work of Swamy *et al.*¹¹⁹ These include rutile (space group: *P4₂/mnm*), anatase (*I4₁/amd*), and brookite (*Pbca*), in addition to the high pressure phases columbite (*Pbcn*), cotunnite (*Pnma*), baddeleyite (*P2₁/c*), and fluorite (*Fm-3m*) and the hypothetical phases of pyrite (*Pa-3m*), hollandite (*I4/m*), and ramsdellite (*Pbnm*). The atomic and electrostatic parameters for Ti and O while the bond-dependent parameters for Ti-O and O-Ti are provided in A-1, A-2, and A-4.

4.1.2 Predicted Ti Properties

The static properties of metallic Ti are reported in this section, where the structures are geometrically optimized until the deviation of total energy and force on

each atom are smaller than $1 \times 10^{-5} \text{ eV}$ and $1 \times 10^{-2} \text{ eV/\AA}$, respectively. Table 4-1 compares the physical properties of the *hcp* phase of Ti predicted by COMB with values from published experimental data, DFT calculations, and a modified embedded atom method (MEAM) potential. The properties marked with an asterisk denote fitted properties, while all others are predicted properties.

The COMB potential successfully reproduces the phase stability of Ti, with *hcp* the ground state phase, and *fcc* and *bcc* having higher energies. The fitted energy differences between *fcc-hcp* and *bcc-hcp* are 65 meV/atom and 100 meV/atom, respectively, which are in a good agreement with the DFT values. The lattice parameters of *hcp* Ti metal fitted by COMB deviate from the experimental values by -0.5% and +1.1% for a_0 and c_0 , respectively. These deviations result in a larger value of c/a ratio=1.61, which is larger than the experimental value of 1.587. Most importantly, both are significantly lower than the ideal value of $c/a=1.633$; it can thus be expected to reproduce the experimentally observed deformation mechanisms.^{136, 137} The cohesive energy and elastic constants fitted by COMB reasonably well reproduce the experimental and DFT values.

The vacancy and interstitial defect formation energy are qualitatively reproduced by COMB, although the Ti interstitial (octahedral site) formation energy is overestimated. The result indicates that the formation energy for a Ti vacancy is 2 eV smaller than the energy to form a Ti interstitial. Finally, the predictions for surface energies of the three low Miller index surfaces are given in Table III. The COMB potential predicts that the (0001) basal plane has a lower surface energy than the surfaces on the $(1\bar{1}00)$ and $(2\bar{1}\bar{1}0)$ planes. This trend is also predicted by the MEAM

potential. However, these predicted trends do not agree with the results of the DFT calculations, which predict the $(2\bar{1}\bar{1}0)$ prismatic surface to be the most stable Ti surface. The average predicted surface energies from the COMB potential are ~25% smaller than the average value measured experimentally.

4.1.3 Properties of Rutile TiO₂ and Phase Stability

The properties of rutile TiO₂ from the COMB potential, compared to the experimental values, DFT calculations, and three other classical interatomic potentials (Matsui¹²², MS-Q¹¹⁹, SMB-Q¹²⁷, and ReaxFF¹²⁹) are presented in Table IV. The Matsui and MS-Q values are generated with the General Utility Lattice Program (GULP)^{138, 139} using parameters provided in Refs ¹¹⁹ and ¹²², respectively.

For the rutile phase, the COMB potential fits the lattice parameters and cohesive energy in a good agreement with experimental values, where the deviations are all below 1%. With regard to the elastic constants, although the larger overestimation of C₁₂ leads to a larger bulk modulus reproduced by COMB, the reproduced elastic constants of C₁₁, C₃₃, C₁₃, C₃₃, C₄₄, and C₆₆ are within 20% of the experimental and DFT values. One thing to note is that the violation of the Cauchy relation is observed experimentally.^{140, 141} The Cauchy relation states that C_{ijkl}=C_{ikjl}, so that, for example, C₁₂ is equal to C₄₄ for cubic systems and C₁₂ is equal to C₆₆ for tetragonal systems such as rutile. To faithfully reproduce the elastic moduli of TiO₂, COMB should capture this violation so that C₁₂≠C₆₆ for TiO₂, which as indicated in Table 4-2, it does reasonably well.

Table 4-3 lists the energy differences between the rutile and other AB₂ phases predicted by COMB, DFT and other empirical potentials. Both the COMB and Matsui

potentials predict the rutile phase to be the most stable, followed by columbite, brookite and anatase. The MS-Q and SMB-Q potentials also predict rutile to be the ground state phase, but followed by brookite and anatase, respectively. Although the COMB potential does not predict exactly the same phase order for all other AB_2 phases relative to DFT, rutile is correctly predicted to be more stable than the high pressure or hypothetical AB_2 phases. This structural stability is important when the properties of rutile phases are determined at high temperatures which may lead to phase transformations.

4.1.4. TiO_2 Low Miller Index Surfaces

Single-crystalline TiO_2 surfaces are important in a wide range of applications.¹¹⁸ An important aspect of assessing the quality of a TiO_2 empirical potential is its ability to describe surface properties. We therefore investigate the capability of the developed COMB TiO_2 potential by calculating the surface energies of pristine TiO_2 rutile low Miller Index surfaces. Since experimental numbers for these surface energies are difficult to obtain, we largely compare values predicted from COMB to the results of DFT and other empirical potentials.

Table 4-4 compares the energies of the (110), (100), and (001) surfaces of rutile predicted by the COMB potential, DFT^{142, 143} and other empirical potentials^{119, 122, 127, 144, 145}. The relaxed (unrelaxed) surface energies predicted by COMB for (110), (100), and (001) are 0.99 (1.09), 1.25 (1.76), and 1.49 (1.87) J/m^2 , respectively. The surface energies computed with first principles techniques over the last fifteen years are reported by Hallil *et al.*¹⁴⁵ Because different approaches (linear combinations of atomic orbitals, plane waves), software packages, and number of surface slab layers are used in the calculations, the (110) surface energies range from 0.40 to 1.10 J/m^2 . Nevertheless, this low Miller index orientation is predicted to be the most stable surface

by all methods considered, followed by the (100) and (001) orientations for the TiO₂ rutile phase.

Variable charged empirical potentials such as COMB, SMB-Q,¹²⁷ and SMTB-Q¹⁴⁵ predict the correct order of surface stability, where SMTB-Q does a better job in predicting the value of surface energies relative to DFT. Kim et al.¹²⁹ reported the surface energies for five different surfaces (three for the anatase phase and two for rutile) using ReaxFF, which predicts that (110) is more stable than (101) surfaces in the case of rutile. In contrast to predictions from the above potentials, the MS-Q potential predicts an incorrect order for the (110) and (100) surface energies.

In addition to the surface energy, it is important that the property of surface atoms, such as charge transfer, is properly captured as they influence processes such as catalysis and thin-film growth. The charge transfer defined here is the charge variation between the atomic charge of a surface atom and its charge in the bulk. The reference bulk charges for Ti and O in COMB are +1.905 and -0.953, respectively. The surface atoms selected for charge transfer determination on (110), (100), and (001) surfaces are labeled in Figure 4-1.

Table 4-5 presents the charge transfer determined by the COMB potential compared with the published results of Mulliken charges from DFT calculations with the CRYSTAL06 code.¹⁴⁵ For the (110) and (100) surfaces, the predictions of COMB are in a good agreement with the results of DFT, particularly for the sign of charge transfer. Both show only bridge oxygen atoms O₍₁₎ becoming more positively charged with respect to the bulk, although the charge transfer on O₍₁₎ of TiO₂(110) is overestimated by COMB. In the case of the (001) surface, charge transfer also takes place primarily on

the most undercoordinated surface atoms, $Ti_{(1)}$ and $O_{(1)}$. In particular, COMB predicts that the four-fold coordinated $Ti_{(1)}$ atom become more negatively charged with respect to the bulk (six-fold) and other five-fold Ti surface atoms of the (110) and (100) surfaces, which is consistent with the results of DFT calculations. This result demonstrates that COMB is capable of describing correctly the charge of atoms under different environments, which is an important criterion for the modeling heterogeneous catalysis.

4.2 Heterogeneous Interfacial System: $Cu_n/TiO_2(110)$

4.2.1 Cu Clusters on Stoichiometric $TiO_2(110)$

Understanding the growth mode of metals on oxide surfaces is important for the design of electronic devices, catalysts, and sensors.¹⁴⁶ The main strength of the COMB potential is its transferability that allows the combination of established potentials for modeling heterogeneous systems, such as metal/metal-oxide systems. In this section, we consider the energetics of Cu clusters supported by rutile $TiO_2(110)$, which is of particular interest for heterogeneous catalysis.¹⁴⁷ To characterize the relative stability of different sized copper clusters, the binding energy (E_b) per atom is estimated using the following standard equation:

$$E_b = (1/n) [E(Cu_n) + E(TiO_2) - E(Cu_n/TiO_2)], \quad (4-1)$$

where n is the number of Cu atoms, $E(Cu_n/TiO_2)$ is the total energy of Cu_n adsorbed on the surface, and $E(Cu_n)$ and $E(TiO_2)$ are the energies of the Cu_n clusters and the optimized TiO_2 surface slab, respectively.

The preferred adsorption site and energetics for single Cu atoms on this surface was investigated first. A Cu atom was placed above the bridging O atom (labeled $O_{(1)}$ in Fig. 4-1), the five-fold coordinated Ti atom (labeled $O_{(1)}$ in Fig. 4-1), and in-between two

bridging O atoms. The COMB potential predicts the Cu binding energies on these sites to be 2.32, 0.15, and 3.25 eV, respectively. Thus, COMB predicts that the most favorable adsorption site for Cu is in between two bridging O atoms, which is also predicted by Giordano *et al.*¹⁴⁸ and Pillay *et al.*¹⁴⁹ using DFT calculations and observed by experiments.¹⁵⁰ This agreement gives confidence regarding the interaction of Cu clusters with this TiO₂ surface, something that is more computationally intensive to investigate using first-principles methods.

The configurations of the Cu clusters considered are illustrated in Figure 4-2. Cu₁₃, Cu₅₅, and Cu₁₄₇ are constructed with a cubo-octahedron shape, while Cu₃₈ is constructed with a truncated octahedron shape. Based on the binding energy, Cu₁₄₇ interacts most strongly with the surface than the other clusters considered. This higher binding energy is thought to result from the formation of more Cu-O bonds across the Cu cluster/TiO₂ interface. The charge distributions of the different sized Cu clusters are illustrated in Figure 4-3. Charge transfer is predicted to occur between the clusters and TiO₂ surface by the COMB potential that results in positively charged Cu clusters in agreement with DFT calculations.¹⁴⁸ The average charge of Cu₁₃, Cu₅₅, and Cu₁₄₇ clusters predicted by COMB are 0.33, 0.21, 0.20, and 0.15 $|e|$, respectively.

4.2.2 Cu₁₄₇ Clusters on Non-Stoichiometric TiO₂(110)

Previous experimental and theoretical studies have reported that the growth modes and optimal size of metal clusters deposited on TiO₂ depends on the details of the surface structure.¹⁵¹⁻¹⁵⁴ To quantify the influence of surface defects on the binding energy of Cu clusters, a reduced rutile (110) surface is built by removing bridging oxygen surface atoms from a perfectly stoichiometric surface slab. Similarly, an oxidized

TiO₂ (110) surface is created by adding oxygen atoms on top of five-fold surface titanium atoms. The largest binding energy predicted for the systems considered here is calculated for the Cu₁₄₇ cluster on oxidized TiO₂(110). This enhanced bonding is in agreement with both experimentally observed findings and DFT calculations for clusters of Au^{151, 153} and Ag^{152, 153} on the same oxidized surface. In addition, through charge distribution analysis of Cu₅₅ on non-stoichiometric TiO₂(110), shown in Figure 4-4, it is clear that while the charge distribution of external Cu cluster atoms are similar as the oxidation state of the surface changes, the number of positively charged Cu atoms at interfaces increases when the clusters are supported on the oxidized surface. The positively charged Cu atom corresponds to a metal-oxide bond between Cu and O that is responsible for the higher bonding energy to the surface.

The agreement between the predictions of the COMB potential, experimental data, and DFT calculations indicates that third-generation COMB potentials for Ti/TiO₂ and Cu/Cu₂O may be used to model Cu/TiO₂ interfaces. However, to capture more complex phenomena, such as Cu cluster or thin-film growth, additional modification of the potential fitting database to emphasize quantities such as diffusion barriers may be necessary.

4.3 Summary

The work described here summarizes the development of an empirical, variable charge potential for Ti and TiO₂ systems within the third-generation COMB potential framework. We also carried out first-principles DFT calculations to determine the phase order of TiO₂ polymorphs. The developed potential is fitted to, and captures most of, the structural, energetic and mechanical properties of Ti metal and TiO₂ rutile phases. In addition, rutile is correctly predicted to be more stable than the high pressure or

hypothetical AB_2 phases. The potential generally reproduces the surface stability of three low Miller index rutile surfaces although their energies are overestimated. Combining the Ti/TiO₂ potential developed in this work with the previously developed COMB potential for the Cu/Cu₂O¹⁵⁵ system, we demonstrate that the adsorption energies of Cu atoms and clusters on the TiO₂(110) surface strongly depend on Cu-O interactions. Higher binding energies result from a larger number of Cu-O bonds formed at the Cu/TiO₂ interface. Therefore, in this work, COMB predicts that Cu₁₄₇ has the largest binding energy compared to the other clusters considered. Charge transfer is predicted to take place between Cu clusters and the TiO₂ surface that results in positively charged clusters. Additionally, COMB predicts an enhanced bonding between Cu clusters and the oxidized surface, which is consistent with findings from both experimental observations and DFT calculations for late transition metals (Au and Ag) on oxidized TiO₂(110).

Thus, the third-generation COMB potential for Ti/TiO₂ is shown to successfully capture many of the important trends for these materials and be transferrable when combined with previously developed potentials to model heterogeneous interfacial systems.

Table 4-1. Properties of Ti reproduced or predicted by the COMB3 potential developed in this work, and compared to experimental results, DFT calculations and the MEAM potential.

Properties	Exp.	DFT ⁺	COMB	MEAM ⁺
a_0^* (Å)	2.951	2.948	2.935	2.931
c_0^* (Å)	4.684	4.667	4.705	4.678
c_0/a_0	1.587	1.583	1.602	1.596
E_c^* (eV/atom)	-4.844	-5.171	-4.843	-4.831
C_{11}^* (GPa)	176	172	156	174
C_{12}^* (GPa)	87	82	86	95
C_{13}^* (GPa)	68	75	80	72
C_{33}^* (GPa)	191	190	170	190
C_{44}^* (GPa)	51	45	31	58
C_{66} (GPa)		28 ⁺⁺	36	
B^* (GPa)	110	111	104	113
G^* (GPa)	52	47	36	55
E (fcc-hcp) [*] (meV/atom)	60	58	65	39
E (bcc-hcp) [*] (meV/atom)	70	108	100	111
Vacancy [*] (eV/defect)		2.03	2.34	2.24
Interstitial [*] (eV/defect)		2.58	4.39	2.64
$\gamma(0001)$ (mJ/m ²)	1920	1939 ⁺⁺	1341	1474
$\gamma(1\bar{1}00)$ (mJ/m ²)	1920	2451 ⁺⁺	1405	1554
$\gamma(2\bar{1}\bar{1}0)$ (mJ/m ²)	1920	1875 ⁺⁺	1677	1682

* Denotes fitted properties for the COMB potential

+ DFT and MEAM values from Ref.[¹⁵⁶⁻¹⁵⁸] unless otherwise specified

++ Our DFT calculation

Table 4-2. Properties of the rutile, anatase, and brookite phases calculated by the COMB potential. The properties are compared to experiments, DFT calculations (values without references are our calculations), and three other empirical potentials.

Rutile TiO ₂						
Properties	Exp.	DFT	COMB	SMB-Q ^f	MS-Q ^g	Matsui ^h
a ₀ [*] (Å)	4.594	4.646	4.562	4.581	4.587	4.493
c ₀ [*] (Å)	2.959	2.970	2.967	2.966	2.958	3.008
E _c [*] (eV/TiO ₂)	-19.90	-26.95	-19.19	-19.90	-16.49	-39.80
B [*] (GPa)	218 ^a	211 ^b	266	228	229	237
G [*] (GPa)	124 ^a	136 ^b	125		87	116
C ₁₁ [*] (GPa)	268 ^a	270 ^b	318	293	294	322
C ₁₂ [*] (GPa)	175 ^a	172 ^b	257	203	202	230
C ₁₃ [*] (GPa)	147 ^a	147 ^b	182	164	168	147
C ₃₃ [*] (GPa)	484 ^a	468 ^b	516	400	423	444
C ₄₄ [*] (GPa)	124 ^a	116 ^b	123	128	96	123
C ₆₆ [*] (GPa)	190 ^a	216 ^b	204	183	190	226
q _{Ti} (e)		2.26	1.91	2.51	1.15	2.20
Anatase TiO ₂						
a ₀ (Å)	3.785	3.806	3.849	3.825	3.850	3.770
c ₀ (Å)	9.512	9.714	9.135	9.030	9.060	9.568
E _c [*] (eV/TiO ₂)		-27.03	-19.06	-19.84	-8.19	-39.49
B (GPa)	59-178 ^c	180	234	220	176	176
G (GPa)		57	126		66	59
q _{Ti} (e)		2.24	1.88		1.12	2.20
Brookite TiO ₂						
a ₀ (Å)	9.184 ^d		9.368	9.259	9.113	9.146
b ₀ (Å)	5.449 ^d		5.424	5.444	5.449	5.389
c ₀ (Å)	5.145 ^d		5.046	5.229	5.170	5.144
E _c [*] (eV/TiO ₂)			-19.11	-19.65	-8.21	-39.62
B (GPa)	255 ^e		261	227	211	200
G (GPa)			124		83	92
q _{Ti} (e)			1.89		1.14	2.20

* Denotes fitted properties for COMB potential

- a Reference ¹⁵⁹ h Reference ¹²²
b Reference ¹⁶⁰ g Reference ¹¹⁹
c Reference ¹⁶¹
d Reference ¹⁶²
e Reference ¹⁶³
f Reference ¹²⁷

Table 4-3. Cohesive energies of rutile titania (eV/TiO₂ unit) and that relative to rutile titania for other polymorphs (AB₂ phases) calculated from COMB potential for TiO₂ developed in this work in comparison with DFT calculations and other empirical potentials.

Polymorph (space group)	Exp.	DFT	COMB3	MS-Q ^b	Matsui ^c	SMB-Q ^d
<i>Normal phases</i>						
Rutile (P4 ₂ /mmn)		-26.949	-19.189	-8.248	-39.798	-19.90
Anatase (I4 ₁ /amd)	0.035 ^a	-0.083	0.129	0.057	0.304	0.060
Brookite (Pbca)	0.008 ^a	-0.046	0.080	0.037	0.178	0.250
<i>High pressure phases</i>						
Columbite (Pbcn)		0.006	0.010	0.074	0.035	-
Cotunnite (Pnma)		0.107	0.739	0.553	0.914	-
Baddeleyite (P2 ₁ /c)		0.066	0.667	0.515	-	-
Fluorite (Fm-3m)		0.775	1.118	1.020	0.580	-
<i>Hypothetical phases</i>						
Pyrite (Fm-3m)		-	0.253	-	-	-
Hollandite (I4/m)		-	0.275	-	-	-
Ramsdellite (Pnma)		-	0.263	-	-	-

^a Reference ¹⁶⁴

^b Reference ¹¹⁹

^c Reference ¹²²

^d Reference ¹²⁷

Table 4-4. Low index surface energies (J/m²) of rutile TiO₂ from the *ab initio* approaches and empirical potentials.

Method	Surface formation energy (J/m ²)		
	(110)	(100)	(001)
<i>ab initio</i>			
PBE (Crystal03) ¹⁴³	0.42	0.69	1.39
LDA (Crystal03) ¹⁴³	0.90	1.20	1.88
B3LYP (Crystal03) ¹⁴²	1.10		
<i>Empirical potentials</i>			
<u>Fix charged</u>			
CFR ^{119, 144}	0.95	1.24	2.20
MA ^{119, 122}	1.77	2.07	2.40
<u>Variable charged</u>			
MS-Q ²	1.40	1.32	1.85
SMB-Q ¹²⁷	0.60	0.85	1.74
SMTB-Q ¹⁴⁵	0.42	0.49	1.26
COMB	0.99	1.25	1.49

Table 4-5. Charge variation ($Q-Q_{\text{bulk}}$) (in e^-) of surface atoms (labeled in Figure 4-1).
The charges of Ti and O in bulk rutile are 1.905 and -0.953, respectively.

$Q-Q_{\text{bulk}}$	CN	DFT	COMB
TiO ₂ (110)			
O(1)	2	0.18	0.28
O(2)	3	-0.04	-0.08
Ti(1)	5	-0.03	-0.02
Ti(2)	6	-0.06	-0.08
TiO ₂ (100)			
O(1)	2	0.18	0.20
O(2)	3	-0.02	-0.09
O(3)	3	-0.01	-0.04
Ti(1)	5	-0.09	-0.05
TiO ₂ (001)			
Ti(1)	4	-0.15	-0.09
Ti(2)	6	0.05	0.02
O(1)	2	0.05	0.11
O(2)	3	0.04	-0.05

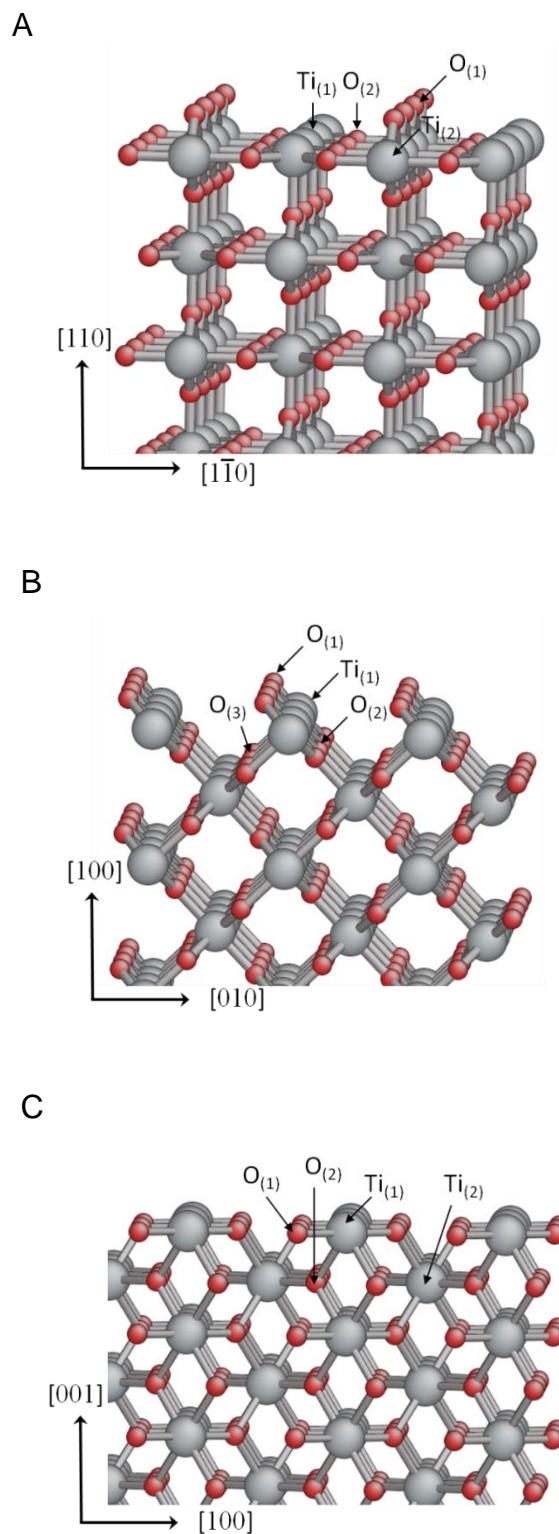


Figure 4-1. Model of the rutile TiO₂ surfaces. A) (110), B) (100), and C) (001) surfaces. Ti and O atoms are represented by big (grey) and small (red) spheres. The surface atoms for charge transfer calculations are labeled by element type and Arabic numbers.

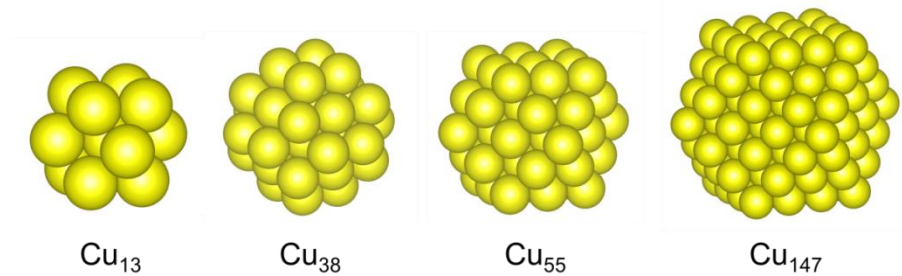


Figure 4-2. Optimized geometries of Cu_{13} , Cu_{38} , Cu_{55} , and Cu_{147} clusters.

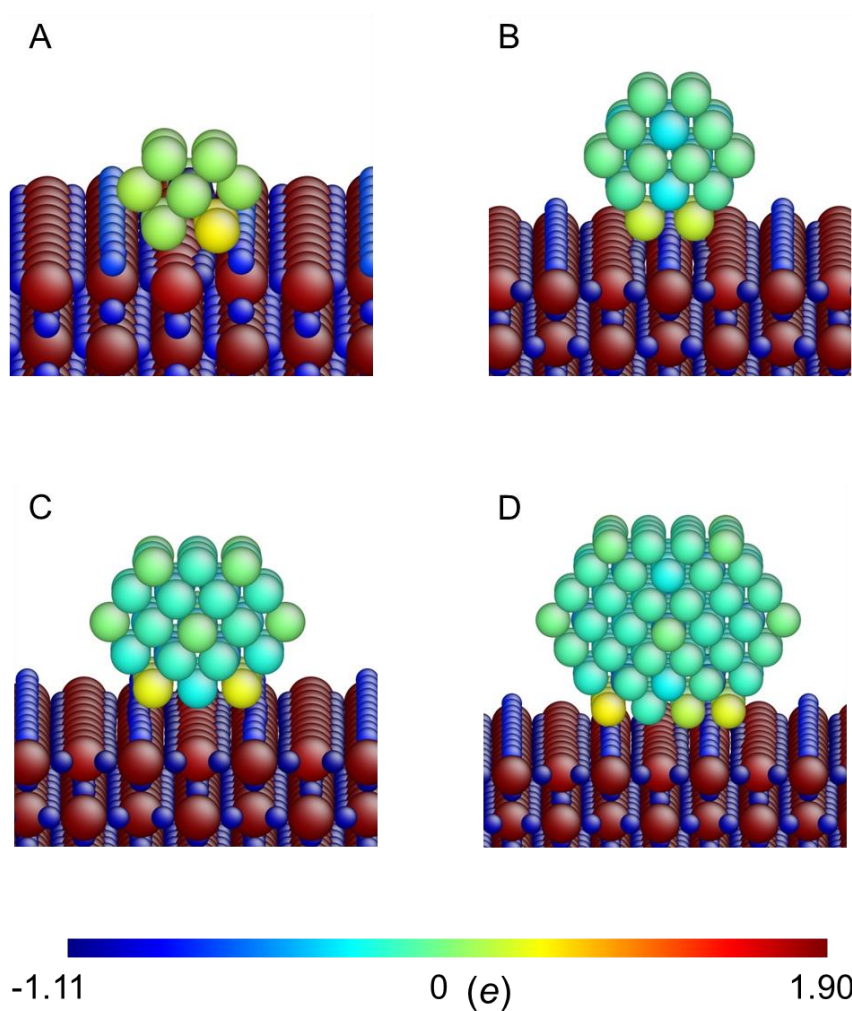


Figure 4-3. Charge distribution of relaxed Cu clusters on $\text{TiO}_2(110)$. A) Cu_{13} , B) Cu_{38} , C) Cu_{55} , and D) Cu_{147} . Large atoms are Ti, medium sized atoms are Cu and small atoms are oxygen.

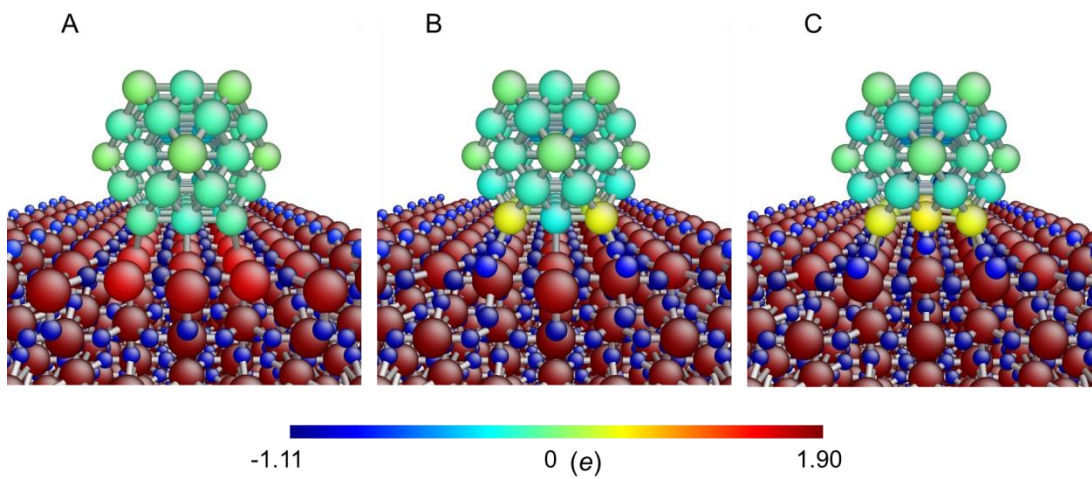


Figure 4-4. Charge distribution of relaxed Cu_{55} clusters on the stoichiometric and defected $\text{TiO}_2(110)$ surfaces. A) Reduced, B) stoichiometric, and C) oxidized $\text{TiO}_2(110)$ surfaces. Large atoms are Ti, medium sized atoms are Cu and small atoms are oxygen.

CHAPTER 5

DEVELOPMENT OF COMB3 TI/TiN POTENTIAL AND ITS APPLICATIONS ON Ti/TiN INTERFACES AND THE DEPOSITION OF ATOMIC OXYGEN ON TiN(001) SURFACE

Titanium nitride (TiN) thin films are notable for their distinctive properties, which include extreme hardness (2000 kg/mm²), high melting temperature (2950 °C), and a small thermal expansion coefficient ($9.4 \times 10^{-6} \text{ }^\circ\text{C}^{-1}$).³⁸ They have consequently been widely used as wear-resistant coatings on cutting and grinding tools,^{3, 165, 166} corrosion-resistant coverings on mechanical parts,^{167, 168} and diffusion barriers in microelectronic devices¹⁶⁹. More recently, TiN thin films have been used in medical implants^{170, 171} because of their biocompatibility with bony tissue. All of these applications are highly dependent on the nature of the interface structure between TiN and the underlying substrate. Therefore, achieving a better understanding of the properties of these highly heterogeneous interfaces across length scales will allow us to better enhance the utilization of TiN thin films.

In the case of the TiN system, the bulk and surface properties of TiN have been studied by Marlo *et al.*¹⁷² using density functional theory (DFT) with various exchange-correlation functions. However, there are only a few empirical potentials for TiN in the literature. The first interatomic potential description of TiN was reported by Hernández *et al.*¹⁷³ in the form of a rigid-ion model. However, no information was provided on how this potential can reproduce the fundamental physical properties of TiN system. Later, an extended Tersoff-type potential of TiN was developed by Iwasaki *et al.*¹⁷⁴. In this case, although the details of the potential formalism and parameters are provided, the structural and elastic properties of TiN were not discussed. Kim *et al.*¹⁷⁵ developed a potential based on the second nearest-neighbor modified embedded-atom method

(2NN MEAM). They provided the parameters and to extensively discussed its ability to predict the properties of TiN. Later, the parameters of Kim *et al.* were modified slightly by Yu *et al.*¹⁵⁶ for a better description of physical properties of Ti₂N. Most recently, Xu *et al.*¹⁵⁷ combined the 2NN MEAM potential with Ziegler-Biersack-Littmark (ZBL) repulsive potential to examine the growth of TiN films on the TiN(001) surface in MD simulation; the results indicated that the TiN film grows via layer-by-layer growth mode.

The purpose of the present work is to develop an interatomic, third-generation COMB potential for the Ti-N system compatible with the developing potential of Ti-O and N-O systems. This thus enables the simulation of complex Ti-N-O phenomena, such as oxidation of TiN.

5.1 Potential development and Properties of Ti, N₂, and TiN

5.1.1 Fitting Procedure

The element-type parameters are fit for pure elements (Ti and N) and bond-type parameters for binary systems (TiN). In the present work, the element-type parameters of Ti are implanted from the established COMB potential for Ti/TiO₂ system,¹⁷⁶ where the fitting structures for metallic Ti include the hexagonal closed packed (*hcp*), face-centered cubic (*fcc*), body-centered cubic (*bcc*), simple cubic, and diamond phases. For N, the binding energy and bond length of N₂ molecule are fitted to experimental values.

For the bond-type parameters, to ensure the phase stability of the ground state, the fitting structures for TiN system include rocksalt ground state (B1, space group: $Fm\bar{3}m$), wurtzite (B4, space group: $P6_3mc$), zincblende (B3, space group: $F\bar{4}3m$), and cesium chloride (B2, space group: $Pm\bar{3}m$). Because Ti₂N can form stable intermediate phases according to the Ti-N phase diagram, we also consider four fitting structures for

the Ti₂N system, which are rutile (space group: $P4_2/mmm$), which is the ground state structure of Ti₂N, fluorite (space group: $Fm\bar{3}m$), F₂N-type (space group: $P\bar{3}m1$) and Cu₂O-type (space group: $Pn\bar{3}m$) structures. All the fitted structures considered are illustrated in Figure 5-1.

The physical properties of the TiN rocksalt phase are of the most interest. We therefore include the lattice constants, elastic properties, defect formation energies, and surface energies of this phase in the fitting from published experimental data and DFT calculations. In those cases where reliable data could not be obtained from the literature, we performed our own DFT calculations to complete the data set for fitting and comparison. The DFT calculations were carried out with the Vienna *ab initio* Simulation Program (VASP)^{61, 62, 177, 178} within the generalized-gradient approximation (GGA), using the Perdew–Burke–Ernzerhof (PBE)⁴³ exchange–correlation functional. Ti3p⁶3d³4s¹ and N2s²2p³ were taken as the valence electrons. A plane-wave basis with a 400 eV energy cutoff and a 6×6×6 Monkhorst-Pack k-point mesh^{179, 180} were used. The convergence criteria for energies and forces were set at 1×10⁻⁵ eV and 1×10⁻² eV·Å⁻¹, respectively. For N₂ molecule, the electronic structure calculations were performed using the Gaussian09¹⁸¹ computational chemistry software package. The geometric optimization was carried out using B3LYP/6-311G*,⁶³ and the ionization energies are calculated with the CCSD(t)/cc-pVTZ^{182, 183} level of theory.

5.1.2 Fitted Properties of Ti metal and N₂ molecule

The static properties of lattice constants for Ti metal are provided in Table 4-1, where the *hcp* structure is the ground state phase for Ti metal. In the case of the N₂ molecule, the bond length and bonding energy match well the experimental values,¹⁸⁴

which are 1.098 Å for COMB vs. 1.099 Å in experiment and -9.76eV vs. -9.80 eV per molecule.

5.1.3 Fitted and Predicted TiN Phase Stability and Properties

Table 5-1 compares the physical properties of TiN polymorphs fitted or predicted by the COMB potential with values from published experimental data, DFT calculations, and second nearest-neighbor modified embedded-atom method (2NN MEAM) potential.¹⁸⁴

In order to determine the phase stability in TiN and Ti₂N systems, the enthalpy of formation, ΔH_f , is fitted. The definition of the enthalpy of formation of a compound is the change of enthalpy from the formation of one mole compound from its constitutive elements in their standard states: hcp Ti metal and an isolated N₂ molecule, respectively. As shown in Table 5-1, the rocksalt and rutile phases are correctly fitted as the most stable for TiN and Ti₂N systems, respectively.

For the TiN system, which is the phase of primary interest, the COMB potential not only successfully fits the lattice constant and enthalpy of formation for the rocksalt structure to experimental data, but also reproduces the correct phase order of rocksalt, wurtzite, zincblende, and cesium chloride. The fitted energy differences between the rocksalt phase and hypothetical phases of wurtzite, zincblende, and cesium chloride are also in good agreement with the results of DFT calculations. With regard to the elastic properties, COMB does a better job of fitting the values of C_{11} , C_{22} , and C_{44} than the 2NN MEAM potential, as illustrated in Table 5-1. In particular, the largest deviation of elastic constants with respect to the experimental values is 4% for COMB and 12% for 2NN MEAM due to its larger overestimation of C_{44} .

In the case of the Ti₂N system, the rutile phase is correctly fitted to be the ground state structure. However, the agreement between fitted and experimental values for the lattice constants and the enthalpy of formation for the rutile structured Ti₂N are only fair. Nevertheless, COMB successfully reproduces that the formation TiN is favored over the formation of Ti₂N based on the standard state conditions used in the enthalpy of formation calculations. This is important for the atomic-scale study of TiN alloys.

5.1.4 Predicted Defect Formation Energies and Surface Energies of rocksalt TiN

The defect formation energies for the Ti-vacancy (V_{Ti}), N-vacancy (V_N), Ti-interstitial (I_{Ti}), and N-interstitial (I_N), and the Schottky and Frenkel complexes have been determined for the TiN rocksalt structure. The vacancies are generated by removing an atom of Ti or N from the lattice sites, while interstitials are created by placing a Ti or N atom in the tetrahedral position. The Schottky defects are created by the association of a Ti and an N vacancy that are separated by a distance of 4.77 Å to prevent their direct interaction. Similarly, to prevent the recombination of Frenkel or anti-Frenkel, the vacancy and interstitial are separated by 4.63 Å.

Table 5-2 compares the defect formation energy predictions of the COMB potential with published DFT results¹⁷³. The defect formation energies, E^f , were calculated with the standard equation,

$$E^f = E^{def} - E^{perf} \pm \sum_i n_i \mu_i, \quad (5-1)$$

where E^{def} and E^{perf} are the energies of defective and perfect bulk structures, respectively, n_i is the number of defects and μ_i is the chemical potential of the atom added or removed. These energies were not part of the fitting dataset of physical properties; COMB predicts generally larger values of defect formation energies than

DFT. Nevertheless, COMB predicts defect-formation energies with a fidelity similar to that of DFT, which the nitrogen vacancy and the Schottky defect predicted to be the most stable point defect and defect complex, respectively. This gives confidence that the COMB potential captures much of the correct physics.

In addition to the formation of defects, the predictions for the surface stability of TiN were investigated. To simulate surfaces, a vacuum of 25 Å is added in the direction normal to the surface within the simulation box, thereby forming a slab with two free surfaces. To facilitate comparison, the surfaces are relaxed until the force on each atom is closed to zero and there is a minimal fluctuation in total energy. For the (001) and (110) surfaces, which are nonpolar, the number of Ti cations and N anions within each layer is identical. Therefore, a stoichiometric slab with two identical surfaces may be created. In contrast, the TiN (111) surface is polar and is constructed with alternating layers of Ti cations and N anions. It therefore is expected that a rocksalt (111) surface will undergo reconstruction¹⁸⁵ to minimize the surface dipole. In this study, a stoichiometric slab with Ti- and N-terminated surfaces for TiN (111) is created for the surface energy calculation. The surface energies, σ , were calculated by using the following standard equation¹⁸⁵:

$$\sigma = \frac{1}{A} (E_{slab} - nE_{bulk}), \quad (5-2)$$

where E_{slab} is the total energy of the slab for the surface energy calculation, E_{bulk} is the energy per atom of the perfect bulk structure, n is the total number of atoms in the slab, and A is the total area of surfaces (top and bottom) of the slab. Table 5-3 compares the surface energies predicted by COMB to the results of DFT calculations and MEAM

potentials. The surface energy trend predicted by COMB is $(100) < (110) < (111)$, which is consistent with the trend predicted by DFT.

Overall, COMB potential correctly reproduces the phase stability, lattice constant, and elastic constant of TiN rocksalt structure compared to the experimental value and DFT calculations. However, the underestimation for the surface energy of the TiN(111) polar surface needs a further improvement.

5.2 Predicted Dynamical Results

The potentials fitting performed using calculations carried out at 0 K. To verify that there are no unphysical phase transformation during MD simulations at high temperatures, the rocksalt phase TiN is heated to 3500 K and then cooled to 300 K.¹⁸⁶ The simulation cell has dimensions of $10a \times 10a \times 10a$ ($a = 4.242 \text{ \AA}$, lattice constant of TiN) and consists of 8000 atoms in the stoichiometric rocksalt structure. All of the simulations are performed using the LAMMPS software.

The system is initially equilibrated at 2000 K for 100 ps in the constant-temperature-and-pressure (NPT) ensemble until the total energy variation and total pressure of the simulation box is below the values of convergence, which are both at $1 \times 10^{-4} \text{ eV}$ and $1 \times 10^{-2} \text{ eV} \cdot \text{\AA}^{-1}$. Next, several successive equilibration calculations are carried out by increasing the temperature at intervals of 100 K up to 3500 K. At each temperature, the system is equilibrated for 40 ps. Figure 5-3(a) shows the change of the crystal configuration as a function of temperature. At 1000 and 2000 K, the rocksalt structure of TiN is stable. At 3000 K, it is clear to see that Ti and N atoms have a larger thermal vibration but are still in their original lattice positions. Finally, at 3500 K, all of the atom positions abruptly randomize, resulting in a liquid phase. On the basis of the radial distribution function that is illustrated in Figure 5-3(b), the rocksalt structures of

TiN are maintained up to 3000 K. As for the prediction of melting point by MD,^{76, 187} because the MD structure is a defect-free crystal, it is expected that the prediction will be higher than the experimental values where the sample always has defects that facilitate the transition from the crystalline to the liquid phase. Therefore, it is only possible to indicate that the COMB potential predicts a melting point around 3000 – 3500 K on the basis of these simulations, which is in excellent agreement with the experimental melting point of 3203 K.¹⁸⁸

For the quenching process, the structure was equilibrated by following the heating procedure back down to 300 K from 3000 K. Our simulation result indicates that the heated structure returns to the rocksalt phase.

5.3 Applications of COMB3 TiN Potential

5.3.1 Adhesion of fcc-Ti/TiN(001) Interfaces

Ti/TiN multilayered structures are commonly used as barriers in ultra large scale integration (ULSI) devices for Al metallization³, or coated on steel to provide corrosion resistance¹⁸⁹ and enhance tribological properties¹⁹⁰ compared to single-layered hard coatings. Because the performance in the above applications is highly dependent on the nature of the interface between Ti and TiN, an atomic-scale approach provides important insights into the nature of the bonding at metal/ceramic interfacial structures.

Here, to demonstrate the ability of COMB3 TiN potential for describing the different bonding environments in a seamless manner, the interfacial energy between Ti and TiN was determined. Based on the x-ray diffraction analysis, TiN thin films with (001)-orientated surface were observed when they were sputter-deposited on the glass substrate.¹⁹¹ Since experimentally Ti thin films are epitaxially grown on TiN and there are only small differences in the lattice constants (~ 3.3%) between fcc Ti metal (4.10 Å)

and rocksalt TiN (4.24 Å), a coherent interface of fcc-Ti(001) || TiN(001) is expected. Here, three coherent (001) interfaces were considered between fcc-Ti and rocksalt TiN, as shown schematically in Figure 5-4 (a). For cases (1) and (2), the Ti metal interacts directly with Ti atoms and N atoms of TiN, respectively. For case (3), the Ti atoms in the metal are on the bridge site of TiN and only interact with Ti atoms in TiN.

The work of adhesion, W , was used to quantify the stability of interfaces and was calculated from the standard equation: $W = (E_{\text{Ti}} + E_{\text{TiN}} - E_{\text{Ti/TiN}}) / A$, where E_{Ti} and E_{TiN} are the total energy of relaxed fixed volume Ti and TiN slabs, respectively, $E_{\text{Ti/TiN}}$ is the total energy of the relaxed interfacial structure, and A is the interface area. All the structures were equilibrated at 300 K, prior to quenching at $T=0$ K. The calculated works of adhesion for these three interfaces are 4.45 J/m², 0.93 J/m², and 2.83 J/m², respectively. The corresponding values from DFT calculations¹⁹² are 3.56 J/m², 0.43 J/m², and 1.66 J/m², respectively. The results indicate that COMB potentials qualitatively predict the trends compared to DFT calculations. In particular, both COMB and DFT predict that the interface of Ti metal interacting with N atoms in TiN is stronger than that of Ti metal interacting with Ti atoms in TiN, which can be attributed to the stronger bonding associated with Ti-N bonding relative to Ti-Ti bonding. In addition, the atomic charge predicted by COMB for these interfaces, shown in Figure 5-4(b), indicates that the Ti and N atoms in TiN have more positive and negative charge when Ti atoms in Ti on the top sites of N or bridges site of Ti in TiN.

5.3.2 Atomic Oxygen deposition on TiN(001) surface

The adsorption of oxygen atoms on the TiN surface plays a crucial role in the TiN oxidation processes. Here, we perform two MD simulations to examine the adsorption of atomic and molecular oxygen on the TiN (001) surface through deposition.

In the case of atomic oxygen deposition, sixty oxygen atoms are deposited with an incident energy of 5 eV normal to the surface in spatially random locations. The dimensions of the TiN surface slab are $42 \text{ \AA} \times 42 \text{ \AA} \times 63 \text{ \AA}$, where the bottom layer is fixed in their bulk lattice sites to prevent the slab from translating as a result of the deposition process. The middle eight layers of TiN are thermostated using a Langevin thermostat applied to dissipate the excess energy from the deposited oxygen atoms and to maintain a constant surface temperature. The active region comprises the top six layers of the slab; these evolve under unconstrained equations of motion. The surface slab was equilibrated at 300 K for 10 ps prior to the deposition. Figure 5-5 shows the snapshots after thirty and sixty oxygen atoms have been deposited, respectively.

A majority 70% of the deposited O atoms stick to the surface. Interestingly, when the COMB potential is used to calculate the static adsorption energy for atomic oxygen on this surface, the largest adsorption energy is predicted for the atop site on the N atom, which contradicts the results of DFT calculations.¹⁹³ However, the larger cutoff distance of Ti-O (3.2 \AA) compared to N-O (2.3 \AA) within the potential leads the oxygen atoms to preferably adsorb on top of the Ti atoms in the MD simulations, in agreement with the results of DFT calculations. The simulations further predict that 10% of the incident oxygen atoms rebound from the surface, and 20% of the incident oxygen atoms form O₂ molecules in the vacuum above the surface.

In the case of the simulation of O₂ deposition, a single oxygen molecule is given an given incident energy of 5 eV per molecule and placed 5.0 Å above a TiN (001) surface slab with the same dimensions and characteristics as described above for the atomic O deposition case. The oxygen molecule binds initially to a Ti atom. Subsequently, it moves to a bridge position over two Ti atoms and then dissociates, as illustrated in Figure 5-6. These results are consistent with the findings of a study by Piskanec *et al.*¹⁹⁴ who analyzed the early oxidation stages of TiN(100) by means of first-principles molecular dynamics (FPMD). The bridge Ti atoms will be the preferred adsorption site for the oxygen molecule. Thus, through a combination of characteristics these examples demonstrate the fact that the third-generation COMB potential may be used to examine TiN oxidation via MD simulations.

5.4 Summary

In summary, an empirical, variable charge potential for TiN systems was successfully developed based on the COMB3 potential framework. The potential captures most of the physical properties of TiN rocksalt phase. Because the TiN is the primary interest in the work, it is acceptable that the fitted lattice constants and enthalpy of formation for Ti₂N rutile phase are only fair compared to experimental values. Nevertheless, COMB3 successfully reproduces that the formation TiN is favored over the formation of Ti₂N. This is important for the atomic-scale study of TiN alloys. Furthermore, the COMB3 Ti/TiN potentials correctly determine the work of adhesion on different interfacial structures of fcc-Ti(001)/TiN(001) and to characterize the adsorption of oxygen atoms and molecules on the TiN(001) surface through deposition. In particular, the Ti/TiN potential could be easily integrated with other existing COMB

potentials, which facilitate variety studies of disparate systems at the large-scaled MD simulations.

Table 5-1. COMB predictions compared to published experimental results, DFT calculations, and MEAM potentials for the lattice constants a_0 and c_0 (Å), enthalpy of formation ($\Delta_f H$) (eV/atom), cohesive energy (E_c), bulk modulus (B), shear modulus (G) and elastic constants of the rocksalt (B1) TiN and rutile Ti₂N. (The reference states for the heats of formation are hcp Ti and gaseous N₂)

		Exp.	DFT	COMB	2NN-MEAM ^b	2NN-MEAM ^c
TiN (B1)	a_0^*	4.242	4.238	4.243	4.242	
	$\Delta_f H_{B1}^*$	-1.74	-1.70	-1.75	-1.74	-1.82
	E_c			-6.63		-6.69
	B^*	320 ^a		318	320	288
	G			183		
	C_{11}^*	625 ^a		634	659	561
	C_{12}^*	165 ^a		165	150	152
	C_{44}^*	163 ^a		157	183	191
	$\Delta_f H_{B4} - \Delta_f H_{B1}^*$		0.12	0.23		
	$\Delta_f H_{B3} - \Delta_f H_{B1}^*$		0.34	0.41		0.39
	$\Delta_f H_{B2} - \Delta_f H_{B1}^*$		0.89	0.87		1.25
Ti ₂ N (rutile)	a_0^*	4.943		4.842	4.783	4.777
	c_0^*	3.036		2.924	3.051	3.048
	$\Delta_f H_{Rutile}^*$	-1.38	-1.26	-1.26	-1.63	-1.63
	$\Delta_f H_{Fe_2N} - \Delta_f H_{Rutile}$		0.72	0.23		0.015
	$\Delta_f H_{Fluorite} - \Delta_f H_{Rutile}$		0.62	0.34		
	$\Delta_f H_{Cu_2O} - \Delta_f H_{Rutile}$		0.68	0.45		

* Denotes fitted properties for COMB potential

^a Ref.[¹⁹⁵]

^b Ref.[¹⁹⁶]

^c Ref.[¹⁵⁶]

Table 5-2. Comparison of formation energies (eV) of point defects in NaCl typed TiN crystal calculated from first-principles calculations and COMB potentials. The chemical potentials of Ti and N are hcp Ti metal and an isolated N₂ molecule, respectively.

Defects	<i>DFT</i>	<i>COMB</i>
N vacancy	3.38 ^a , 2.41 ^{b,c}	3.11
Ti vacancy	4.19 ^a , 3.28 ^c	4.72
N interstitial	5.46 ^b , 4.93 ^c	13.82
Ti interstitial	8.28 ^c	24.27
Schottky	5.28-5.80 ^c	7.22
Cation Frenkel	11.56 ^c	28.98
Anion Frenkel	7.34 ^c	16.93

^a Ref.[¹⁵⁸]

^b Ref.[¹⁹⁷]

^c Ref.[¹⁹⁸]

Table 5-3. Relaxed surface energy of TiN (100), (110) and (111) surface predicted by COMB potentials, in comparison with the predictions from published first-principles calculation and MEAM potentials.

Surface (J/m ²)	COMB	MEAM	First-principles calculations
(100)	1.41	1.30 ^a , 1.66 ^b	1.06–1.30 ^c
(110)	2.07	2.46 ^a , 3.01 ^b	2.59–2.86 ^c
(111)	2.54	3.65 ^a , 5.28 ^b	4.59–4.95 ^c

^a Ref.[¹⁹⁹]

^b Ref.[¹⁵⁶]

^c Ref.[¹⁵⁷]

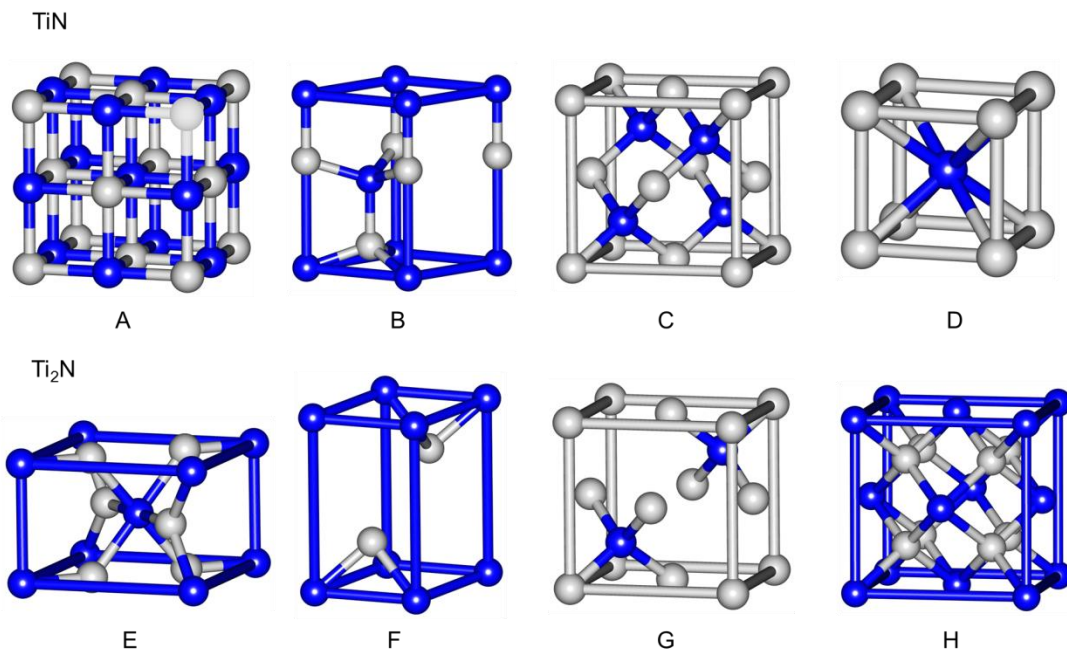


Figure 5-1. The unit cell of fitting structures for TiN and Ti₂N systems in this study. A) NaCl, B) wurtzite, C) ZnS, D) CsCl, E) rutile, F) Fe₂N, G) Cu₂O, and H) fluorite. Grey and blue atoms denote Ti and N atoms.

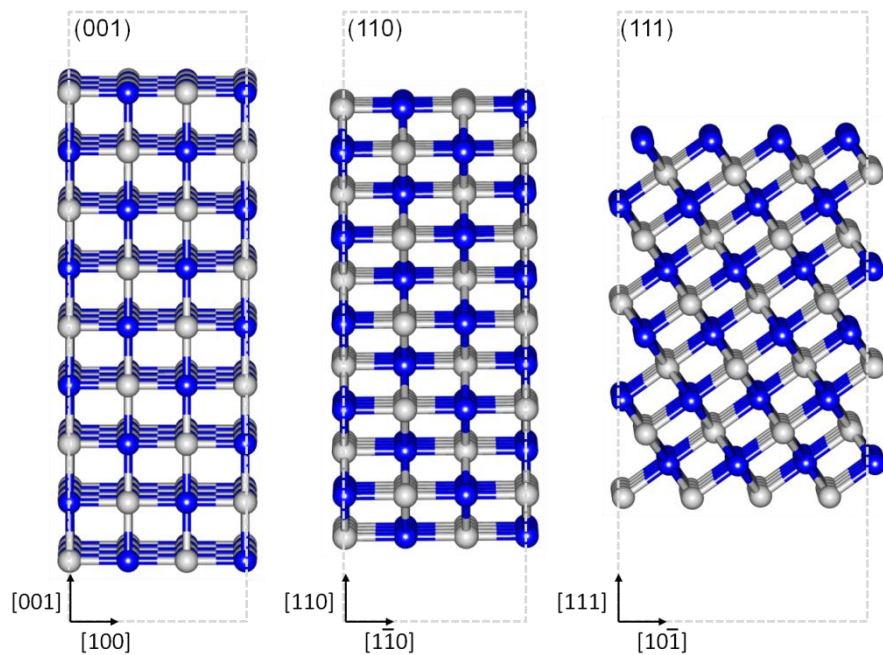
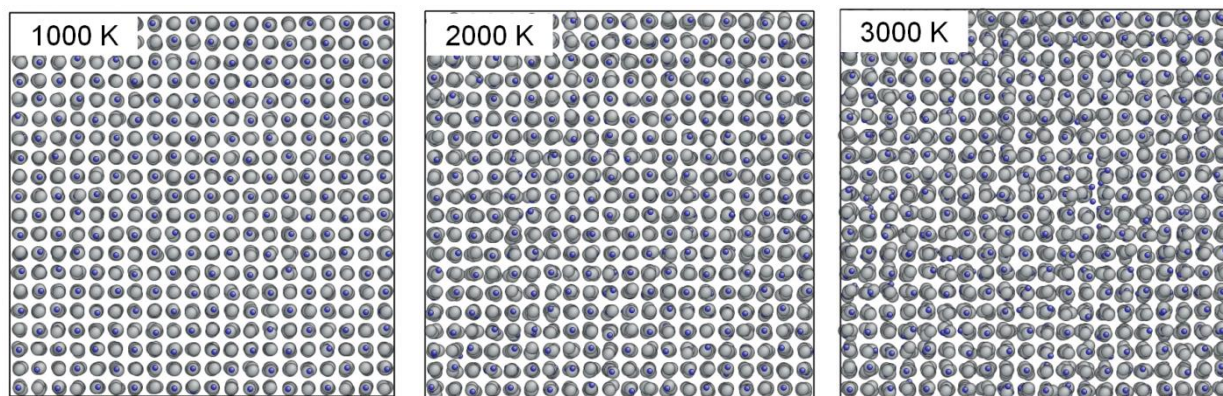


Figure 5-2. Schematic of layers sequence of the TiN(001), (110), (111) surfaces. Grey and blue atoms denote Ti and N atoms.

A



B

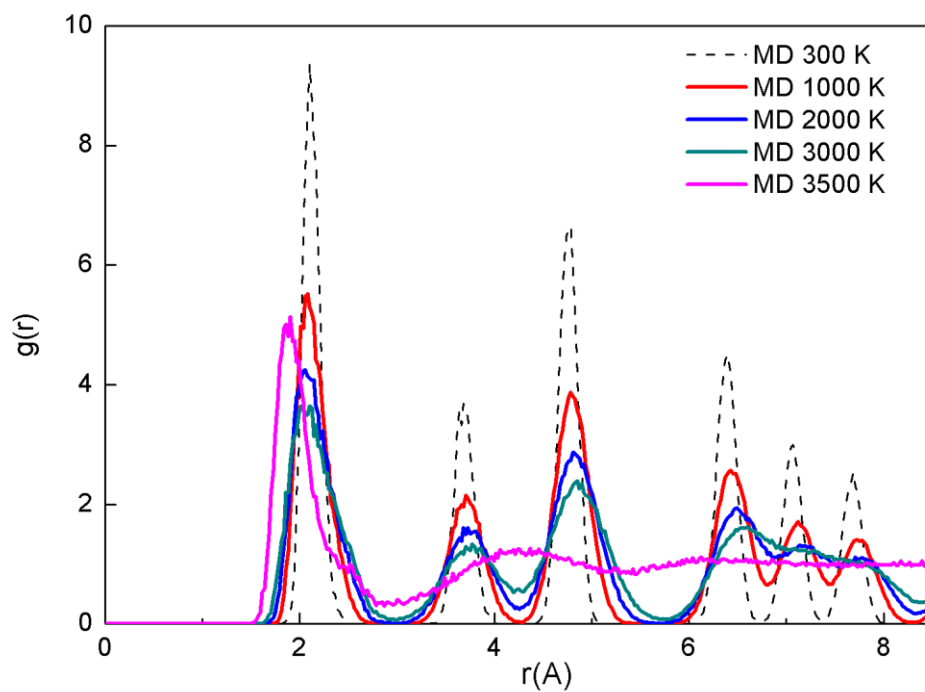
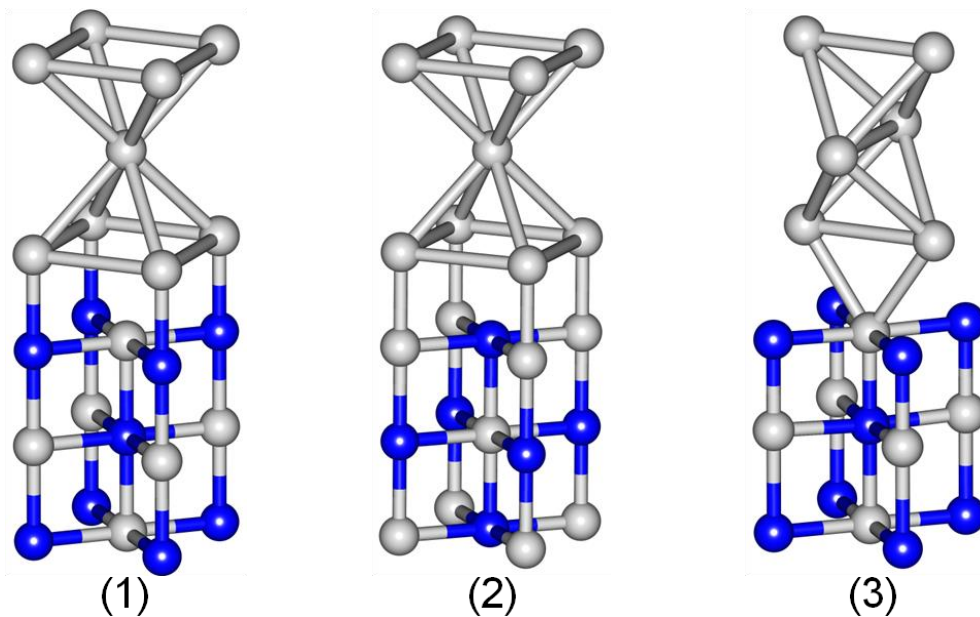


Figure 5-3. The crystal structures of rocksalt TiN as a function of temperature. A) The atomic configurations where grey and blue atoms denote Ti and N atoms. B) The pair distribution functions for the Ti-N for rocksalt TiN from MD simulations at 300, 1000, 2000, 3000, and 3500 K.

A



B

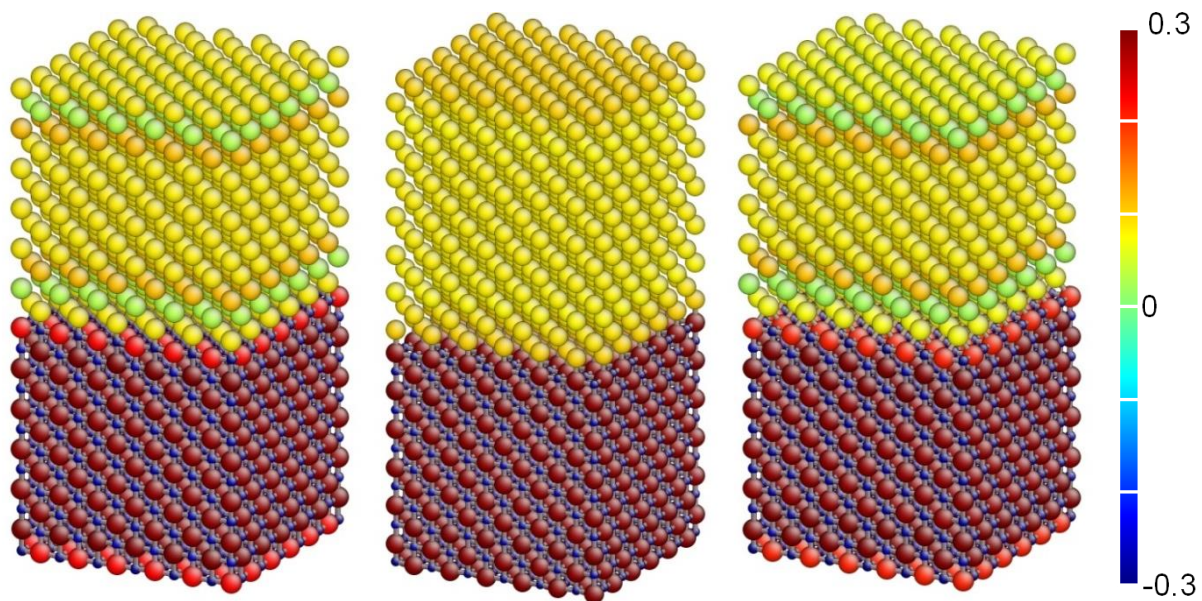


Figure 5-4. The interfacial structures of Ti(001)/TiN(001), where Ti atoms in Ti metal are on the atop site of N, Ti and bridge site of Ti, respectively. A) DFT calculations; the color scheme is the same as in Figure 1. B) MD using COMB3; the atoms are color coded by atomic charge as indicated by the color bar.

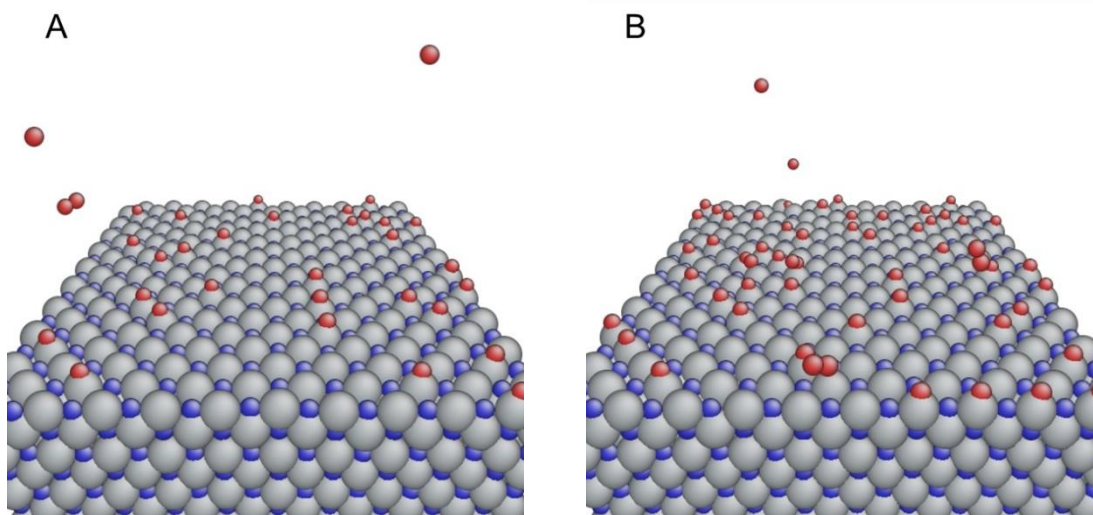


Figure 5-5. Snapshots of oxygen atoms deposited on the TiN(001) surface. A) thirty and B) sixty oxygen atoms deposited. The color scheme is the same as in Figure 1.

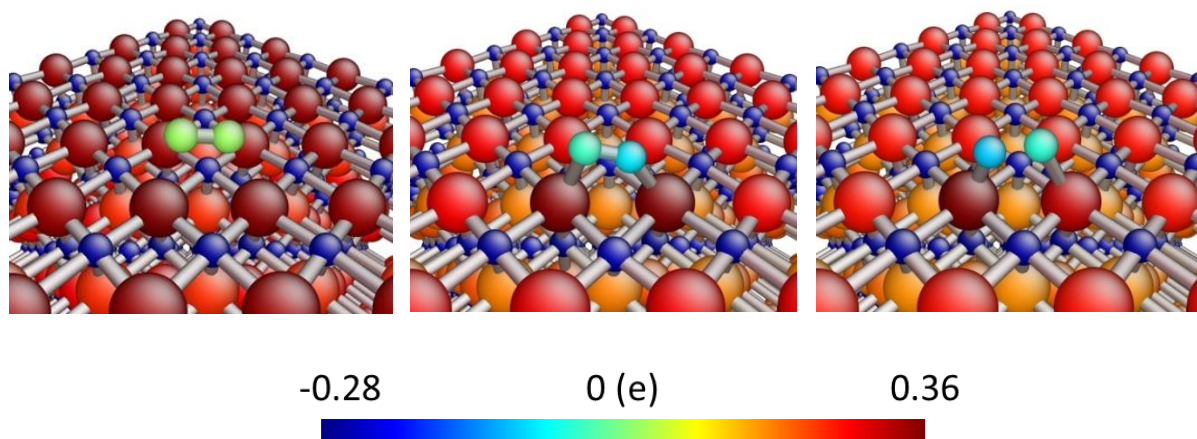


Figure 5-6. Snapshots from the deposition of single oxygen molecule on the TiN(001) surface. The atoms are color coded by the atomic charges with the charge values indicated by the color bar.

CHAPTER 6 FIRST-PRINCIPLES STUDY OF EARLY STAGE OXIDATION OF FACETED AlN SURFACES

Alumina nitride (AlN) has great potential for use as a thermal barrier material in protective coatings due to its properties of high theoretical thermal conductivity (320W/mK) and a small thermal expansion coefficient ($4.6 \times 10^{-6}/^{\circ}\text{C}$). It has been experimentally²⁰⁰⁻²⁰² demonstrated that when AlN is exposed to air at high temperature it is oxidized, influencing its chemical structure and thermal conductivity. Previous computational studies have investigated the adsorption of oxygen on flat AlN nonpolar²⁰³ and polar^{204, 205} surfaces, but the influence of surface features and defects have yet to be taken into account in such calculations. For example, the reduced coordination of surface steps can substantially influence surface reactivity as has been demonstrated for the adsorption and dissociation of oxygen molecules on metal surfaces,²⁰⁶⁻²¹⁰ which show enhanced reactivity at steps in terms of smaller bond-breaking energy barriers with respect to terrace sites.

In this work, we use first-principles, density-functional theory (DFT) calculations to investigate the role of surface steps on the adsorption of oxygen molecules and their subsequent dissociation on the AlN ($10\bar{1}0$) surface with a monoatomic step. To quantify the surface reactivity, the results are further compared to the energetics associated with a flat AlN ($10\bar{1}0$) surface.

6.1 Computational Details

The DFT calculations are carried out using the Vienna *ab initio* simulation package (VASP).⁵⁹⁻⁶² The exchange-correlation energy and potential are treated within the generalized gradient approximation (GGA) using the functional of Perdew–Burke–

Ernzerhof (PBE).⁴³ The valences electron orbitals for elements are $Al3s^23p^1$, $N2s^22p^3$, and $O2s^22p^4$, respectively. The energy cutoff for the plane wave basis is 500 eV.

The AlN (10 $\bar{1}0$) surface was built from the PBE optimized bulk AlN wurtzite structure. The properties of bulk AlN predicted by the DFT calculations are summarized in Table 6-1 and they compare well to published experimental values. The AlN(10 $\bar{1}0$) surface structure is an eight-layer slab with 64 atoms and is modeled using a 2x2 unit cell, while the corresponding stepped surface is modeled by a 4x3 system. A 14 Å vacuum space is added to separate the slabs, which is determined to be sufficient to prevent surface slabs from interacting with one another through the periodic boundary conditions. The side and top views of the flat and stepped AlN(10 $\bar{1}0$) surface structure are illustrated in Figure 6-1. In the calculations, the Brillouin zone is sampled with a 4x4x1 Monkhorst–Pack (ref) k-point mesh. The convergence criteria are set at 1×10^{-5} eV and 1×10^{-2} eV·Å⁻¹ for energies and forces, respectively.

For characterizing the interaction between oxygen molecule and AlN surfaces, the adsorption energy is defined by the Equation 5-1,

$$E_{ads} = \frac{1}{N} \left(E_{O/AlN} - E_{AlN} - \frac{N}{2} E_{O_2} \right), \quad (6-1)$$

where N is the number of O atoms adsorbed on the AlN surface, $E_{O/AlN}$ is the total energy of the oxygen adsorbed on the surface, E_{AlN} is the energy of the fully relaxed AlN surface, and E_{O_2} is the energy of single O₂ molecule in the vacuum. According to this equation, negative values mean bound states while positive values mean the states are unstable with respect to desorption.

6.2 Adsorption of Atomic and Molecular Oxygen on the AlN surface

The preferred adsorption sites are explored for atomic oxygen on the flat AlN surface by performing geometric optimization calculations. Three equilibrium adsorption sites denoted by A, B, and C in Figure 6-1 are identified for the (2×2) (10 $\bar{1}$ 0) surface and Table 2 summarizes the adsorption energies at these sites. Site A lies above the Al-N dimer with an adsorption energy of -0.98 eV/atom, and site B lies between adjacent Al-N dimers with an adsorption energy of -0.59 eV/atom. Site C bonds two parallel Al-N dimers with adsorption energy of -0.10 eV/atom, which is much lower than the others. It should be noted that atomic oxygen placed right above the Al and N atoms are unstable and eventually move to the A site.

In the case of atomic oxygen on the stepped AlN surface, based on the result of the preferred site on the flat surface, three equilibrium adsorption sites that all lie above the Al-N dimer and are denoted by D, E, and F, as shown in Figure 6-1, are explored. The adsorption energies for these three sites are listed in Table 2. Site F exhibits the largest adsorption energy (-1.08 eV/atom) followed by site D (-1.00 eV/atom) and then site E (-0.96 eV/atom). The results indicate that the step edge may lead to enhanced adsorption behavior.

In the case of the adsorption and dissociation of the oxygen molecule, the energy change for these processes is revealed in Figure 6-2. In Figure 6-2(a), the initial state starts with a flat surface with an O₂ lying far away from the surface (>8 Å). When the O₂ is adsorbed on the surface, the total energy is decreased by 1.37 eV/atom. The final state is O₂ dissociation and both oxygen atoms are sitting on the preferred site A, in which the total energy is decreased by 1.987 eV/atom compared to the initial state. As

for the stepped surface, the start of initial state is similar to that on flat surface, where O_2 lies horizontally some distance from the surface. Because it is more complicated to anticipate the preferred sites for O_2 dissociation on a stepped surface, the oxygen molecule is placed above the Al-N dimer in the vicinity of the top step edge to optimize the calculation, as illustrated in Figure 6-2(b). Following optimization, the results indicate that the oxygen molecule spontaneously dissociates into two oxygen atoms (d_{O-O} is 1.49 Å) and the total energy is decreased by 2.096 eV/atom compared to the initial state. The spontaneous dissociation of O_2 is enhanced by the step edge where the undercoordinated surface atoms form bonds to the newly dissociated oxygen atoms. Therefore, in the next step, we would like to discuss this spontaneous dissociation with electron density plots.

6.3 Summary

In this work, first-principles, density-functional theory calculations are used to investigate the role of surface steps on the adsorption of oxygen molecules and their subsequent dissociation. The specific system considered is AlN($10\bar{1}0$) with a monoatomic step. The results indicated that adsorption in the vicinity of the top step edge leads to the spontaneous dissociation of O_2 , which does not occur on the bare terrace. This work will serve as a benchmark for the testing and validation of future Al/ Al_2O_3 /AlN COMB potentials.

Table 6-1. Comparison of the computed bulk properties to the experimental data.

AlN (wurtzite)	Experiment	This work
a (Å)	3.110	3.109 (-0.03 %)
c (Å)	4.978	4.990 (+0.24 %)
a/c	1.601	1.608 (+0.43 %)
E_c (eV/atom)	-7.497	-7.446 (-0.68 %)

Table 6-2. Predicted adsorption energies (E_{ads})(eV) of atomic oxygen on the flat and stepped AlN($10\bar{1}0$) surfaces.

<i>Adsorption site</i>	E_{ads} (flat)	E_{ads} (stepped)
top Al	unstable	
top N	unstable	
A	-0.98	
B	-0.59	
C	-0.10	
D		-1.00
E		-0.96
F		-1.08

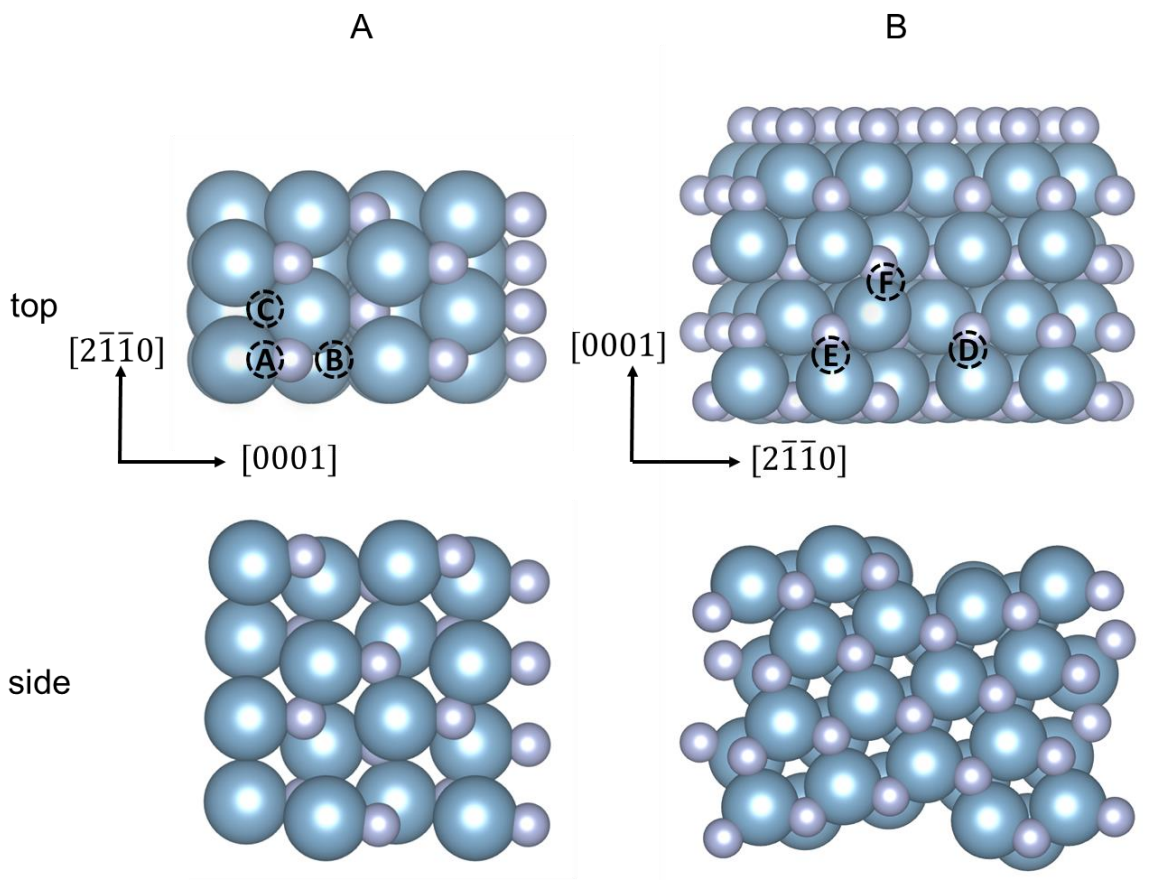


Figure 6-1. Stable adsorption sites on the flat and stepped AlN($10\bar{1}0$) surfaces. A) Flat surface structure and three stable adsorption sites (denoted by A, B, and C). B) Stepped surface and three stable adsorption sites (denoted by D, E, and F).

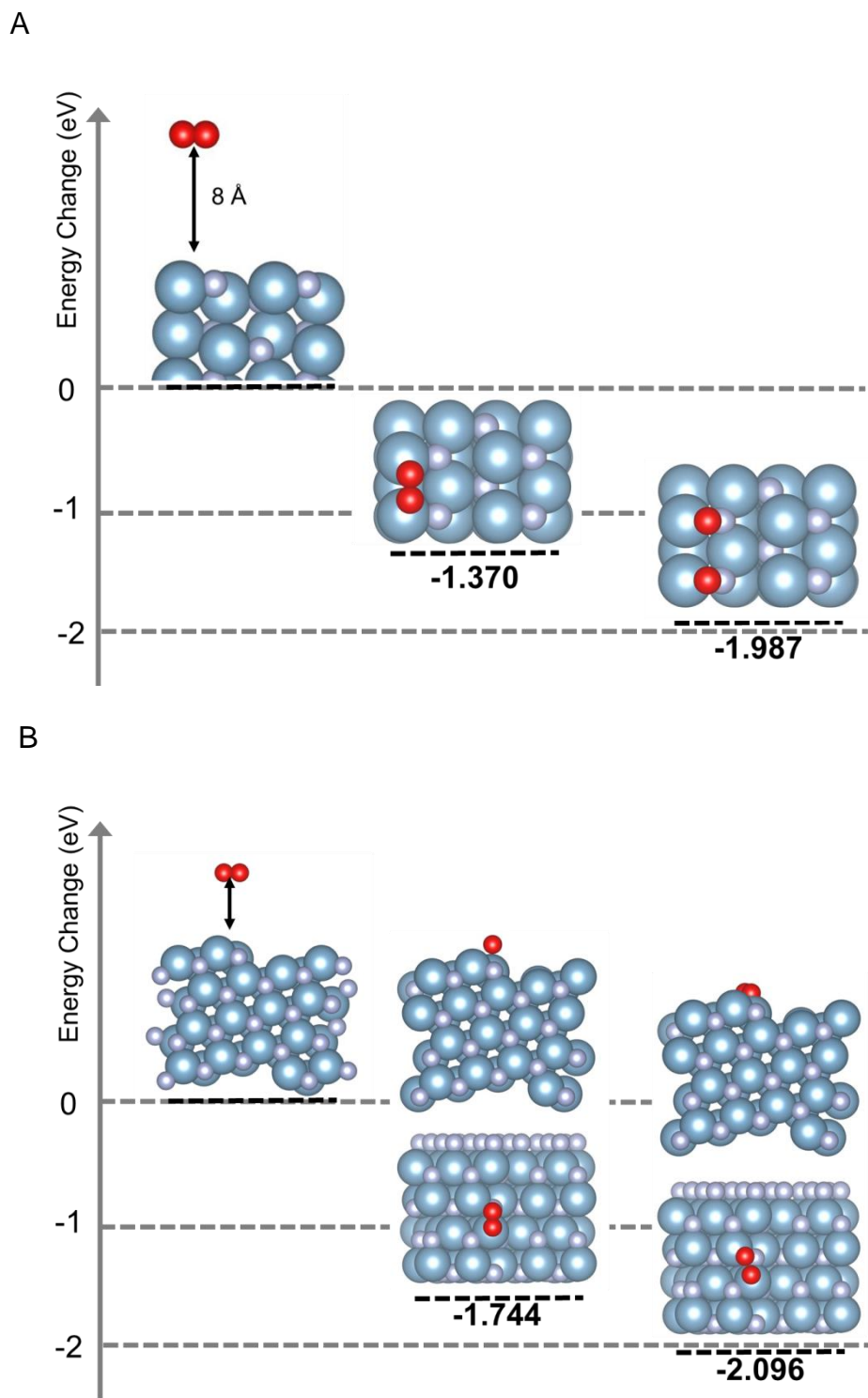


Figure 6-2. The energy change of the adsorption and dissociation of O_2 on the flat and stepped AlN(10 $\bar{1}$ 0) surface. A) flat and B) stepped.

CHAPTER 7 CONCLUSIONS

In this dissertation, we report on the development and parameterization of third-generation charge-optimized many-body (COMB) potential for the Cu/ZnO, TiN, and Ti/TiO₂ systems. Because the most important features of COMB are that it includes many-body interactions with directional bonds and dynamic charge transfer, it is able to correctly model complex physical, chemical, and mechanical processes in these systems on their own or in combination with other systems parameterized within COMB. This approach was used to examine several different problems related to processes at surfaces and interfaces.

First, the growth mode of Cu on ZnO(10 $\bar{1}$ 0) was characterized by modeling the deposition and subsequent Cu growth with COMB. Through MD simulations, the evolution of Cu growth was explored, and the results indicated that deposited Cu atoms form clusters on ZnO(10 $\bar{1}$ 0). In particular, the simulation results clearly elucidated the ways in which Cu growth transitions from layer-by-layer to three-dimensional as converge increases, a topic that is currently the subject of controversy in the literature. In addition, the influence of such factors as incident cluster deposition energy, ZnO surface temperature, and the nature of the oxide support on the potential nanoscaled changes at the interfaces, such as Cu-Zn mixing during high energy deposition and the different charge states of Cu atoms on different supporting surfaces, were examined. These results are expected to provide useful guidance for the interpretation of experimental data and the optimization of supported metal systems for the catalyst applications.

Second, the properties of Ti, TiO₂ and Cu/TiO₂ were examined. The fitted and predicted properties of the Ti *hcp* metal and the TiO₂ rutile phase reasonably reproduced the experimental and density functional values. Most importantly, without the need for re-parameterization but combining the Ti/TiO₂ potential developed in this work with a previously parameterized potential for Cu/Cu₂O, COMB predicted that a preferred adsorption site for a single Cu atom is in between two bridging O atoms followed by the site above the bridging O atom and the five-fold coordinated Ti atom on the TiO₂(110) surface, which agrees with the results of density functional theory calculations and experimental observations. Further, COMB predicted enhanced bonding between Cu clusters and the oxidized surface and indicated that a metal-oxide bond between Cu and O was responsible for the high adsorption energy in this system. These results are expected to provide useful guidance to fabricate dispersed Cu clusters on TiO₂ and thus improve their catalytic activity. Furthermore, the adsorption mechanisms identified in this work could be applicable to other transition metal/oxide systems.

Third, the COMB potentials developed for TiN systems were used to investigate the relationship between interfacial structure and adhesive properties of Ti/TiN interfaces. The results indicated that the COMB potentials correctly described the energetics of adhesion energy and charge distribution for three different interfacial structures of fcc-Ti(001)/TiN(001), which are reasonably consistent with density functional theory calculations. In addition, the characterization of the adsorption of oxygen atoms and molecules on the TiN(001) surface showed that the COMB potentials

for Ti/TiN/TiO₂ and N/NO systems were well suited to explore the chemistry associated with their oxidation.

Fourth, first-principles, density-functional theory calculations were used to investigate the role of surface steps on the adsorption of oxygen molecules and their subsequent dissociation on the AlN(10 $\bar{1}$ 0) surface with a monoatomic step. The results indicated that adsorption at the vicinity of top step edge leads to a spontaneous dissociation of O₂. This work will serve as a benchmark for the testing and validation of Al/Al₂O₃/AlN COMB potentials currently being refined by other graduate students.

While the COMB potential has a complex formalism for the potential energy, its design allows parameters to be flexible and transferable in multicomponent systems, as the examples in this dissertation illustrate. They are particularly well-suited for the study of complex processes at surfaces and provide detailed atomic mechanisms that complement experimental observations and measurements. Most recently, the author participated in a more challenging task to examine the electrocatalytic reduction of CO₂ on the Cu/ZnO catalyst, as shown in Fig. 1-4, using the COMB potential. In this work, the products observed during MD simulations resemble those experimentally measured, which further demonstrates the ability of COMB to probe the complex process of surface catalysis.

As a result of the work carried out and described in this dissertation, powerful new computational methods are thus available. These methods can be considered to be potent tools when used in combination with experimental methods to elucidate the details of complex processes in materials.

APPENDIX
POTENTIAL PARAMETERS FOR COMB POTENTIALS DEVELOPED IN THIS WORK

The atomic and electrostatic parameters of COMB potentials for pure elements (O, Cu, N, Ti, and Zn) are given in Table A-1, while the bond-typed parameters for pure elements and binary systems (Cu/ZnO, TiO₂, and TiN) are given in Tables A-2, A-3, and A-4.

Table A-1. Atomic and electrostatic parameters of pure elements (O, Cu, N, Ti, and Zn) for COMB3 potentials.

	O	Cu	N	Ti	Zn
X (eV·q ⁻¹)	6.599630	3.652316	6.209731	3.095768	3.389925
J (eV·q ⁻²)	5.955097	3.213926	9.292255	4.230280	8.162758
K (eV·q ⁻³)	0.760433	0.747810	-1.254466	-1.039759	-3.381140
L (eV·q ⁻⁴)	0.009388	0.117292	0.286350	0.357428	0.921681
ξ (Å ⁻¹)	1.371794	1.397263	1.438711	0.724352	0.673439
Z (q)	-1.539170	0.467753	-0.552136	3.022932	0.620000
u_1 (eV·q ⁻³ ·r ⁻³)	1.966411	0.309036	1.048322	0.365635	0.339814
u_1 (eV·q ⁻⁴ ·r ⁻⁵)	2.521788	0.926620	3.911805	0.764850	0.670207
D_U (Å)	-1.213951	-0.133947	-0.688784	-0.500000	-0.50040
D_L (Å)	0.007664	0.349021	0.199693	0.005000	0.529610
Q_U (q)	6	2	5	4	4
Q_L (q)	-2	-2	-3	-4	-4

Table A-2. Bond-typed parameters of pure element (O, Cu, N, Ti, and Zn) for COMB3 potentials.

	O-O	Cu-Cu	N-N	Ti-Ti	Zn-Zn
A (eV)	4956.338821	712.352722	7654.972656	516.5873248	2842.164795
B ₁ (eV)	688.163507	102.826096	2102.295654	117.0421345	494.811310
B ₂ (eV)	0.000000	0.000000	0.000000	0.000000	510.776123
B ₃ (eV)	0.000000	0.000000	0.000000	0.000000	530.021545
$\lambda(\text{\AA}^{-1})$	5.295119	2.712035	5.218037	2.136011	2.626286
$\alpha_1(\text{\AA}^{-1})$	3.258854	1.467089	3.738549	1.178831	2.352653
$\alpha_2(\text{\AA}^{-1})$	0.000000	0.000000	0.000000	0.000000	2.330411
$\alpha_3(\text{\AA}^{-1})$	0.000000	0.000000	0.000000	0.000000	2.288269
β	3.258854	1.467089	3.738549	0.545629	2.364559
n	1.000000	1.000000	1.000000	0.566048	0.626739
m	1.000000	1.000000	1.000000	1.000000	1.000000
b ₆	14.177827	0.000000	0.000000	0.550400	0.000000
b ₅	16.001644	0.000000	0.000000	-0.065549	0.000000
b ₄	1.257097	0.000000	0.812665	-0.130433	0.000000
b ₃	-5.652039	0.000000	1.724015	0.093054	0.000000
b ₂	-0.204688	0.000000	0.698596	0.226674	0.000000
b ₁	1.826597	0.000000	0.283832	0.146606	0.000000
b ₀	0.856557	0.231055	1.691325	0.077183	0.002774
c ₀	0.000000	0.000000	0.000000	-0.012318	0.002783
c ₁	0.000000	0.000000	0.000000	0.175079	0.001013
c ₂	0.000000	0.000000	0.000000	0.066085	-0.002213
c ₃	0.000000	0.000000	0.000000	-0.076109	0.001191
n _B	10.00	10.00	10.00	10.00	10.00
R _s (Å)	2.40	3.20	2.00	3.90	2.60
S _s (Å)	2.80	3.50	2.30	4.10	3.00

Table A-3. Bond-typed parameters of Cu/ZnO system for COMB potential developed in this work.

	O-Cu	Cu-O	O-Zn	Zn-O	Cu-Zn	Zn-Cu
A (eV)	1336.465698	1336.465698	1407.226318	1407.226318	1318.298950	1318.298950
B ₁ (eV)	934.717041	934.717041	155.372025	155.372025	416.695190	416.695190
B ₂ (eV)	0.000000	0.000000	147.597641	147.597641	0.000000	0.000000
B ₃ (eV)	0.000000	0.000000	177.190201	177.190201	0.000000	0.000000
$\lambda(\text{\AA}^{-1})$	2.353223	2.353223	2.843915	2.843915	2.774643	2.774643
$\alpha_1(\text{\AA}^{-1})$	2.092751	2.092751	1.971994	1.971994	1.900813	1.900813
$\alpha_2(\text{\AA}^{-1})$	0.000000	0.000000	2.035631	2.035631	0.000000	0.000000
$\alpha_3(\text{\AA}^{-1})$	0.000000	0.000000	2.060415	2.060415	0.000000	0.000000
β	2.253174	2.229919	2.060761	0.725662	1.900813	1.900813
n	1.000000	1.000000	1.000000	0.626739	1.000000	0.626739
m	1.000000	1.000000	1.000000	1.000000	1.000000	1.000000
b ₆	0.000000	0.002251	-0.041682	0.024056	0.000000	0.000000
b ₅	0.000000	0.001783	0.408499	0.002583	0.000000	0.000000
b ₄	-0.010825	0.018164	-0.097052	0.067959	0.000000	0.000000
b ₃	0.009698	0.003013	-0.285974	-0.028187	0.000000	0.000000
b ₂	-0.045080	0.002789	0.836569	0.067872	0.000000	0.000000
b ₁	0.021738	0.004218	0.926345	-0.110034	0.000000	0.000000
b ₀	0.155773	0.000704	0.636860	0.050320	0.247469	0.227573
c ₀	-0.009366	0.034866	-0.006728	-0.036859	0.000000	0.000000
c ₁	0.149421	-0.012322	0.134903	0.047156	0.000000	0.000000
c ₂	-0.009016	0.019651	0.353478	-0.000017	0.000000	0.000000
c ₃	-0.009550	-0.021196	0.123085	0.015725	0.000000	0.000000
n _B	10.00	10.00	10.00	10.00	10.00	10.00
R _s (Å)	2.30	2.30	2.60	2.60	3.30	3.30
S _s (Å)	2.60	2.60	3.00	3.00	3.60	3.60

Table A-4. Bond-typed parameters of TiN and TiO₂ systems for COMB3 potentials developed in this work.

	O-N	N-O	O-Ti	Ti-O	Ti-N	N-Ti
A (eV)	7654.972656	7654.972656	1556.205566	1556.205566	1876.810769	1876.810769
B ₁ (eV)	2102.295654	2102.295654	212.525665	212.525665	194.957894	194.957894
B ₂ (eV)	0.000000	0.000000	183.473007	183.473007	172.903008	172.903008
B ₃ (eV)	0.000000	0.000000	181.943161	181.943161	198.120622	198.120622
$\lambda(\text{\AA}^{-1})$	5.218037	5.218037	2.868830	2.868830	3.084135	3.084135
$\alpha_1(\text{\AA}^{-1})$	3.738549	3.738549	2.129506	2.129506	1.866843	1.866843
$\alpha_2(\text{\AA}^{-1})$	0.000000	0.000000	2.142030	2.142030	2.104133	2.104133
$\alpha_3(\text{\AA}^{-1})$	0.000000	0.000000	2.030774	2.030774	2.569293	2.569293
β	0.545629	3.738549	2.557314	0.791273	1.093141	3.364171
n	1.000000	1.000000	1.000000	0.566048	0.566048	1.000000
m	1.000000	1.000000	1.000000	1.000000	1.000000	1.000000
b ₆	0.550400	0.000000	0.150761	0.049978	0.000002	0.000000
b ₅	-0.065549	0.000000	0.157712	0.154609	0.000022	0.000023
b ₄	-0.130433	0.812665	-0.010905	0.044523	-0.011337	0.021388
b ₃	0.093054	1.724015	0.097477	0.169396	0.058494	0.266099
b ₂	0.226674	0.698596	0.068680	0.179627	0.186848	0.539999
b ₁	0.146606	0.283832	-0.190148	-0.239884	0.219402	-0.103172
b ₀	0.077183	1.691325	0.130799	0.184842	0.280179	0.061309
c ₀	-0.012318	0.000000	-0.020522	-0.003457	-0.030106	-0.052880
c ₁	0.175079	0.000000	-0.028074	-0.022650	-0.064553	-0.034314
c ₂	0.066085	0.000000	0.064522	0.016666	-0.001688	0.020290
c ₃	-0.076109	0.000000	-0.026573	-0.003002	-0.067116	0.020788
n _B	10.00	10.00	10.00	10.00	10.00	10.00
R _s (Å)	2.00	2.00	2.80	2.80	2.60	2.60
S _s (Å)	2.30	2.30	3.20	3.20	3.00	3.00

REFERENCE LIST

- 1 U. Diebold, J. M. Pan, and T. E. Madey, *Surf. Sci.* **331-333**, 845 (1995).
- 2 V. E. Henrich and P. A. Cox, *The surface science of metal oxides* (Cambridge University Press, Cambridge, 1996).
- 3 H. O. Pierson ed., *Handbook of refractory carbides and nitrides: properties, characteristics, processing, and applications* (Noyes Publications, Park Ridge, N.J., 1996).
- 4 C. T. Campbell, *Surf. Sci. Rep.* **27**, 1 (1997).
- 5 U. Diebold, *Surf. Sci. Rep.* **48**, 53 (2003).
- 6 N. P. Padture, m. Gell, and E. H. Jordan, *Science* **296**, 280 (2002).
- 7 R. A. Miller, *J. Am. Chem. Soc.* **67**, 517 (1984).
- 8 M. Le, M. Ren, Z. Zhang, P. T. Sprunger, R. L. Kurtz, and J. C. Flake, *J. Electrochem. Soc.* **158**, E45 (2011).
- 9 P. Lazcano, M. Batzill, U. Diebold, and P. Häberle, *Phys. Rev. B* **77**, 035435 (2008).
- 10 G. Zhou and J. C. Yang, *J. Mater. Res.* **20**, 1684 (2005).
- 11 T. Do, S. J. Splinter, C. Chen, and N. S. McIntyre, *Surf. Sci.* **387**, 192 (1997).
- 12 N. Birks, G. H. Meier, and F. S. Pettit, *Introduction to the high-temperature oxidation of metals* (Cambridge University Press, Cambridge, 2009).
- 13 H. G. Karge and J. Weitkamp eds., *Adsorption and diffusion* (Springer, Verlag Berlin Heidelberg, 2008).
- 14 X. M. Liu, G. Q. Lu, Z. F. Yan, and J. Beltramini, *Ind. Eng. Chem. Res.* **42**, 6518 (2003).
- 15 T. Shishido, M. Yamamoto, D. Li, Y. Tian, H. Morioka, M. Honda, T. Sano, and K. Takehira, *Appl. Catal., A* **303**, 62 (2006).

- 16 Y. Tanaka, T. Utaka, R. Kikuchi, K. Sasaki, and K. Eguchi, *Appl. Catal., A* **238**, 11 (2003).
- 17 T. Shishido, Y. Yamamoto, H. Morioka, K. Takaki, and K. Takehira, *Appl. Catal., A* **263**, 249 (2004).
- 18 T. C. Germann and K. Kadau, *Int. J. Mod. Phys. C* **19**, 1315 (2008).
- 19 J. E. Jones, *Proc. Phys. Soc.* **43**, 461 (1931).
- 20 J. E. Jones, *Proc. R. Soc. Lond. A* **106**, 463 (1924).
- 21 M. S. Daw and M. I. Baskes, *Phys. Rev. Lett.* **50**, 1285 (1983).
- 22 M. S. Daw and M. I. Baskes, *Phys. Rev. B* **29**, 6443 (1984).
- 23 R. A. Buckingham, *Proc. R. Soc. London, Ser. A* **168**, 264 (1938).
- 24 G. V. Lewis and C. R. A. Catlow, *J. Phys. C: Solid State Phys.* **18**, 1149 (1985).
- 25 M. W. Finnis and J. E. Sinclair, *Phil. Mag. A* **50**, 45 (1984).
- 26 F. Cleri and V. Rosato, *Phys. Rev. B* **48**, 22 (1993).
- 27 J. G. Yu, S. B. Sinnott, and S. R. Phillpot, *Phys. Rev. B* **75**, 085311 (2007).
- 28 T.-R. Shan, B. D. Devine, T. W. Kemper, S. B. Sinnott, and S. R. Phillpot, *Physical Review B* **81**, 125328 (2010).
- 29 B. Devine, T. R. Shan, Y. T. Cheng, A. J. H. McGaughey, M. Lee, S. R. Phillpot, and S. B. Sinnott, *Phys. Rev. B* **84**, 17 (2011).
- 30 T. Liang, B. Devine, S. R. Phillpot, and S. B. Sinnott, *J. Phys. Chem. A* **116**, 7976 (2012).
- 31 A. C. T. van Duin, S. Dasgupta, F. Lorant, and W. A. Goddard, *J. Phys. Chem. A* **105**, 9396 (2001).
- 32 J. Tersoff, *Phys. Rev. B* **37**, 6991 (1988).
- 33 J. Tersoff, *Phys. Rev. B* **38**, 9902 (1988).

- 34 A. K. Rappe and W. A. Goddard III, *J. Phys. Chem.* **95** (1991).
- 35 T.-R. Shan, B. D. Devine, S. R. Phillpot, and S. B. Sinnott, *Physical Review B* **83**, 115327 (2011).
- 36 D. W. Brenner, O. A. Shenderova, J. A. Harrison, S. J. Stuart, B. Ni, and S. B. Sinnott, *J. Phys.: Condens. Matter* **14**, 783 (2002).
- 37 K. H. Ernst, A. Ludviksson, R. Zhang, J. Yoshihara, and C. T. Campbell, *Phys. Rev. B* **47**, 13782 (1993).
- 38 J. M. Pomeroy, A. Couture, J. Jacobsen, C. C. Hill, J. P. Sethna, B. H. Cooper, and J. D. Brock, *MRS Proc.* **648**, P7.3 (2000).
- 39 P. Hohenberg and W. Kohn, *Phys. Rev. B* **136**, B864 (1964).
- 40 W. Kohn and L. J. Sham, *Phys. Rev.* **140**, 1133 (1965).
- 41 J. P. Perdew and A. Zunger, *Phys. Rev. B* **23**, 5048 (1981).
- 42 J. P. Perdew, J. A. Chevary, S. H. Vosko, K. A. Jackson, M. R. Pederson, D. J. Singh, and C. Fiolhais, *Phys. Rev. B* **46**, 6671 (1992).
- 43 J. P. Perdew, K. Burke, and M. Ernzerhof, *Phys. Rev. Lett.* **77**, 3865 (1996).
- 44 D. Sholl and J. A. Steckel, *Density Functional Theory: A Practical Introduction* (Wiley New Jersey, 2009).
- 45 D. Frenkel and B. Smit, *Understanding Molecular Simulation: From Algorithms to Applications* (Academic Press, 2001).
- 46 T. Liang, B. Devine, S. R. Phillpot, and S. B. Sinnott, *J. Phys. Chem. A* **116**, 7976 (2012).
- 47 H. Toufar, K. Nulens, G. O. A. Janssens, W. J. Mortier, R. A. Schoonheydt, F. D. Proft, and P. Geerlings, *J. Phys. Chem.* **100**, 15383 (1996).
- 48 F. H. Streitz and J. W. Mintmire, *Phys. Rev. B* **50**, 11996 (1994).
- 49 J. C. Slater, *Phys. Rev.* **36**, 57 (1930).

- 50 D. Wolf, P. Keblinski, S. R. Phillpot, and J. Eggebrecht, *J. Chem. Phys.* **110**, 8254 (1999).
- 51 P. P. Eward, *Ann. Phys* **369**, 253 (1921).
- 52 M. Wilson, M. Exner, Y. M. Huang, and M. W. Finnis, *Phys. Rev. B* **54**, 15683 (1996).
- 53 H. A. Stern, G. A. Kaminski, J. L. Banks, R. H. Zhou, B. J. Berne, and R. A. Friesner, *J. Phys. Chem. B* **103**, 4730 (1999).
- 54 J. Tersoff, *Phys. Rev. Lett.* **56**, 632 (1986).
- 55 A. Yasukawa, *Jsmc Int. J. Ser. A* **39**, 313 (1996).
- 56 D. W. Brenner, *Phys. Rev. B* **42**, 9458 (1990).
- 57 B. J. Thijsse, *Nucl. Instr. and Meth. in Phys. Res. B* **228** (2005).
- 58 J. A. Martinez, D. E. Yilmaz, T. Liang, S. B. Sinnott, and S. R. Phillpot, *Curr. Opin. Solid State Mater. Sci.*, <http://dx.doi.org/10.1016/j.cossms.2013.09.001> (2013).
- 59 G. Kresse and J. Hafner, *Phys. Rev. B* **47**, 558 (1993).
- 60 G. Kresse and J. Hafner, *Phys. Rev. B* **49**, 14251 (1994).
- 61 G. Kresse and J. Furthmüller, *Phys. Rev. B* **54**, 11169 (1996).
- 62 G. Kresse and J. Furthmüller, *Comp. Mater. Sci.* **6**, 15 (1996).
- 63 M. J. Frisch, et al., (Gaussian, Inc., Wallingford, CT, 2009).
- 64 W. E, W. Ren, and E. Vanden-Eijnden, *Phys. Rev. B* **66**, 052301 (2002).
- 65 H. Jonsson, G. Mills, and K. W. Jacobsen, in *Classical and Quantum Dynamics in Condensed Phase Simulations*, Ed. B. J. Berne, G. Ciccotti and D. F. Coker, 385 (World Scientific, 1998).
- 66 G. Henkelman and H. Jonsson, *J. Chem. Phys.* **111**, 7010 (1999).

- 67 H.-J. Ernst, F. Fabre, and J. Lapujoulade, Phys. Rev. B **46**, 1929 (1992).
- 68 M. Breeman and D. O. Boerma, Surf. Sci. Rep. **269-270**, 224 (1992).
- 69 L. Hansen, P. Stoltze, K. W. Jacobsen, and J. K. Nørskov, Phys. Rev. B **44**, 6523 (1991).
- 70 C. L. Liu, J. M. Cohen, J. B. Adams, and A. F. Voter, Surf. Sci. **253**, 334 (1991).
- 71 C. Lee, G. T. Barkema, M. Breeman, A. Pasquarello, and R. Car, Surf. Sci. **306**, L575 (1994).
- 72 G. A. Evangelakis and N. I. Papanicolaou, Surf. Sci. **347**, 376 (1996).
- 73 G. Henkelman and H. Jónsson, J. Chem. Phys. **111**, 7010 (1999).
- 74 S. Plimpton, J. Comp. Phys. **117**, 1 (1995).
- 75 A. O. Oluwajobi and X. Chen, Int. J. Auto. Comp. **8**, 326 (2011).
- 76 S. J. Plimpton and A. P. Thompson, MRS Bulletin **37**, 513 (2012).
- 77 G. C. Chinchin, K. C. Waugh, and D. A. Whan, Appl. Catal. **25**, 101 (1986).
- 78 J. Yoshihara and C. T. Campbell, J. Catal. **161**, 776 (1996).
- 79 T. S. Askgaard, J. K. Nørskov, C. V. Ovesen, and P. Stoltze, J. Catal. **156**, 229 (1995).
- 80 M.M. Günter, T. Ressler, B. Bems, C. Büscher, T. Genger, O. Hinrichsen, M. Muhler, and R. Schlögl, Catal. Lett. **71**, 37 (2001).
- 81 S. Sakahara, K. Yajima, R. Belosludov, S. Takami, M. Kubo, and A. Miyamoto, Appl. Surf. Sci. **189**, 253 (2002).
- 82 J. Nakamura, Y. Choi, and T. Fujitani, Top. Catal. **22**, 277 (2003).
- 83 J. B. Wagner, P. L. Hansen, A. M. Molenbroek, H. Topsøe, B.S.Clausen, and S. Helveg, J. Phys. Chem. B **107**, 7753 (2003).

- 84 J.-D. Grunwaldt, A. M. Molenbroek, N.-Y. Topsøe, T. Topsøe, and B. S. Clausen, *J. Catal.* **194**, 452 (2000).
- 85 T. Fujitani and J. Nakamura, *Appl. Catal. A* **191**, 111 (2000).
- 86 T. H. Fleisch and R. L. Mieville, *J. Catal.* **90**, 165 (1984).
- 87 J. K. W. Frese, *J. Electrochem. Soc.* **138**, 3338 (1991).
- 88 J. Flake (private communication).
- 89 O. Dulub, M. Batzill, and U. Diebold, *Top. Catal.* **36**, 65 (2005).
- 90 L. V. Koplitz, O. Dulub, and U. Diebold, *J. Phys. Chem. B* **107**, 10583 (2003).
- 91 S. V. Didziulis, K. D. Butcher, S. L. Cohen, and E. I. Solomon, *J. Am. Chem. Soc.* **111**, 7110 (1989).
- 92 J. Yoshihara, J. M. Campbell, and C. T. Campbell, *Surf. Sci.* **406**, 235 (1998).
- 93 J. Yoshihara, S. C. Parker, and C. T. Campbell, *Surf. Sci.* **439**, 153 (1999).
- 94 O. Dulub, L. A. Boatner, and U. Diebold, *Surf. Sci.* **504**, 271 (2002).
- 95 G. Kresse, O. Dulub, and U. Diebold, *Phys. Rev. B* **68**, 245409 (2003).
- 96 A. Beltrán, J. Andrés, M. Calatayud, and J. B. L. Martins, *Chem. Phys. Lett.* **338**, 224 (2001).
- 97 D. R. Hummer, J. D. Kubicki, P. R. C. Kent, J. E. Post, and P. J. Heaney, *Journal of Physical Chemistry C* **113**, 4240 (2009).
- 98 K. Klier, *Adv. Catal.* **31**, 243 (1982).
- 99 A. C. T. v. Duin, S. Dasgupta, F. Lorant, and W. A. Goddard, *J. Phys. Chem. A* **105**, 9396 (2001).
- 100 D. Raymand, A. C. T. V. Duin, D. Spångberg, W. A. G. III, and K. Hermansson, *Surf. Sci.* **604**, 741 (2010).

- 101 D. Raymand, A. C. T. v. Duin, W. A. G. III, K. Hermansson, and D. Spångberg, J. Phys. Chem. C **115**, 8573 (2011).
- 102 A. C. T. v. Duin, V. S. Bryantsev, M. S. Diallo, W. A. Goddard, O. Rahaman, D. J. Doren, D. Raymand, and K. Hermansson, J. Phys. Chem. A **114**, 9507 (2010).
- 103 T. Liang, et al., Annu. Rev. Mater. Res. **43**, 109 (2013).
- 104 Y. K. Shin, T.-R. Shan, T. Liang, M. J. Noordhoek, S. B. Sinnott, A. C. T. v. Duin, and S. R. Phillpot, MRS Bulletin **37**, 504 (2012).
- 105 V. F. Degtyareva, O. Degtyareva, M. K. Sakharov, N. I. Novokhatskaya, P. Dera, H. K. Mao, and R. J. Hemley, J. Phys.: Condens. Matter **17**, 7955 (2005).
- 106 Y.-T. Cheng, T.-R. Shan, B. Devine, D. Lee, T. Liang, B. B. Hinojosa, S. R. Phillpot, A. Asthagiri, and S. B. Sinnott, Surf. Sci. **606** (2012).
- 107 M. Hellström, D. Spångberg, K. Hermansson, and P. Broqvist, Phys. Rev. B **86**, 235302 (2012).
- 108 G. Henkelman and H. Jónsson, J. Chem. Phys. **111**, 7010 (1999).
- 109 M. P. Allen and D. J. Tildesley eds., *Computer simulation of liquids* (Oxford university press, New York, 1991).
- 110 L. Verlet, Phys. Rev. **159**, 98 (1967).
- 111 J. Yoshihara, S. C. Parker, and C. T. Campbell, Surf. Sci. **439**, 153 (1999).
- 112 G. Ehrlich and F. G. Hudda, J. Chem. Phys. **44**, 1039 (1966).
- 113 R. L. Schwoebel and E. J. Shipsev, J. Appl. Phys. **37**, 3682 (1966).
- 114 C. R. Henry, Surf. Sci. Rep. **31**, 235 (1998).
- 115 K. H. Ernst, A. Ludviksson, R. Zhang, J. Yoshihara, and C. T. Campbell, Phys. Rev. B **47**, 13782 (1993).
- 116 O. Dulub, L. A. Boatner, and U. Diebold, Surf. Sci. **504**, 271 (2002).
- 117 L. V. Koplitz, O. Dulub, and U. Diebold, J. Phys. Chem. B **107**, 10583 (2003).

- 118 U. Diebold, Surface Science Reports **48**, 53 (2003).
- 119 V. Swamy, J. D. Gale, and L. S. Dubrovinsky, Journal of Physics and Chemistry of Solids **62**, 887 (2001).
- 120 D. R. Collins, W. Smith, N. M. Harrison, and T. R. Forester, Journal of Materials Chemistry **6**, 1385 (1996).
- 121 G. V. Lewis and C. R. A. Catlow, Journal of Physics C-Solid State Physics **18**, 1149 (1985).
- 122 M. Matsui and M. Akaogi, Mol. Simul. **6**, 239 (1991).
- 123 R. T. Sanderson, Journal of the American Chemical Society **105**, 2259 (1983).
- 124 R. A. Donnelly and R. G. Parr, Journal of Chemical Physics **69**, 4431 (1978).
- 125 W. J. Mortier, K. Vangenechten, and J. Gasteiger, Journal of the American Chemical Society **107**, 829 (1985).
- 126 A. K. Rappe and W. A. Goddard, Journal of Physical Chemistry **95**, 3358 (1991).
- 127 A. Hallil, R. Tetot, F. Berthier, I. Braems, and J. Creuze, Physical Review B **73**, 165406 (2006).
- 128 R. Tetot, A. Hallil, J. Creuze, and I. Braems, Epl **83** (2008).
- 129 S.-Y. Kim, N. Kumar, P. Persson, J. Sofo, A. C. T. van Duin, and J. D. Kubicki, Langmuir **29**, 7838 (2013).
- 130 S.-Y. Kim and A. C. T. van Duin, The Journal of Physical Chemistry A **117**, 5655 (2013).
- 131 J. P. Perdew, J. A. Chevary, S. H. Vosko, K. A. Jackson, M. R. Pederson, D. J. Singh, and C. Fiolhais, Physical Review B **46**, 6671 (1992).
- 132 H. J. Monkhorst and J. D. Pack, Physical Review B **13**, 5188 (1976).
- 133 G. Kresse and D. Joubert, Physical Review B **59**, 1758 (1999).
- 134 P. E. Blochl, Physical Review B **50**, 17953 (1994).

- 135 T. Liang, S. R. Phillpot, and S. B. Sinnott, *Physical Review B* **79**, 245110 (2009).
- 136 J. X. Zheng-Johansson, O. Eriksson, and B. Johansson, *Physical Review B* **59**, 6131 (1999).
- 137 D. J. Bacon and V. Vitek, *Metall. Mater. Trans. A* **33**, 721 (2002).
- 138 J. D. Gale, *Journal of the Chemical Society-Faraday Transactions* **93**, 629 (1997).
- 139 J. D. Gale and A. L. Rohl, *Molecular Simulation* **29**, 291 (2003).
- 140 E. G. Brovman, Y. Kagan, and A. Kholas, *Soviet Physics Jetp-Ussr* **30**, 883 (1970).
- 141 M. Matsui, *Journal of Chemical Physics* **108**, 3304 (1998).
- 142 J. Scaranto, G. Mallia, S. Giorgianni, C. M. Zicovich-Wilson, B. Civalleri, and N. M. Harrison, *Surf. Sci.* **600**, 305 (2006).
- 143 F. Labat, P. Baranek, and C. Adamo, *J. Chem. Thoery Comput.* **4**, 341 (2008).
- 144 C. R. A. Catlow, C. M. Freeman, and R. L. Royle, *Physica* **131B**, 1 (1985).
- 145 A. Hallil, E. Amzallag, S. Landron, and R. Tetot, *Surface Science* **605**, 738 (2011).
- 146 M. Hu, S. Noda, and H. Komiyama, *Surf. Sci.* **513**, 530 (2002).
- 147 J. A. Rodríguez, J. Evans, J. s. Graciani, J.-B. Park, P. Liu, J. Hrbek, and J. F. Sanz, *The Journal of Physical Chemistry C* **113**, 7364 (2009).
- 148 L. Giordano, G. Pacchioni, T. Bredow, and J. F. Sanz, *Surf. Sci.* **471**, 21 (2001).
- 149 D. Phillay, Y. Wang, and G. S. Hwang, *Catal. Today* **105**, 78 (2005).
- 150 Y. Tanizawa, T. Shido, W. J. Chun, K. Asakura, M. Nomura, and Y. Iwasawa, *J. Phys. Chem. B* **107**, 12917 (2003).
- 151 D. Matthey, J. G. Wang, S. Wendt, J. Matthiesen, R. Schaub, E. Laegsgaard, B. Hammer, and F. Besenbacher, *Scienc* **315**, 1692 (2007).

- 152 J. Ø. Hansen, et al., J. Phys. Chem. C **114**, 16964 (2010).
- 153 E. Lira, J. Ø. Hansen, L. R. Merte, P. T. Sprunger, Z. Li, F. Besenbacher, and S. Wendt, Top. Catal. **2013**, 1460 (2013).
- 154 R. P. Galhenage, H. Yan, S. A. Tenney, N. Park, G. Henkelman, P. Albrecht, D. R. Mullins, and D. A. Chen, J. Phys. Chem. C **117**, 7191 (2013).
- 155 B. D. Devine, T.-R. Shan, Y.-T. Cheng, A. McGaughey, M.-Y. Lee, S. R. Phillpot, and S. B. Sinnott, Phys. Rev. B **84**, 125308 (2011).
- 156 Y.-M. Kim and B.-J. Lee, Acta Mater. **56**, 3481 (2008).
- 157 H. Yu and F. Sun, Phys. B **404**, 1692 (2009).
- 158 Z. H. Xu, L. Yuan, D. B. Shan, and B. Guo, Comput. Mater. Sci. **50**, 1432 (2011).
- 159 D. G. Isaak, J. D. Carnes, O. L. Anderson, H. Cynn, and E. Hake, Physics and Chemistry of Minerals **26**, 31 (1998).
- 160 H. Z. Yao, L. Z. Ouyang, and W. Y. Ching, Journal of the American Ceramic Society **90**, 3194 (2007).
- 161 J. Muscat, V. Swamy, and N. M. Harrison, Phys. Rev. B **65**, 224112 (2002).
- 162 P. E. Meagher and G. A. Lager, Can. Mineral **17**, 77 (1979).
- 163 W. Luo, S. F. Yang, Z. C. Wang, R. Ahuja, B. Johansson, J. Liu, and G. T. Zou, Solid State Commun. **133**, 49 (2005).
- 164 T. Mitsuhashi and O. J. Kleppa, J. Am. Ceram. Soc. **50**, 626 (1979).
- 165 L. E. Toth ed., *Transition Metal Carbides and Nitrides* (Academic Press, New York, 1971).
- 166 S. T. Oyama ed., *The Chemistry of Transition Metal Carbides and Nitrides* (Black Academic and Professional, London, UK, 1996).
- 167 P. Hedenqvist, M. Olsson, P. Wallén, Å. Kassman, S. Hogmark, and S. Jacobson, Surf. Coat. Technol. **41**, 243 (1990).
- 168 H. E. Rebenne and D. G. Bhat, Surf. Coat. Technol. **63**, 1 (1994).

- 169 K. Hai, T. Sawase, H. Matsumura, M. Atsuta, K. Baba, and R. Hatada, *J. Oral Rehabil.* **27**, 361 (2000).
- 170 M. Wittmer, *J. Vac. Sci. Technol. A* **3**, 1797 (1985).
- 171 L. Hultman, *Vac.* **57**, 1 (2000).
- 172 S. B. Sinnott and D. W. Brenner, *MRS Bulletin* **37**, 469 (2012).
- 173 M. Marlo and V. Milman, *Physical Review B* **62**, 2899 (2000).
- 174 N. C. Hernández and J. F. Sans, *Comp. Mater. Sci.* **35**, 183 (2006).
- 175 T. Iwasaki and H. Miura, *J. Mater. Res.* **16**, 1789 (2001).
- 176 Y.-T. Cheng, T.-R. Shan, T. Liang, R. K. Behera, S. R. Phillpot, and S. B. Sinnott, *J. Phys.: Condens. Matter* (submitted).
- 177 G. Kresse and J. Hafner, *Physical Review B* **47**, 558 (1993).
- 178 G. Kresse and J. Hafner, *Physical Review B* **49**, 14251 (1994).
- 179 J. P. Perdew, K. Burke, and M. Ernzerhof, *Phys. Rev. Lett.* **77**, 3865 (1996).
- 180 J. P. Perdew, K. Burke, and M. Ernzerhof, *Phys. Rev. Lett.* **78**, 1396 (1997).
- 181 H. J. Monkhorst and J. D. Pack, *Physical Review B* **13**, 5188 (1976).
- 182 C. Lee, W. Yang, and R. G. Parr, *Physical Review B* **37**, 785 (1988).
- 183 A. D. Becke, *J. Chem. Phys* **98**, 5648 (1993).
- 184 M. Fuchs, J. L. F. D. Silva, C. Stampfl, J. Neugebauer, and M. Scheffler, *Physical Review B* **65**, 245212 (2002).
- 185 D. Wolf, *Phys. Rev. Lett.* **68**, 3315 (1992).
- 186 V. Fiorentini and M. Methfessel, *J. Phys.: Condens. Matter* **8**, 6525 (1996).
- 187 S. Plimpton, *J. Comp. Phys.* **117**, 1 (1995).

- 188 K. Harafuji, T. Tsuchiya, and K. Kawamura, J. Appl. Phys. **96**, 2501 (2004).
- 189 W.-F. Wu, K.-C. Tsai, C.-G. Chao, J.-C. Chen, and K.-L. Ou, J. Electro. Mater. **34**, 1150 (2005).
- 190 L. A. S. Ries, D. S. Azambuja, and I. J. R. Baumvol, Surface and Coating Technology **89**, 114 (1997).
- 191 J. M. Lackner, L. Major, and M. Kot, Bulletin of the polish academy of science technical science **59**, 343 (2011).
- 192 J. Pelleg, L. Z. Zevin, and S. Lungo, Thin Solid Films **197**, 117 (1991).
- 193 S. V. Dudiy and B. I. Lundqvist, Physical Review B **69**, 125421 (2004).
- 194 J. Zimmermann, M. W. Finnis, and L. C. Ciacchi, J. Chem. Phys **130**, 134714 (2009).
- 195 R. G. Hennig, T. J. Lenosky, D. R. Trinkle, S. P. Rudin, and J. W. Wilkins, Physical Review B **78**, 054121 (2008).
- 196 J. O. Kim, J. D. Achenbach, P. B. Mirkarimi, M. Shinn, and S. A. Barnett, J. Appl. Phys. **72**, 1805 (1992).
- 197 S. S. Carara, L. A. Thesing, and P. Piquini, Thin Solid Films **515**, 2730 (2006).
- 198 L. Tsetseris, N. Kalfagiannis, S. Logothetidis, and S. T. Pantelides, Physical Review B **76**, 224107 (2007).
- 199 R. Bès, Y. Pilon, N. Millard-Pinard, S. Gavarini, and M. Freyss, Physical Review B **87**, 024104 (2013).
- 200 Y. Geng and M. G. Norton, J. Mater. Res. **14**, 2708 (1999).
- 201 J. W. Lee, I. Radu, and M. Alexe, J. Mater. Sci. : Materials in electronics **13**, 131 (2002).
- 202 E. W. Osborne and M. G. Norton, J. Mater. Sci. **33**, 3859 (1998).
- 203 H. Ye, G. Chen, and Y. Wu, J. Phys. Chem. C **115**, 1882 (2011).
- 204 H. Ye, G. Chen, Y. Zhu, and S.-H. Wei, Phys. Rev. B **77**, 033302 (2008).

- 205 M. S. Miao, P. G. Mosers, J. R. Weber, A. Janotti, and C. G. V. D. Walle, EPL **89**, 56004 (2010).
- 206 A. T. Gee and B. E. Hayden, J. Chem. Phys. **113**, 10333 (2000).
- 207 P. Gambardella, Z. Slijivancanin, B. Hammer, M. Blanc, K. Kuhnke, and K. Ken, Phys. Rev. Lett. **87**, 056103 (2001).
- 208 Y. Xu and M. Mavrikakis, Surf. Sci. **538**, 219 (2003).
- 209 Y. Xu and M. Mavrikakis, J. Phys. Chem. B **107**, 9298 (2003).
- 210 M. Ahonen, M. Hirsimäki, A. Puisto, S. Auvinen, M. Valden, and M. Alatalo, Chem. Phys. Lett. **456**, 211 (2008).

BIOGRAPHICAL SKETCH

Yu-Ting Cheng was born in Taoyuan, Taiwan, in 1981 to Ming-Shan Cheng and Li-Hsiang Wu. He received his bachelor's degree in mechanical engineering and master's degree in materials science and engineering from National Sun Yat-Sen University, Kaohsiung, Taiwan in 2003 and 2005, respectively. In August 2008, Yu-Ting was offered with the opportunity to pursue his Ph.D. degree at the University of Florida, and in May 2009, he was kindly provided with a research assistantship from Professor Susan B. Sinnott and since then working under her advisement towards the degree.